A compact and low-cost microwave radar prototype for breast health monitoring

Adam Santorelli

Department of Electrical and Computer Engineering

McGill University, Montréal

Québec, Canada

January, 2017

A thesis submitted to McGill University in partial fulfillment of the requirements

for the degree of Doctor of Philosophy

Abstract

Early detection of breast cancer is imperative to ensure successful treatment of the disease, motivating researchers to develop medical devices that can allow for an easily-accessible screening protocol. Currently, X-ray mammography is regarded as the "gold-standard" for screening technologies. However, it suffers from several drawbacks: i) it exposes patients to ionizing radiation, ii) the exam requires the painful compression of the breast, iii) it has difficulty imaging the breasts of young women, and iv) the high associated cost of an X-ray machine and dedicated radiologist and technician.

The development of microwave systems over the last few decades has highlighted the potential for an alternative to mammography. Microwave systems operate based on the intrinsic differences in dielectric properties between healthy and malignant tissues. These systems can exploit recent advances in wireless and telecommunication technologies to develop a low-cost, compression-free, non-ionizing medical device. Such a device can allow for the implementation of a breast cancer screening protocol worldwide and for more frequent scans starting at a younger age.

This thesis is focused on hardware and software developments and the design of a low-cost flexible prototype for early-stage breast cancer detection. The advances proposed in this thesis are focused towards the long-term research goal of developing a medical device that will allow for the monitoring of breast health with regular scans to enable the detection of abnormalities at an early stage.

First, this thesis presents an overview of the development of a clinically tested experimental system. The system is built from generic off-the-shelf components as a first prototype. A discussion of the various components and their associated cost is included. Successful images of realistic breast phantoms are generated and the system is tested with

13 healthy volunteers over several months. With this system, various signal processing methods are tested on the realistic breast phantoms to help mitigate noise (calibration and artifact removal techniques) and to detect the presence of a tumour (machine learning classification techniques).

Various tissue mimicking materials are fabricated from a mixture of polyurethane, graphite, carbon black, and acetone that can represent tissues over a wide range of dielectric properties. A variety of different hemi-spherical breast phantoms, with skin, fat, gland, and tumour structures are then fabricated from these tissue mimicking materials. The development of these stable phantoms allows for the testing of various hardware systems on the same phantoms. The quality of these phantoms are verified through imaging techniques and classification algorithms with the initial experimental system and finally with X-ray and magnetic resonance imaging (MRI).

The design and testing of a flexible multi-layer circuit board for use in a custom-built microwave system for breast health monitoring is then presented. The flexible circuit features both an integrated solid-state switching network and 16 wideband antennas. The integration of the switching matrix and the antenna array on the same substrate represents the first time that these hardware components have been integrated into a single structure. The circuit board is integrated into a previously developed clinically tested system and successful images of realistic breast phantoms are presented. The thesis is then focused on addressing the miniaturization and development of custom-built hardware components to replace the remaining off-the-shelf components within the system. Pulse generation and data acquisition are the core concepts that are addressed, as several possible solutions are explored. Lastly, the investigation of an early clinical trial conducted in a hospital, along with good clinical practice and the associated challenges, are described. This work represents a step towards a more patient-friendly, compact, cost-effective medical prototype for breast health monitoring.

Sommaire

La détection précoce du cancer du sein est impérative pour assurer un traitement efficace de la maladie, ce qui motive les chercheurs à développer des nouveau system médicaux qui peuvent permettre un protocole de dépistage facilement accessible. Présentement, mammographie par rayons X est la plus utilisée systèmes pour le dépistage du cancer du sein. Par contre, il y a plusieurs négatifs associés avec mammographie : i) il expose les patient aux radiations ionisants, ii) l'examen nécessite la compression douloureuse du sein, iii) il a des difficultés d'imagerie des seins de jeunes femmes, et iv) le coût élevé associé d'une machine à rayons X et radiologue et technicien dédié.

Le développement des systèmes qui utilise des microondes, au cours des dernières décennies, a mis en évidence le potentiel d'une alternative à la mammographie. Les systèmes hyperfréquences fonctionnent basée sur les différences intrinsèques dans les propriétés diélectriques entre les tissus sains et malins. Ces systèmes peuvent exploiter les progrès récents dans les technologies sans fil pour développer un dispositif médical non ionisant à faible coût. Un tel dispositif peut permettre d'un protocole de dépistage du cancer du sein dans le monde entier et pour des examens plus fréquents à partir d'un âge plus jeune.

Cette thèse est concentré sur les développements matériels et logiciels et la conception d'un prototype peu coûteux pour la surveillance de la santé du sein. Les progrès proposés dans cette thèse sont axés sur l'objectif à long terme de la recherche de développer un dispositif médical qui permettra de surveiller la santé du sein avec des examens réguliers pour permettre la détection des anomalies à un stade précoce.

Premièrement, cette thèse présente un aperçu du développement d'un système expérimental qui était testé cliniquement. Le système est construit des éléments génériques comme premier prototype. Une discussion sur les différents éléments et leur

coût associé est incluse. Le système était testé avec des fantômes mammaires et aussi avec 13 volontaires sains. Avec ce système, différentes méthodes de traitement du signal sont testées pour atténuer le bruit (étalonnage et techniques d'élimination des artefacts) et pour détecter la présence d'une tumeur (techniques de classification par apprentissage automatique).

Divers matériaux qui peut imiter des tissus sont fabriqués à partir d'un mélange de polyuréthane, de graphite, de noir de carbone et d'acétone. Ces matériels peuvent représenter des divers tissus sur une large gamme de propriétés diélectriques. Une variété de fantômes de sein hémi-sphériques avec des structures de peau, de graisse, de glande, et de tumeur sont ensuite fabriqués à partir de ces matériaux imitant des tissus. Le développement de ces fantômes stables permet de tester différents systèmes sur les mêmes fantômes. La qualité de ces fantômes est vérifiée par des techniques d'imagerie et des algorithmes de classification avec le système expérimental initial et enfin avec l'imagerie par résonance magnétique (IRM) et rayons X.

La conception et l'analyse d'un circuit imprimé multicouches et flexible, pour utilisation dans un système de micro-ondes, pour la surveillance de la santé du sein est ensuite présenté. Le circuit flexible comporte à la fois un réseau de commutation à semi-conducteurs intégré et 16 antennes à large bande. L'intégration de la réseau de commutation et du réseau d'antennes sur le même substrat représente la première fois que ces éléments ont été intégrés dans une structure unique. Le circuit imprimé est intégrée dans un système testé cliniquement et développé avec succès des images de fantômes de sein réalistes. La thèse est ensuite axée sur la miniaturisation et le développement de composants matériels pour remplacer les éléments restants dans le système. La génération de signaux et l'acquisition de données sont les concepts fondamentaux qui sont analysées. Enfin, l'étude d'un essai clinique précoce menée dans un hôpital, ainsi que les bonnes pratiques cliniques et les défis associés, sont décrits. Ce

travail représente une étape vers un prototype médical plus convivial, plus compact et à coût faible pour la surveillance de la santé des seins.

Acknowledgements

I would like to first express my sincerest thanks to my Ph.D. (and M.Eng.) supervisor Professor Milica Popović for her support and guidance over the last few years. As my supervisor throughout my graduate studies career she has encouraged me to excel at my work, to pursue every and all research possibilities, and afforded me every opportunity to expand my research network, helping lay a strong foundation for my future career.

I would like to express gratitude to both Professor Joshua Schwartz and Professor Mark Coates. Both of whom have served as an integral part of our research team, and have been a source of invaluable feedback on experimental design, data analysis, and the result presentation.

My Ph.D. supervisory committee, Professor Jean-Jacques Laurin and Professor Dennis Giannacopoulous, were essential in providing constructive feedback and helping to guide the development of my thesis from my initial proposal.

I would like to acknowledge Mr. Don Pavlasek, workshop supervisor in the Faculty of Engineering at McGill, for allowing us access and space to create the rubber phantoms and for always helping out with any of the small mechanical issues that arose in the fabrication of experimental systems. Additionally, I'd like to thank Mr. Jules Gauthier at Polytechnique Montréal for providing access to a dielectric measurement system on several occasions on short notice.

I would like to thank the Photonic Systems Group and the Telecommunications and Signal Processing Laboratory for the loan of several pieces of equipment during the development and testing of the initial system prototype. I would also like to acknowledge CMC Microsystems for the loan of equipment and providing access to several key software programs (HFSS, Altium Designer).

I am extremely grateful for sources of funding from; le Fonds de recherche du Quebec - Nature et Technologies (FRQNT), McGill Engineering Doctoral Award (MEDA), the McGill University Graduate Research Mobility Award (GRMA), and the McGill University Graduate Research Enhancement and Travel (GREAT) awards that have allowed me to focus solely on my research and provided me opportunities to travel around the world to present my research and foster relations with other groups focused on similar topics.

I would like to thank my lab mates Karim El-Hallouai, Pragyan Hazarika, and Lena Kranold, who represent the next generation of students working on the project. I would also like to sincerely thank Dr. Evgeny Kirshin and Yunpeng Li (Ph.D. Candidate), with whom I have worked very closely since the start of my Ph.D., our work together has seen allowed us to see great progress on our experimental system from when we first started on the project many years ago.

Lastly, my deepest thanks to my colleague (and fiancée!) Dr. Emily Porter. We have worked on this project for almost seven years now and have come a long way from a system consisting of two antennas trying to detect a screw driver in air! My endless gratitude for helping me achieve everything this thesis represents.

Preface & Contribution of Authors

The novel and key contributions of this thesis that add to the field of knowledge in the development of microwave medical devices are as follows:

- The development and testing of the first clinically ready patient interface for a microwave time-domain experimental system;
- First demonstration of using machine learning classification techniques with experimental data obtained from breast phantoms;
- Application of hybrid artifact removal to a time-domain experimental system;
- Development, fabrication, and verification of stable tissue mimicking materials to represent high permittivity biological tissues;
- Development of heterogeneous modular realistic breast phantoms consisting of skin, fat, gland, and tumour regions;
- Development of a large scale phantom with four embedded tumours for verification with X-ray, ultrasound, and MRI;
- Design, testing, and integration of a multi-layer circuit board that has a solid-state switching network and embedded antenna array;
- Antenna array optimization for next generation iteration of flexible circuit board;
- Design and testing of a low-cost equivalent-time sampling circuit;
- Design of a second generation multilayer flexible circuit board with improved flexibility, fewer control lines, and optimized antenna array;
- Testing of low-cost solutions for pulse generation and data acquisition.

This research project has allowed me the opportunity to collaborate with international partners:

- At the National University of Ireland, Galway, I have had the opportunity to work with Dr. Martin O'Halloran and Adnan Elahi (Ph.D. Candidate) on adapting their hybrid artifact removal algorithm for the experimental system developed in our lab at McGill;
- My co-supervisor Dr. Joshua Schwartz (Associate Professor, Trinity University) has provided invaluable feedback and support on the development, testing, and integration of novel hardware components;
- I worked with Dr. Jochen Moll at the Goethe University of Frankfurt on the testing of rubber phantoms in various imaging modalities (MRI, CT, X-ray).

Aspects of my research presented in this thesis were done in collaboration with other students within McGill University:

- Dr. Emily Porter was responsible for interacting with patients for all clinical trials and pilot studies and was involved with the development of the initial oil-water-gelatin breast phantoms.
- Dr. Evgeny Kirshin was responsible for the design of the first electromechanical switching matrix used in the first experimental system and the initial code for the delay-multiply-and-sum algorithm used for image generation.
- Mr. Yunpeng Li (Ph.D. Candidate) helped develop the ensemble classifier used with the rubber based phantoms and helped record the data with the original system with these phantoms.

Additionally, I worked with several younger students within the lab and helped mentor them on their respective projects that fell within the framework of this research project:

- Mr. Pragyan Hazarika (M. Eng.) worked closely with me to run the iterative simulations in HFSS to optimize the antenna array for the second generation of the flexible circuit board;
- Mr. Karim El-Hallaoui (M.Eng. Student) helped with the testing of the miniaturization of pulse generation components;
- I have worked with and supervised several undergraduate students: Olivier LaForest worked closely with me in the development in the stable carbon-based phantoms; José Mastrangelo helped with the testing of the equivalent-time sampling circuit; and Kevin Cadieux helped develop some code for the interface between the microcontroller and the analog-digital converter (ADC).

Contents

List of Figures

List of Tables

List of Acronyms

2-D	2-dimensional
3-D	3-dimensional
ADC	analog-to-digital converter
CMOS	complementary metal-oxide-semiconductor
CPW	coplanar waveguide
DMAS	delay-multiply-and-sum
EM	electromagnetic
FD	frequency-domain
FPGA	field-programmable gate array
HFSS	high frequency structural simulator
LCP	liquid crystalline polymer
LDA	linear discriminant analysis
MRI	magnetic resonance imaging
MSE	mean-square error
PCA	principal component analysis
PCB	printed circuit board
PET	positron emission tomography
QDA	quadratic discriminant analysis
RMS	root mean square
SBR	Synthesized Broadband Reflector
SCR	signal-to-clutter ratio
SMA	SubMiniature version A
SSIM	structural similarity index
SVM	support vector machine
TD	time-domain
TSAR	tissue sensing adaptive radar
TWTLTLA	Travelling Wave Tapered and Loaded Transmission Line Antenna
UWB	ultrawideband
VNA	vector network analyzer

Chapter 1: Introduction

Breast cancer is the most commonly diagnosed cancer in women in both developed and developing countries, with the rate of incidence increasing rapidly in developing countries [1]. In Canada, the probability for a woman to develop breast cancer in her lifetime has surpassed 11% [2]. The early detection of breast cancer is vital to ensure a successful treatment of the disease [1] – [3]. The 5-year survival rate for women diagnosed with breast cancer is over 89% in North America [2], [3]. If the cancer is localized within the breast at the time of diagnosis the 5-year survival rate is close to 99%; once the cancer has spread to distant regions of the body (late-stage diagnosis) the 5-year survival rate decreases to just 24% [3].

However, it is important to highlight that currently only mammography has been clinically proven to be a screening methodology that reduces mortality rates [1], [4] – [6]. Unfortunately, implementing a screening protocol for an entire population represents an extreme burden on health care facilities, and is often impossible to implement due to equipment and personnel costs. As a consequence, breast cancer is more commonly diagnosed at later stages and carries a higher mortality rate in developing countries [1], [4] – [6]. In fact, the 5-year survival rate for breast cancer averages 57% in developing regions of the world [4], leading these low-income and middle-income countries (LMCs) to search for alternative low-cost technologies that will allow for population-wide screening to be implemented.

1.1 Motivation and Objectives

Currently, X-ray mammography is the primary screening protocol implemented worldwide, and is the only screening protocol to have been clinically demonstrated to

reduce mortality rates in the screened population versus an unscreened group [1] – [3]. Abnormalities detected with X-ray can be further investigated with magnetic resonance imaging (MRI) before a localized biopsy is performed to confirm the diagnosis. However, mammography as a screening technique has several drawbacks including: the use of ionizing radiation which limits the frequency and number of scans that can be performed, the painful compression of the breast, the associated cost of an X-ray machine and technician, and, most recently, increasing concerns with overdiagnosis and overtreatment [7], [8].

Microwave medical devices offer the potential for low-cost systems to be used in breast health monitoring for implementation in a screening protocol. These systems use low-power microwaves; there is no ionizing radiation and scans can be repeated as frequently as needed [8]. Microwave systems operate based on the inherent difference in dielectric properties between malignant and healthy tissues. The large amount of water associated with tumour regions creates a contrast in the complex permittivity over the microwave frequency range between the healthy and malignant tissues [9]. Additionally, with the recent advancements in wireless technology, microwave systems can be built at a fraction of the cost of a conventional X-ray machine, with little to no associated operational costs.

In this work, a low-cost, portable, and conformal microwave system for breast health monitoring is developed. This system is conceived to work by obtaining frequent scans of a patient's breast over time and using a comparative analysis to identify the development of any abnormalities. The implementation of a monitoring application, as opposed to the more infrequent scan of a conventional imaging device, reduces both the computational and technological demands of such a system.

Specifically, this thesis is focused on the design, testing, and integration of specialized low-cost hardware components to replace the bulky, large-scale, off-the-shelf components

that are commonly found in microwave system prototypes. The goal is to demonstrate that these hardware components can be used to fabricate a low-cost microwave medical device; demonstrating the potential for microwave systems as an ideal candidate to be used for breast screening protocols that can be implemented globally.

1.2 Thesis Contributions

The contributions of this thesis can be divided into three main topics within the development of microwave medical devices: i) demonstration of signal processing methods for an experimental time-domain prototype; ii) fabrication of stable and dielectrically accurate tissue mimicking materials that can accurately model high water content tissues; and iii) the design, testing, and integration of a novel low-cost and portable microwave system for breast health monitoring. A summary of the novel contributions of this thesis is as follows:

- The development and testing of the first clinically ready patient interface for a microwave time-domain experimental system;
- First demonstration of using machine learning classification techniques with experimental data obtained from breast phantoms;
- Application of hybrid artifact removal to a time-domain experimental system;
- Development, fabrication, and verification of stable tissue mimicking materials to represent high permittivity biological tissues;
- Development of heterogeneous modular realistic breast phantoms consisting of skin, fat, gland, and tumour regions;
- Development of a large scale phantom with four embedded tumours for verification with standard imaging modalities, such as CT and MRI, and ultimately for comparison with microwave images;

- Design, testing, and integration of a multi-layer circuit board that has a solid-state switching network and embedded antenna array;
- Antenna array optimization for next generation iteration of flexible circuit board;
- Integration and testing of a low-cost pulse generation and equivalent-time sampling circuit;
- Design of a second generation multilayer flexible circuit board with improved flexibility, fewer control lines, and optimized antenna array.

1.3 Thesis Outline

Chapter 2 of this thesis is focused on providing a thorough background on the topic; including a discussion on breast anatomy, the development of breast cancer, and a review of the primary breast screening technologies. An overview of microwave systems for medical diagnostics is also presented in this chapter.

In Chapter 3, a time-domain microwave radar prototype for breast health monitoring is presented. An overview and discussion on the hardware components of the system is included. Additionally, initial validation results of the system, tested with breast phantoms and patient volunteers, is also presented. Finally, the chapter concludes with an investigation into different signal processing methods to analyse data recorded with the system.

Chapter 4 discusses the development of novel stable tissue mimicking materials, which are made of a mixture of polyurethane and carbon-based particles, to represent high water content materials. A wide range of materials are fabricated and dielectric measurements are performed to verify the stability and range in their complex permittivity. From these materials, accurate breast phantoms, consisting of skin, fat, gland, and embedded tumours are fabricated. These phantoms are then tested with the initial system prototype. Finally,

a specialized phantom with four embedded low-contrast tumours is fabricated and tested with various imaging modalities (X-ray, CT, and MRI).

In Chapter 5, a novel multi-layer flexible circuit board is presented. This circuit board replaces several of the expensive and bulky components found in the initial experimental system, namely, the electromechanical switching matrix, the antenna array, and the antenna radome, with a smaller and more cost-effective solution. This circuit board is then integrated into the experimental system and its performance is compared to the initial system prototype using the rubber phantoms presented in Chapter 4. A discussion of the challenges and issues observed with this first-generation prototype are presented prior to the presentation of an improved 2nd-generation design. Finally, this chapter concludes with examples of possible hardware solutions to replace the remaining large-scale components that exist in the system, namely the pulse generator, system clock, and the high speed oscilloscope.

Chapter 6 presents some of the experiences, difficulties, and key observations from undertaking a Phase 0 clinical trial with an experimental medical device. This clinical trial was conducted at the Cedar Breast Clinic located within the McGill University Health Centre. This chapter is focused on discussing topics related to obtaining ethical approval, understanding the clinical experience and good clinical practice, and balancing competing needs.

Finally, Chapter 7 provides a concise summary of the thesis, the key results reported, and some of the potential avenues of investigation for future research for the project.

Chapter 2: Background and Literature Review

This chapter is focused on providing the reader with background information on the basics of breast cancer development, current screening methodologies for breast cancer detection, and a comprehensive review of experimental microwave systems for breast cancer detection.

2.1 Breast Anatomy Review

The human breast is composed primarily of adipose tissue that surrounds a network of glandular tissues. The glandular tissues of the breast are divided into lobules and connective ducts. The lobules are the glands responsible for the creation and storage, specifically in the alveoli of the lobules, of breast milk during a woman's nursing stage after childbirth. Lobules are arranged into groups called lobes, with each breast containing approximately 15 – 25 lobes. The connective ducts are the glandular structures which link the nipple to the lobules and allow breast milk to be delivered from the nipple. This gives the glandular tissues the appearance of a network of tissue which expands outwards from the nipple [10], [11]. The volume, size, and distribution of glandular structures within the breast can vary significantly between individuals. Adipose tissue fills the space between the skin and the glandular structures and serves as a protective layer for these glands. Breast tissue also includes the chest wall region; it includes the muscle and rib bones and extends up to the collarbone and stretches from the armpit to the centre of the chest. A diagram of the female breast anatomy is shown in Fig. 2.1.

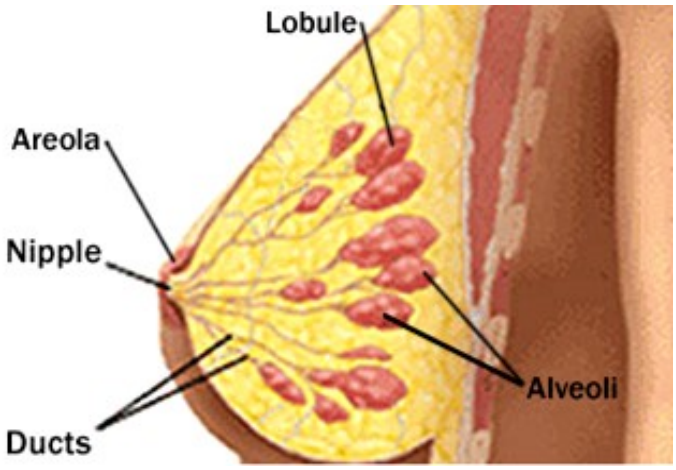

Figure 2.1. Diagram of female breast anatomy [10].

Embedded within the fatty tissue is a series of lymphatic vessels that are used to drain the breast tissues of lymph (fluid carrying white blood cells). The lymphatic vessels are connected to a series of lymph nodes through a series of lymph ducts. Lymph nodes are located throughout the human body and are interconnected via the lymphatic system. The lymphatic system is responsible for transporting and draining lymph from the various regions within the body. If malignant cancer cells within the breast reach the lymph nodes of the breast, the lymphatic system provides the opportunity for the rapid spreading of cancer throughout the body [10], [11]. A schematic of the lymphatic system near the female breast is shown in Fig. 2.2.

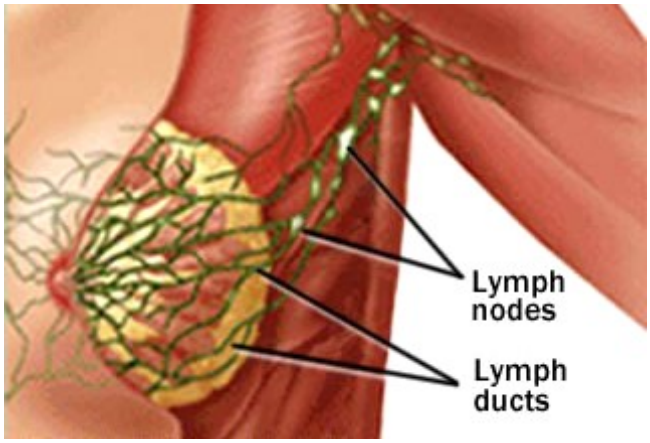

Figure 2.2. Schematic of the lymphatic system for the female breast [10].

2.1.1 Pathology of Breast Cancer

A neoplasm is defined as the new growth or formation of abnormal cells in a region. These cells seem to grow quickly, without cessation, and their growth can be invasive to the surrounding regions. Most neoplasms begin from a single cell in which the DNA has been altered from its parent cell [12]. Cancerous cells are those defined to be a part of a malignant neoplasm. The word 'tumour', while not medically accurate, is often used to describe this abnormal mass of cancerous cells. The true definition of the word tumour refers to swelling from any process. For the remainder of this thesis, the word tumour is synonymous with the growth of cancerous tissues (malignant neoplasm).

A neoplasm can be benign or malignant in nature [12]. This classification is done based on a histological examination of the affected region; thus, for the confirmation of breast cancer, a biopsy is required. Malignant neoplasms are faster growing and more aggressive than benign neoplasms (eg. cysts, benign tumours). Additionally, malignant neoplasms can invade and destroy surrounding tissue and can develop secondary points of tissue growth (metastasis) that are unconnected to the primary tumour. The potential for metastasis is what makes undiagnosed cancers extremely dangerous; they can spread

throughout the body until the cancer cells infiltrate vital organs, ultimately leading to death. A summary of the primary differences between benign and malignant neoplasms is outlined in Table 2.1.

TABLE 2.1. DIFFERENCES BETWEEN BENIGN AND MALIGNANT TUMOURS [12]

	Benign	Malign
Behaviour	No metastatic potential Slow growth	Metastatic potential Rapid growth Can infiltrate surrounding tissue
Appearance	Encapsulated, spherical, well defined region Nucleus of regular shape and size	Irregular shape Enlarged, bizarre, and variable shape and size of nucleus

Breast cancer is the development of a malignant neoplasm within the breast tissues, these cells will often group together and form a tumour. If undiagnosed, these cells can then spread through the body once they reach the lymph nodes within the breast. This danger highlights the need for early detection and treatment of the disease. While there has been no direct link found in the development of breast cancer, several risk factors have been identified: excessive weight, physical inactivity, alcohol consumption, heavy drinking, having type-II diabetes, inherited familial risk, and characteristics of the woman's reproductive life [2], [3].

Breast cancer commonly develops (over 50% of all diagnosis) in the upper outer quadrant of the breast, near the armpit [13] – [15]. Breast cancer can be divided into non-invasive, or *in situ* (in place), carcinomas and invasive carcinomas, with nearly all cancer starting within the glands or the ducts of the breast [2], [3]. The term *in-situ* describes the group of cancer cells as being well confined to the original site of growth; the cancer has not yet started to invade any of the surrounding tissue.

There are three primary non-invasive cancers; *ductal carcinoma in situ* (DCIS), *lobular carcinoma in situ* (LCIS), and Paget's disease. DCIS is the most common of all breast cancer diagnosis. In DCIS, the development of the cancerous tissues starts and remains localized within the inside lining of the breast ducts. LCIS is similar to DCIS, however, here the cancer is present in the lobules. In Paget's disease the malignancy develops near the nipple. Interestingly, DCIS and LCIS, by definition, are not malignant as the cells have not infiltrated any surrounding tissue, however, as these cells have the potential to form invasive carcinomas they are commonly referred to as malignant tumours and are removed if diagnosed [2], [3], [11].

Invasive breast cancers are primarily made up of *invasive ductal carcinoma* (IDC) and *invasive lobular carcinoma* (ILC), with IDC forming the vast majority, making up 75% of invasive breast cancer diagnoses. IDC and ILC can be viewed as advanced forms of DCIS and LCIS in which the cancerous cells have now infiltrated the surrounding tissues and are no longer limited by the ductal or lobular walls. Other invasive breast cancers include inflammatory carcinoma in which the cancer cells block the pathways of the lymphatic network; however, these conditions are quite rare [2], [3].

An important aspect for the prognosis and treatment of breast cancer is the assessment of the spread of the cancerous tissues. Staging is used to evaluate the extent to which the tumour has spread. For breast cancer a TNM staging system is used. This system is based on the size and spread of the primary tumour (T), whether the cancerous cells have spread to any lymph nodes (N), and whether any distant metastases have formed (M) [2], [12]. Tumours can be classified from Stage 0 through Stage IV.

Treatment for breast cancer is highly dependent on the diagnosis of the stage and type of cancer. These treatment protocols often involve surgical interventions. The primary surgical options are lumpectomy (localized removal of cancerous tissues within the breast) or mastectomy (removal of all breast tissues). Surgery is often performed in

combination with radiation therapy, chemotherapy, or hormone therapy. The success of these treatments relies heavily on early detection. The 5-year survival rate for patients diagnosed with Stage I or earlier breast cancer is 99% in North America [1] – [3], however, if the cancer is only detected after it has metastasized to distant tissues, the survival rate drops significantly to only 24% [1] – [3]. Currently, approximately 61% of all breast cancers (in the North America) are diagnosed at Stage I or earlier [3]. This statistic suggests that there is significant room for improving early-stage tumour diagnosis and highlights the desire for an improved screening methodology.

2.2 Review of Current Breast Screening Protocols

The motivation for implementing a public wide screening protocol for any disease is based on the fact that finding the disease prior to the development of symptoms will allow for detection at a less advanced stage, allowing for an improved treatment outlook [16]. The principles of effective screening as outlined by the World Health Organization (WHO) can be summarized by five key points [16]:

1. The disease being screened is serious and prevalent;
2. The test is sensitive and specific;
3. The test is well tolerated;
4. The test is inexpensive; and
5. The test changes therapy or outcome.

Clearly, a breast cancer screening protocol should aim to meet these key points. Currently, the only screening procedure implemented in North America is based on the use of X-ray mammography for women between the ages of 40 and 69 [2], [3]. However, the use of X-ray mammography does not seem to meet all these key points. An X-ray mammogram is painful, exposes patients to ionizing radiation, and requires access to an

X-ray mammogram and radiologists. The fact that all five of these key points are not currently met highlights the desire for the development of novel technologies that can allow for a screening protocol to be implemented world wide that can meet all these key points.

The two most commonly cited measures of the performance of a screening tool are its sensitivity and specificity [16]. In the case of breast cancer, sensitivity is defined as the percentage of correctly detected cancers out of the total number of breast cancers in the test population, it can also be referred to as the true positive rate. It is a measure of a tests ability to correctly identify patients who have the disease. The sensitivity, S_e, can be defined as in equation (2.1):

$$S_e = \frac{TP}{TP+FN} * 100\% \quad (2.1),$$

where TP is the number of true positive results (the test has correctly identified the presence of breast cancer) and FN is the number of false negative tests (the test has incorrectly reported the patient as healthy in the presence of cancer).

Specificity is the measure of a tests ability to correctly rule out the presence of the disease. It is the percentage of tests that correctly identify that a patient is healthy out of the entire healthy population that is screened, it can also be referred to as the true negative rate. The specificity, S_p, can be defined as in equation (2.2):

$$S_p = \frac{TN}{TN+FP} * 100\% \quad (2.2),$$

where TN is the number of true negatives (the test correctly identified that no disease was present) and FP is the number of false positives (the test reported cancer when the patient was healthy).

While sensitivity and specificity are the most commonly cited and easily understood metrics, they do not consider the prevalence of the disease and can thus be misleading. The positive predictive value, PPV, and the negative predictive value, NPV, are measures

that take into account the specificity, sensitivity, and the prevalence of the disease in the screened population. The positive predictive value measures the probability that a patient with a positive test has the disease. The positive predictive value is defined as:

$$PPV = \frac{TP}{TP+FP} * 100\% \quad (2.3).$$

From equation (2.3) it is clear that for a screening protocol to have a high positive predictive value the total number of false positives must be limited. The negative predictive value (NPV) measures the probability that a patient who receives a negative test result is cancer-free. The negative predictive value is defined as:

$$NPV = \frac{TN}{TN+FN} * 100\% \quad (2.4).$$

A screening tool with high specificity has a lower rate of false positives and thus higher PPV; a high sensitivity has a lower rate of false negatives and thus higher NPV. There is no one metric that is 'better' than the other for a screening system; for diseases with very low prevalence a high NPV is very useful for ruling out the disease. For diseases with higher prevalence, such as breast cancer, creating a screening system with a high PPV can limit the number of false positives, helping to reduce the burden on the health care system. The ultimate measure of effective screening lies in the reduction of the number of mortalities related to cancer [16].

2.2.1 X-ray Mammography

X-ray mammography is defined as the practice of using X-rays to image breast tissue in order to detect or diagnose breast cancer. X-ray mammography is used as both a screening and diagnostic tool. As a screening technique, X-ray mammography is conducted on an asymptomatic population of women that are assumed to be healthy [16] (of course it is possible that women without symptoms may in fact have breast cancer, these cancers are then caught in the early stage). An X-ray mammogram creates an image of

radiographic breast density; differences between healthy and malignant tissues are distinguished based on these different densities [17]. During a mammogram, the breast is compressed between two parallel metal plates resulting in a more even thickness of tissue through the scan area and improved image quality due to lower attenuation of X-rays (due to the shorter travel paths). X-ray images are then interpreted by a radiologist specializing in breast cancer; any abnormalities detected within the image are further verified by ultrasound, MRI, or biopsy.

The meta-analysis carried out in [16] has shown that the sensitivity of mammography is estimated to be within 83 to 95% and the specificity within 90 to 98%. With a false-positive rate of approximately 1 in 10 for mammography, it can be estimated that half of the women who receive an annual mammogram for 10 years will have a least one case of a false-positive test that leads to additional testing (ultrasound, MRI, or biopsy) [16].

One of the primary drawbacks of using mammography as a screening tool is that its performance is highly dependent on the density of the breast; both false-positive and false-negative results are more likely with dense breasts [16]. In a study with more than 11 000 women with no symptoms of breast cancer and with varying levels of breast density, it was shown that the sensitivity of mammography for women with extremely dense breasts was 48%; compared to the 78% percent sensitivity for entire population of women in the study [18]. This is an inherent disadvantage of using X-ray technology: MRI and ultrasound are less affected by breast density.

Despite these issues, mammography is the only clinically proven screen method to save lives from breast cancer [1] – [6], [16], and offers the best combination of sensitivity and specificity of all the currently implemented screening tools for breast cancer [16].

2.2.2 Magnetic Resonance Imaging

Magnetic resonance imaging is regularly used when abnormalities are found in a mammogram. The greater detail in MRI images allows for it to be used primarily for diagnostic and staging of breast cancer purposes [2], [3]. A MRI scan consists of exposing a patient to a strong uniform magnetic field. The presence of this strong magnetic field causes the atoms within the human body to become aligned with the direction of the field. By then applying radio waves to specific tissues it is possible to create local misalignments. MRI operates by alternating this source of radio waves; as the source is turned on and off the atoms will alternate from being in an aligned state to misaligned and emit radio waves themselves. The different tissues within the body can then be identified based on the rate at which the misaligned atoms return to the aligned state.

While MRI scans produce high resolution images, have high sensitivity, and can detect very small tumours and diagnose early stage breast cancer development [19], the scans are too time-consuming and prohibitively expensive for MRI to be useful as a screening tool. Additionally, reports of high variability in the specificity of the technique, from 37 – 97 % [19] – [21], would result in a very low positive predictive value if MRI were used as a screening tool.

2.2.3 Ultrasound

Ultrasound is based on sending sound waves into the body, and due to the different acoustic impedances from various tissues, the recorded sound waves can be used to generate an image of the tissues within the human body. Ultrasound scans are conducted by using a hand-held transducer that is pressed against the skin. The operating technician can then vary the angle of incidence and reposition the transducer to obtain images at

the desired locations. Ultrasound devices are cost-effective and portable alternatives to mammography, with images being obtained and interpreted by the technician in real time.

Currently, ultrasound is used to assess specific abnormalities that have been identified from mammography as it is adept at differentiating from benign cysts and malignant tissues [22]. However, due to poor sensitivity, just under 40% as reported in [22], and the high dependence on the operator's level of experience with interpreting ultrasound breast images [8], it does not offer a reliable alternative for a breast screening tool.

2.3 Microwave Breast Cancer Detection

The current breast cancer screening methods have significant drawbacks, as discussed in Section 2.2, that limit their effectiveness as part of a screening protocol to help save lives from breast cancer. Microwave systems offer the potential for a complementary tool to the current screening technologies. They can exploit the popularity of recent microelectronics developed and tested in wireless technologies to fabricate low-cost and compact custom built systems [8].

This thesis is focused on the development of a low-cost microwave system ideal for implementation in a breast screening protocol. The implementation of a microwave based system for breast cancer detection is possible due to the inherent contrast in the dielectric properties (relative permittivity and conductivity) between healthy and malignant tissues over the microwave frequency range [9], [23], [24]. Microwave systems illuminate the breast with electromagnetic (EM) energy in the microwave frequency range. The different tissues within the breast create various interfaces that the wave must travel through. The resulting scattered and transmitted waves are proportional to the dielectric properties on both sides of the interface. These resulting scattered and transmitted waves are dependent on the types of tissues within the breast, and thus it is possible to differentiate the presence of a cancerous tumours.

The breast is a unique organ in that it extends outward from the body; it is not behind the chest wall or other bone structures which would cause significant attenuation and scattering of the incident microwave signals. Additionally, the relatively low-loss nature of the breast, due primarily to the large percentage of adipose tissue, allows the use of low-power signals that will undergo minimal signal attenuation.

A breast scan with a microwave system is non-invasive, there is no painful compression of the breast, there is no use of ionizing radiation, and it can be considered to be free from safety concerns [8]. These benefits allow for breast scans to be repeated at frequent intervals, hopefully allowing the development of breast cancer to be detected at the earliest stage possible. Furthermore, as system components have a small footprint, can be easily mass-produced, and are a cost effective solution, microwave systems offer the potential to be distributed and used in developing countries as part of a screening protocol. While microwave imaging does not offer the same resolution as X-ray mammography or MRI, it offers sufficient detail to be a viable technique in the diagnosis of the development of tissue abnormalities [8].

2.3.1 Breast Tissue Properties

The two electrical properties of primary interest in the design and development of microwave medical tools are relative permittivity, ε_r, and conductivity, σ (S/m). These two properties govern the behaviour of an incident wave within the breast (how much energy is reflected at each interface and how much energy is lost per distance travelled). Studies on the dielectric properties of various breast tissues have suggested that there is a contrast between the healthy and malignant tissues in both relative permittivity and conductivity, particularly over the microwave frequency range. This contrast is largely attributed to the effects of water. High water content tissues (tumour, gland, and skin) have much higher permittivity and conductivity than the low water content adipose

tissues. An accurate knowledge of these properties can help in the development of microwave systems by informing specific design choices, such as frequency of operation. The difficulties with these studies on dielectric properties, and comparing the reported data, lie in the fact that the measurement techniques, whether the measurements were performed *in-vivo* or *ex-vivo*, and the temperature of the samples all play key roles in the reported measured values [26]. This section will review the research works that have contributed the most significantly in the development of microwave systems for breast cancer detection.

One of the early studies that focused on the measured dielectric properties, over the 10 Hz – 20 GHz frequency range, of human tissues was performed in 1996 by Gabriel et al. [27], [28]. The tissues were excised from human corpses during autopsies, with an exception with the skin being measured *in-vivo*. The measurements were performed at body temperature, with three different measurement techniques used to cover the wide range of frequencies examined, and the authors were able to compare their measurements with those found in the literature with a high level of similarity. The study did not involve tissues specific to the breast, however, the data in regards to skin and adipose tissues are of use in microwave applications.

In [9] and [23], a large scale study on the dielectric properties of breast tissues, based on measurements from excised tissues, was conducted. The results of this study encompassed both healthy and malignant tissues and aimed to characterize the dielectric properties of these tissues over the 500 MHz – 20 GHz frequency range. The study was split between healthy patients [23] and patients with a confirmed malignancy [9]. All measurements were performed *ex-vivo* within five hours from when the tissues were excised. The dielectric properties were measured using the standard open-ended coaxial technique; a high precision coaxial probe was connected to a vector network analyser (VNA) and the complex permittivity of the sample was recorded. The tissue type of each

sample was determined by a pathologist using a histological assessment. Some of the known confounders with this study include the time from excision to measurement (there was no standard protocol in place), the temperature of the samples, and the repeatability and reliability of human-interpretation of the histological determination.

In [23], a total of 488 samples from 93 patients were obtained, with the tissues being excised during breast reduction surgeries. Each of these samples were measured and the recorded dielectric properties were reported [23]. The samples were categorized into three specific groups based on the histological analysis: Group 1 contained samples with 0 – 30 %, Group 2 with 31 – 84 %, and Group 3 with 85 – 100 % adipose tissue, respectively. Groups 1 and 2, with low percentage of adipose tissue, correspond closely to the glandular tissues found within the breast [23]. The measured data was then fitted to a Cole-Cole model to match the measured data to a parameter-based equation that is used to model the behaviour of dispersive materials over a wide frequency range.

A reproduction of the data presented in [23] is shown in Fig. 2.3 and Fig. 2.4. Fig 2.3 is a plot of the median relative permittivity of the three groups mentioned above, with error bars denoting the 25^{th} and 75^{th} percentile for each group. From Fig 2.3 as the percentage of adipose tissue decreases the permittivity increase significantly. This result is in agreement with the idea that the high-water content breast tissues, in this case the glandular tissues, will have much higher permittivity. Similarly, Fig. 2.4 is a plot of the electrical conductivity. A similar relationship between the adipose tissue content and the electrical conductivity can be observed. From these figures, we can observe significant variation in the measured tissue properties for Group 1 and Group 2. In fact, there is a significant overlap of the two groups of data in both the permittivity and conductivity. Additionally, the study reported high level of variation of the measured data in both the patient-to-patient and sample-to-sample data. A negative correlation between the relative permittivity and the conductivity and the time from excision was also reported, however,

the time from excision and the tissue temperature were found to not be of statistical importance [23].

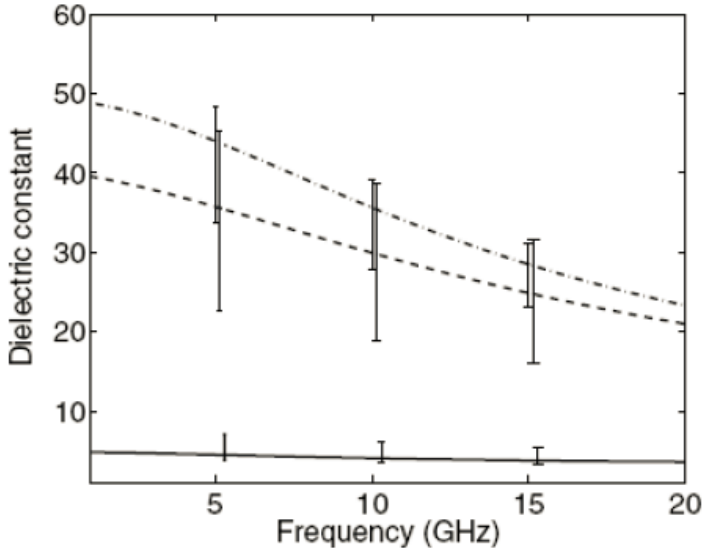

Figure 2.3. Plot of the median relative permittivity for three separate adipose content groups, reproduced from [23]. Group 1, 0 – 30 % adipose tissue, represented by the dot-dash line, Group 2, 31 – 84 % adipose tissue, represented by the dashed line, Group 3, 85 – 100 % adipose tissue, represented by the solid line.

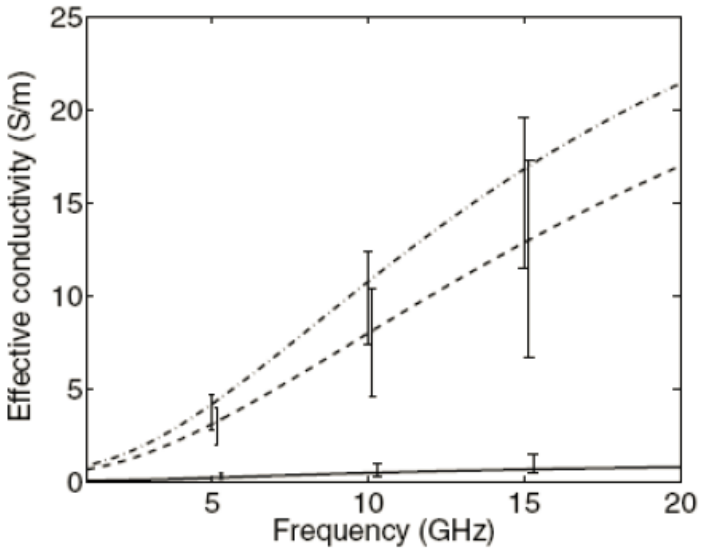

Figure 2.4. Plot of the median conductivity for three separate adipose content groups, reproduced from [23]. Group 1, 0 – 30 % adipose tissue, represented by the dot-dash line, Group 2, 31 – 84 % adipose tissue, represented by the dashed line, Group 3, 85 – 100 % adipose tissue, represented by the solid line.

In [9], 319 tissue samples were collected from 196 patients undergoing biopsy, lumpectomy, and mastectomy surgeries [9]. The tissue samples were then divided into three groups: healthy, malignant, and benign tissues. The samples were then measured following the same procedure as [23]. The healthy tissues corresponded to the excised tissues from the surgeries that did not contain any lesions or tumorous cells. These samples were then further divided by percentage of adipose tissue. There was no significant difference found in the dielectric properties between the normal tissues from breast reduction [23] and cancer surgeries [9]. This served as a powerful validation that the procedure implemented in [23] could be reproduced in [9] without significant error.

In [9], the malignant tissue samples were categorized into three groups based on the percentage of cancerous tissue within each sample based on a histological assessment. Fig. 2.5 and Fig. 2.6 plot the median permittivity and conductivity for these three groups, respectively. As in Fig. 2.3 the error bars correspond to the 25^{th} and 75^{th} percentile measurements. The variation in the dielectric properties for the malignant tissues samples was found not to be statistically significant [9]. Furthermore, from these plots the variation in the permittivity and conductivity within each group is significantly less than compared to the data from healthy tissue samples.

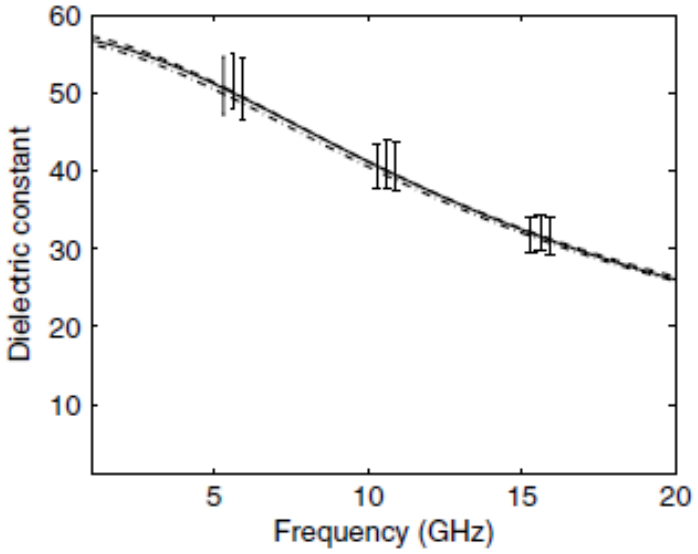

Figure 2.5. Plot of the median relative permittivity for three separate malignant tissue groups, reproduced from [9]. The solid line, dash-dot line, and dash line represent malignant tissue content of higher than 70 %, at least 50 %, and at least 30 % respectively.

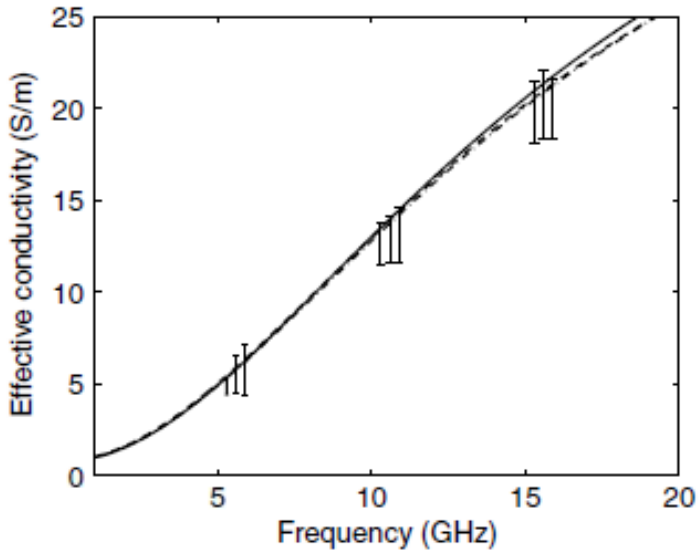

Figure 2.6. Plot of the median electrical conductivity for three separate malignant tissue groups, reproduced from [9]. The solid line, dash-dot line, and dash line represent malignant tissue content of higher than 70 %, at least 50 %, and at least 30 % respectively.

The results from [9] and [23] demonstrate that the permittivity and conductivity of healthy breast tissues cover a wide range at microwave frequencies with the contrast

between malignant and healthy tissue ranging from 10:1 for adipose tissues to only 11:10 for glandular tissues. The combined study in [9] and [23] is frequently referenced, and often used as the basis for the dielectric properties of breast tissues, as it represents the largest study, to date, of excised breast tissue samples. While the popularity of the study is unquestioned, it is important to note that all measurements were performed *ex-vivo* and not time or temperature controlled, both of which can have a significant impact on the dielectric properties of a sample [26].

A recent investigation done at the University of Hiroshima reported on dielectric property measurements of 102 excised samples from 35 patients undergoing breast cancer surgeries [24]. Similarly to [9] and [23], measurements were performed over the 0.5 – 20 GHz frequency range using an open-ended coaxial probe attached to a VNA. In this study, the tissue samples were divided into three types based on a histological analysis: cancer, stroma (glandular), and adipose. The results from this study, permittivity and conductivity for the three tissue types, are shown in Fig. 2.7. This study confirmed that healthy tissues can cover a wide range of permittivity and conductivity. Additionally, there was evidence of overlap between the dielectric properties of the stroma and cancer in certain cases. A second objective of this research study was to quantify the effect that the volume of cancer cells occupy within a sample will have on the dielectric properties. As expected, the dielectric properties were directly correlated to the total volume of cancer cells within the volume; higher volume of cancer cells meant an increased permittivity and conductivity.

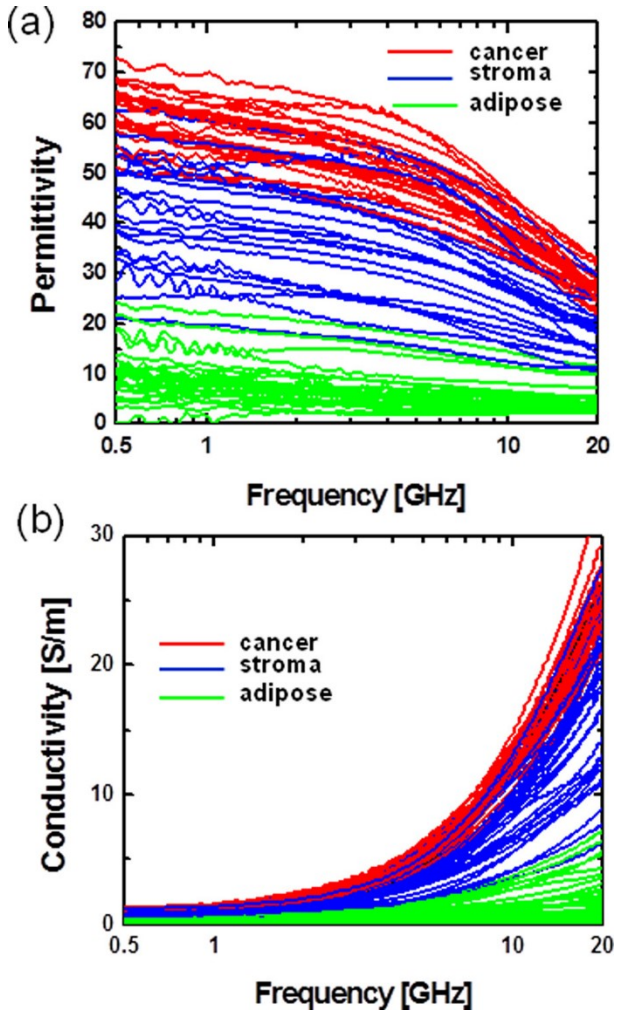

Figure 2.7. A comparison of the relative permittivity (a) and conductivity (b) for the various tissue types found within the breast [24].

The abovementioned studies represent some of the most thoroughly implemented investigations into the characterization of dielectric properties of breast tissues. However, none of these studies could perform temperature controlled *in-vivo* measurements, which would be a more accurate characterization of the tissues. More recently, the results published in [25], call into question the reported results in [9], [23], and [24], as the methods used to characterize the tissue properties relied heavily on coaxial-probe measurements that may have been misinterpreted.

2.3.2 Microwave Techniques for Breast Cancer Screening

Microwave systems can be categorized into three key groups based on their principle of operation: active, passive, and hybrid techniques [8]. Active systems illuminate the breast tissue with EM energy and record the resulting scattered and transmitted energy to detect the presence of abnormalities. Passive methods are based on recording the inherent microwave radiation from the various breast tissues without any sources. One specific passive method, radiometry, can create images of the breast interior by recording thermal emission from the different tissues due to the different metabolic rates of healthy and malign tissues (cancerous cells are very resource intensive) [8], [17]. Hybrid techniques, as the name implies, combine aspects of both active and passive techniques. One of the primary hybrid techniques, microwave-based thermoacoustic imaging, uses microwave energy to uniformly heat the breast tissues. As the tissues are heated and then cooled (microwave source is turned off), the tissues will first expand and then return to their normal size as they cool. This process leads to the production of acoustic waves. A set of transducers can be placed along the breast surface to record these acoustic waves. The inherent contrast in the conductivity of healthy and malignant tissues within the breast will lead to different rates of expansion, and thus different acoustic waves are produced for each tissue. These recorded acoustic waves can then be processed and an image of the breast interior can be formed [8], [17].

Within the scope of breast cancer screening, active systems can be further divided based on their output, imaging or detection, and the basis of operation for the system: time-domain or frequency-domain based measurements.

In the case of microwave imaging, the output image is similar to the current screening protocols. An image of the breast interior is created and the image can then be interpreted to identify the presence of any abnormalities. These images are reconstructed based on

the recorded data from the breast. There are numerous image reconstruction algorithms reported in the literature. These algorithms can be separated into three groups: tomography, radar, and holography [8]. In tomography, the images are formed from a reconstruction of the dielectric profile of the tissues. Two images of the breast are created; one is a profile of the relative permittivity and the other is a profile of the conductivity. Tomographic imaging is both computationally complex and expensive as the reconstruction algorithms require the solution of an ill-posed non-linear inverse problem [17]. In tomography, 2-D images, or slices, are solved for individually and can then be stacked to obtain a 3-D representation of the breast profile. With radar methods a single image of the breast interior is created. This image does not aim to represent the properties of the tissues, but rather it provides a map of the scattered electromagnetic energy. Radar techniques allow for the solution of a complete 3-D problem directly. The most common radar method is confocal imaging, in which a focal point is scanned through a region of interest. The recorded data is then time-shifted to represent this point in space, and the energy is summed. If the energy adds coherently the focal point represents a region of strong electromagnetic scattering [29]. Radar image reconstruction imaging algorithms are typically simpler to implement than tomographic algorithms, however the resultant information is less meaningful [17], [30] (as tomographic images relay information of the actual properties, relative permittivity and conductivity, of the breast interior). Tomography, however, relies on complex algorithms that are less robust and more susceptible to image degradation from measurement noise (due to the high demands on the experimental system) than radar imaging [31]. 3-D holography represents the third imaging reconstruction group. With holography, a 3-D image can be generated in almost real-time. These images represent a contract function of the transmitted wavefronts as opposed to a map of the dielectric properties or a map of electromagnetic scatterers [8].

Unlike a microwave imaging system, with a microwave breast cancer detection system the goal of the system output is to make a decision on whether the recorded data represents a scan of a healthy or cancerous (or even suspicious) breast. This process removes the need for interpretation of an image by a human user. Furthermore, with detection there is no attempt to identify the size or location of the abnormality. Typically, detection algorithms implement some form of machine learning algorithm to classify the breast scan under test. Examples of these machine learning algorithms include Linear Discriminant Analysis (LDA), Support Vector Machines (SVM), and Spiking Neural Networks (SNN) [32] – [34]. These algorithms are trained on a known data set that contains a number of scans from both classes they wish to differentiate (healthy and malign). Then, data from a new scan can be compared to the training set and a decision on that test data can be made. While machine learning algorithms require a significant amount of data to properly train the classifiers, their advantage is that they remove the need for a human to interpret the results of an image.

Microwave systems are primarily divided based on how the system records data; either in the time-domain or frequency-domain. Typically, with a time-domain system, a train of pulses is generated and transmitted to the breast via antennas or sensors. The scattered energy is then recorded and digitized with an oscilloscope (or an equivalent). Frequency-domain systems will transmit a single-tone at a time and then sweep over the desired frequency range of operation. Frequency-domain systems are easily implementable (a standard lab VNA can be used) and offer a higher signal-to-noise ratio (SNR) than time-domain systems as the receiver can be locked to the specific frequency being transmitted. Time-domain systems require both a dedicated pulse generator and oscilloscope to record the data, however, with the recent advances in wireless technology, time-domain systems offer the potential for faster scan times, smaller footprint, and improved cost-effectiveness. The system can also be categorized based on the interaction

between the transmitters and receivers in the system. Typically, there are three types of systems; monostatic (same transmitter and receiver), bistatic (one designated transmitter and receiver pair), and multistatic (multiple simultaneous receivers for each transmitter).

2.3.3 Review of Microwave Systems for Breast Cancer Screening

This section presents an overview of systems for active microwave breast cancer screening. The systems presented in this section are focused on those that have been built and tested experimentally, with a focus on those that have undergone clinical testing. Additionally, where possible, a description of the most up to date version of the hardware of these systems is included. The system prototypes presented here include both frequency-domain and time-domain systems.

At Dartmouth College, research on a clinical prototype for breast imaging using frequency domain measurements for tomography has been underway for more than a decade. Their first system was tested with healthy volunteers in 2000 [35]. The system used 16 monopole antennas arranged in a circular array. The entire antenna array could be moved in the *z-direction* (from the nipple towards the chest wall). A complete breast scan would consist of collecting data with the array at seven distinct z-locations. For each height of the array 240 signals were recorded (data for each transmitter was recorded by the other 15 antennas, each antenna would transmit in turn). Additionally, data was collected at seven discrete frequency points in the 300 – 900 MHz range. Thus, to record all the data necessary for a full 3-D profile of the breast 11760 measurements were necessary. The scan time, per breast, for this initial system was 15 minutes. The patient interface consisted of a tank embedded in a patient bed, with the hardware placed below the bed, unseen to the patient. The tank was filled with a lossy high permittivity medium, saline solution, to provide a match with the skin. The patient would lie in the prone position with the breast submerged in the saline solution; the antenna array would then

be moved inside the tank. This first study had five women volunteers, aged 48 – 76 years, with a range of breast sizes and densities, who all had normal mammograms. The results from this study demonstrated that data recorded from a microwave system agreed with reports from X-ray mammography in determining the radiological breast density. In [36] and [37], the system was tested clinically for two specific applications: detecting the presence of a tumour within the breast and to monitor the progress and changes to a tumour during chemotherapy treatment. Over the years several changes had been made to both the hardware and software. For the scans performed in [36] and [37] the immersion tank was now filled with a glycerine:water solution varying from a 80:20 ratio to 86:14, depending on the density of the breast based on X-ray results. In [36], data was recorded at eleven frequency points up to 3 GHz, with 1.3 GHz being reported as the optimal operation frequency. In [37], data was recorded between 700MHz and 1.7 GHz at 200 MHz intervals. In both cases, as with the original system, data was acquired at 7 distinct locations in the *z*-direction. The hardware and software changes allowed for scans to be completed in under five minutes per breast, with a reported noise floor of -140dBm and channel-channel isolation of 150dB [36]. In [36], results for two patients were included, demonstrating that the prototype was successful in identifying the presence of a tumour and then subsequently tracking the changes in size of the tumour during chemotherapy. In [37], 8 patients were followed during chemotherapy, and once again the system demonstrated successful tracking of the changes in the tumour size during treatment. These two studies demonstrated that a microwave system can also be a useful tool in providing an alternative method to track the progression of chemotherapy treatment with non-invasive imaging. Most recently, the latest prototype of the system was presented in [38]. Figure 2.8 shows the latest system prototype and some of the components. In this 3rd generation of the system, many of the electrical components have been replaced by custom built solutions, reducing the footprint and cost of the system. The system can

operate from 500 MHz – 2.3 GHz and achieve a dynamic range over 110 dB. Additionally, the circular array of 16 antennas has been grouped into two groups of 8 antennas. Now each group could be moved to specific planes as desired, allowing for cross-plane measurements. The performance of the system was validated with phantom measurements in [38].

Figure 2.8. Photographs of the system components from [38]. (Left) The system's main compartmentalized components: 1 – Interface between the immersion tank and liquid, 2 – the microwave electronic networks, 3 – the data acquisition components, 4 – the power supplies. (Middle) The immersion tank and antenna array, attached to the liquid reservoir and the microwave electronic network. (Right) The complete system as it appears in the clinic.

At the University of Calgary, a monostatic radar-based wideband system has been developed and successfully tested with patients [39] – [41]. The system, named the tissue sensing adaptive radar (TSAR) prototype, is somewhat similar to the system developed at Dartmouth. The patient interface is embedded into a clinical table with the patient lying in the prone position with the breast placed in a cylindrical tank filled with an immersion medium, in this case canola oil is used. The system utilizes a single antenna that is mechanically scanned to over 200 positions. Reflection data, S_{11}, is recorded with a VNA at 1601 points over the 50 MHz to 15 GHz range. An image of the breast is formed by convolving the recorded data with a differentiated Gaussian pulse centred at 4 GHz and then applying confocal imaging. In [40], results from an initial clinical trial with eight patients is presented. The patients ranged in age from 32 to 64 years with a cup size of B

or C. For this patient study the antenna position for each scan was dictated by the size of the patient's breast; there were anywhere from five to nine distinct heights, with between 20 to 30 locations per height. The antenna scan positions were defined over a cylindrical pattern around the breast. The antenna is attached to an arm that rotates around the tank. Also attached to this arm is a laser to estimate the distance between the antenna and the skin. Each breast scan takes approximately 30 minutes. In this study, each patient also underwent an MRI for comparison purposes. A direct comparison between the TSAR images and MRI is quite difficult due to the different positioning of the breast; however, the results from [40] are promising as the majority of the images obtained were found to be consistent with the clinical histories of the patients, with the lesions correctly identified and localized in several cases. An image of the patient interface from [40] is shown in Fig. 2.9.

More recently, in [41], an investigation on optimal antenna localization was carried out. Due to recent hardware changes in the TSAR system it is now possible to place the antenna at any arbitrary location within the tank, it is no longer limited to a cylindrical scan pattern. To help identify the optimal scan pattern, three specific scan patterns were investigated: cylindrical, hemispherical, and patient specific. The patient specific scan pattern is defined by first using a laser camera to create a rough profile of the breast surface and then placing and orienting the antenna to maximize the signal that is transmitted within the breast based on that profile. The results from [41], based on numerical simulations with MRI-derived breast models, demonstrate that the patient specific scan pattern allows for the generation of accurate images even in the most challenging of scenarios and out performs both the hemispherical and cylindrical configurations; the hemispherical configuration outperforms the cylindrical configuration. This improvement in performance comes at the cost of longer scan times; the data

acquisition time is increased by 30% for the patient specific scan in comparison to the cylindrical scan [41].

Finally, in [42], the group at the University of Calgary has demonstrated the functionality of a simple system to estimate the bulk dielectric permittivity of the breast. This information can help improve the image reconstruction capabilities of the TSAR system as an estimate of the breast permittivity is necessary in confocal imaging.

Figure 2.9. A photograph of the TSAR system from [40]. Certain components, VNA, EM absorbers, the cable guiding system for the moving antenna, are labelled in the photograph.

An experimental microwave radar system was also developed at the University of Bristol [43], [44]. The initial prototype consisted of a 31-element antenna array integrated into a hemispherical ceramic shell, $\varepsilon_r = 10$, in which the breast or breast phantom is placed. The antennas are connected to a VNA through a custom-built electromechanical switching matrix made from a cascade of 8x1 and 2x1 switches. The system records the transmitted (S_{21}) data for the system for each possible antenna pair. By using a multiport VNA an entire scan can be completed in under three minutes. The system creates images based on a differential analysis. The system records a second scan of the same breast by

rotating the antenna array; the difference of the two scans is used to extract the tumour response. Successful detection with tumours as small as 7mm in diameter was demonstrated with this system in [44]. The system was then tested in a small clinical trial with two patients in [45], while the results were mixed in terms of the performance of the system, this study served to identify key issues including patient movement, mismatch between the breast shape and the array structure, and time to properly position the patient. More recently, the system was upgraded to now use a 60-element antenna array that operates over the 3 – 8 GHz range. This updated system can complete a scan of the breast in only 10 seconds [46]. In 2016, the latest iteration of this prototype was used in a clinical trial with 86 patients with the images generated from the system compared to mammogram images [47]. The system reported a detection rate of 74% compared to 83% detection rate of an experienced radiologist interpreting the mammogram images. Interestingly, the results from the system prototype outperformed the radiologist when imaging women with dense breasts, 86% to 79%. The results from [47] demonstrate that the results from a microwave system prototype compare favourably to the current detection method of mammogram images interpreted by a radiologist. An example of the system setup from [47] is shown in Fig. 2.10.

At the University of Manitoba, two different experimental systems were developed. A 24-antenna system was demonstrated in [48] to detect multiple scatterers using tomographic imaging. The antenna array was connected to a VNA via a switching matrix. An image of the system is shown in Fig. 2.11.

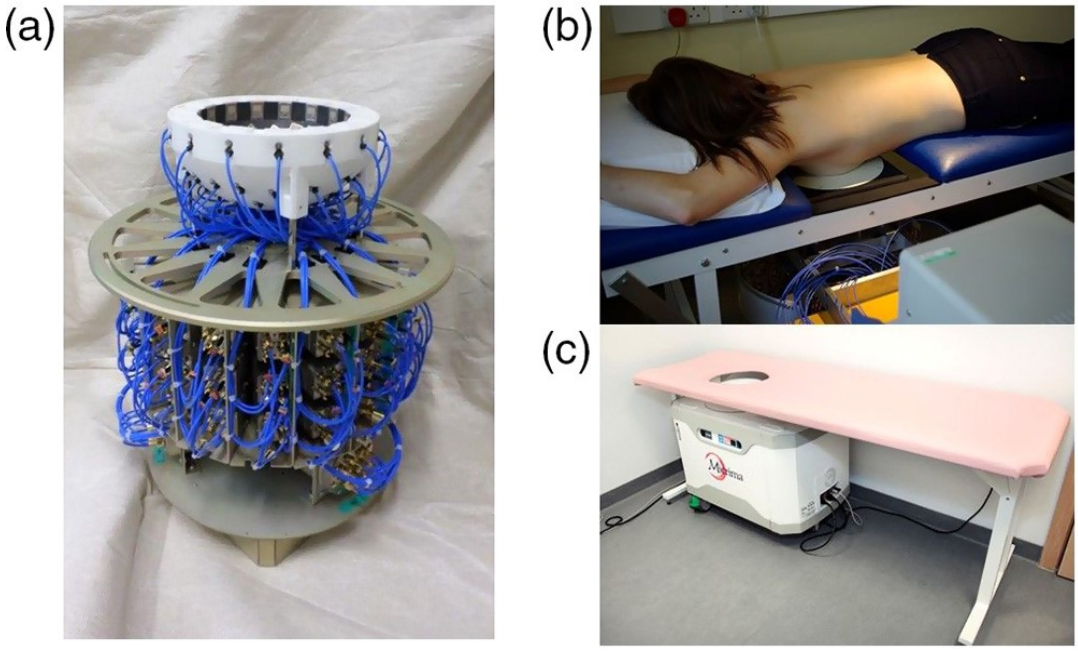

Figure 2.10. Images of the system setup developed at the University of Bristol [47]. (a) An image of the 60-element antenna array and the connections with the electromechanical switching matrix. (b) A patient undergoing an exam with the system prototype from [47]. (c) An image of the latest, more compact, and user friendly design of the system in [47].

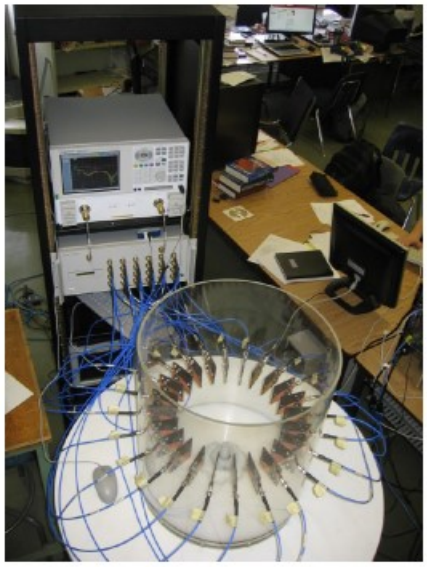

Figure 2.11. An image of the system at the University of Manitoba for tomographic imaging [48].

A second system using a single Vivaldi antenna immersed in an oil tank was also developed [49], [50]. This system records monostatic data using a VNA over the 1 – 6 GHz range. The phantom is rotated by 5° increments such that a circular scanning region is emulated. In [50] the system was tested with six phantoms; three to emulate low-density breasts and the other three phantoms contained significant amount of glandular tissues. Images of these phantoms were reconstructed using circular holography. This technique allowed images to be formed in an average time of 5 ms [50]. The system was able to successfully detect and locate malignant lesions 8 mm in size in each phantom that contained the tumour mimicking materials. More recently, this system was used to explore the application of classification techniques on experimental data [51].

In [31], researchers from the Chalmers University of Technology contrast the performance of frequency-domain and time-domain versions of the same system; using the same antenna array system they simply change the signal generation/recording equipment for the two systems. For the frequency-domain measurements a VNA and a switching matrix is used; the time-domain system consists of the same switching matrix, a pulse generator that creates a 75 ps wide Gaussian pulse, triggered by an external clock, and a high speed oscilloscope to record the data. This work provides the first comparative study between the two types of measurement systems. The remainder of the system consists of 20 monopole antenna evenly spaced along a 10-cm radius around the object under test. Data was collected from simple homogeneous phantoms in both tests. In [31], it was concluded that the SNR and dynamic range for frequency-domain measurements were higher than their time-domain equivalent; however, the reconstructed images of the simple phantoms were well matched. More recent work has focused on the development of custom-built low-cost solutions for time-domain systems to replace some of the bulky components. In [52], the authors have demonstrated that a low-cost equivalent-time sampling circuit can be built from generic components to replace the expensive high speed

oscilloscopes often used in time-domain system. Most recently, in [53], the authors have investigated the use of different types of pulses as the input for a time-domain system. The authors have looked into using a pseudo-random sequence (M-sequence) signals. In [53] they demonstrate that the use of these M-sequence signals can improve the SNR of a time-domain system. However, this improvement seems to be limited to low-loss environments. In a complex and lossy environment such as the breast there does not seem to be anything gained from using these M-sequence signals over a pulse train.

At the University of Hiroshima, the research focus has been on the development of custom-built CMOS technologies to replace the large, bulky, and expensive components often found in microwave systems. The group has developed their own custom built switching matrix, Gaussian monocycle pulse generator, and equivalent-time sampling circuit [54]. Utilizing a planar 4x4 antenna array, that is mechanically scanned across a rectangular phantom, they have demonstrated successful imaging of a tumour embedded within the phantom [54]. An example of the circuitry of this system is shown in Fig. 2.12.

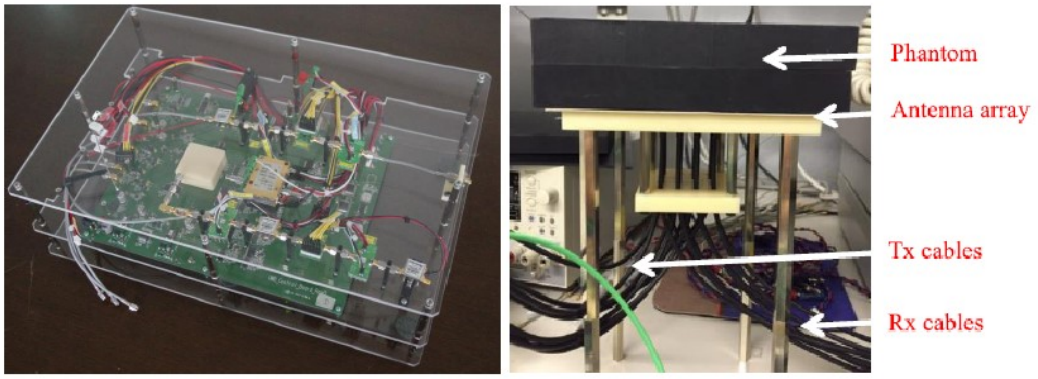

Figure 2.12. Photographs of the system in [54]. (Left) The custom-built electronics for the pulse generation, switching matrix, and data acquisition. (Right) Photo of the integration of the system and the phantom under test.

2.4 Related Medical Microwave Systems

The systems discussed in Section 2.3.3 were focused solely on applications to breast cancer detection. However, the benefits of microwave systems can extend to numerous applications ranging from stroke detection [55], head imaging [56], [57], bladder monitoring [58], [59], bone imaging [60], to therapeutic applications such as hyperthermia for head and neck traumas [61], [62].

The hardware advancements presented in this thesis are focused on the integration with a breast cancer screening system; however, these advancements can be applied to any of the above listed applications.

Chapter 3: Initial Time-Domain Microwave System

In this chapter, a summary of the comprehensive experimental results obtained from a first-generation experimental time-domain microwave system, developed at McGill University for breast health monitoring, is presented. This chapter focuses on summarizing the key results from several papers, namely, those focused on: the design and initial testing of the system with realistic tissue mimicking breast phantoms [63] – [69], the development of a clinical interface for testing with healthy patient volunteers [70] – [76], and the development of signal processing methods for improved detection capabilities [77] – [79]. The novel contributions discussed in this section are: i) the design of a first-generation time-domain prototype for microwave breast screening; ii) development of a clinically ready interface for testing with healthy human volunteers; iii) the implementation of classification algorithms with experimentally obtained data.

This chapter is further broken into several sections; first, a general system description is presented, followed by a summary of the fabrication of realistically shaped tissue-mimicking breast phantoms. The initial results of testing the system with these breast phantoms and then with healthy volunteers follows. The chapter concludes with a discussion on signal processing methods that have been developed to improve the detection capabilities of the system.

3.1 System Description

The objective for the time-domain microwave system is to the detect the growth of abnormalities within the breast at an early stage and identify these abnormalities as cancer. The proposed method of employment of this system is as a monitoring device, wherein frequent breast scans can be conducted. As the microwave system is safe and scans are cost-effective, such a regular screening protocol can be implemented. Individuals

who are known to be healthy would undergo routine scans repeated at pre-determined intervals such that the scans occur during the same phase of the menstrual cycle (as changes in breast density occur during the luteal and follicular phases) [80], [81]. In this way, data is accumulated across a set of breast scans. By creating a temporal profile of changes in the breast, the demands on the technology and signal processing are reduced. The system design choices and experimental validation presented in this thesis are all made with this end goal in mind.

The experimental system presented in [63] – [66] is a time-domain microwave radar system. The system operates as follows. A generic impulse generator (Picosecond Pulse Labs model 3600), which is triggered by a clock generator (Tektronix gigaBERT 1400 generator) operating at 25 MHz, generates quasi-Lorentizian impulses of 70ps full-width half-maximum (FWHM) at -7.5V peak amplitude. These pulses are then re-shaped using a custom-built reflection-mode microstrip filter (referred to as a Synthetic Broadband Reflector, SBR) so that the resulting pulses have the majority of their energy concentrated in the 2 – 4 GHz range [64]. This frequency band represents a trade-off between the attenuation experienced within the lossy breast tissues at high frequencies, and limitations on antenna performance and size at low frequencies [64]. This reshaped pulse is then amplified by +35 dBm, (Mini-Circuits ZVE-3W-83+, maximum output power = 33dBm), resulting in a signal amplitude of 15.8 V p-p, prior to being sent to a custom-built automated electromechanical switching matrix. An antenna array consisting of 16 elements held on the exterior of a hollow, hemi-spherical antenna radome is connected to the switching matrix. This electromechanical switching matrix is built from a cascade of 2×1 and 8×1 switches, and ultimately represents a 16×2 switching matrix; allowing each of the 16 antennas to be connected to either the transmit (TX) or receive (RX) port. After transmission through the breast (or phantom), the scattered signal response is picked up by the receiving antenna, which is connected to the sampling input of a

digitizing oscilloscope (picoTechnology PicoScope 9201 sampling oscilloscope), and the data is transmitted to a laptop for analysis. A block diagram of the system setup is shown in

Fig. 3.1.

The radome is fabricated from alumina (Al_2O_3), $\varepsilon_r = 9.6$, and provides a rigid housing structure for both the antennas and the breast phantoms (or any material under test). Alumina was chosen as it provides a stable material to hold the antennas and material under test while also exhibiting dielectric properties similar to adipose tissue, which the antenna was designed to be in proximity to. The purpose of the radome is two-fold: i) to improve antenna performance by providing better matching at the antenna launch, and ii) to ensure that the antennas are always in the same position relative to each other and the breast phantom. The radome consists of 16 antenna slots organized in a 4x4 grid. Of the 16 slots, there are 12 co-polarized slots (antennas with the same orientation with respect to each other) and 4 cross-polarized slots (antennas oriented at 90° with respect to each other). A photograph of the fabricated radome is shown in Fig. 3.2.

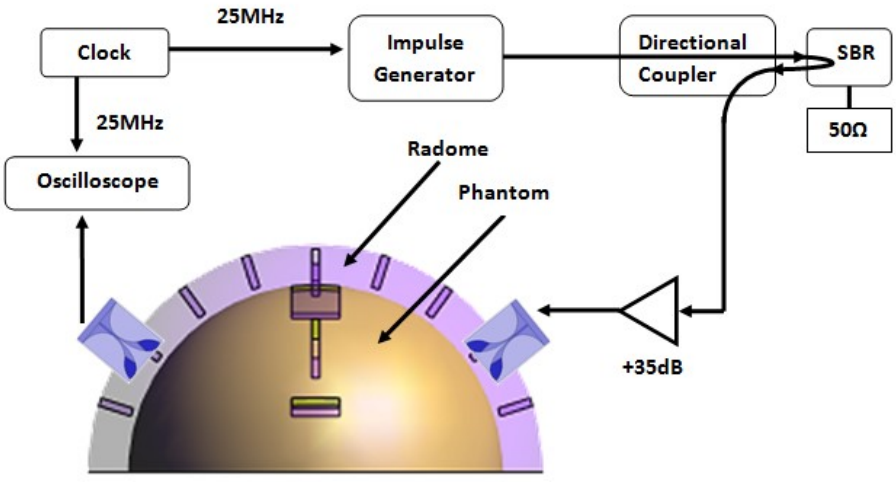

Figure 3.1. A high-level depiction of the complete experimental setup. The setup includes a clock to drive the pulse generator, a directional coupler to route the signal from the SBR structure towards the antenna, a radome to house the antennas and the breast phantom, and an oscilloscope to record the time-domain data [64].

Figure 3.2. A photograph of the fabricated radome demonstrating the relationship of the antenna slots to each other [64].

The antenna used in this experimental system is the Traveling Wave Tapered and Loaded Transmission Line Antenna (TWTLTLA), designed specifically for biosensing applications [82]. The antenna is a compact wideband antenna, measuring 0.635 x 12 x 18 mm^3. A plot of the antenna performance when embedded within the radome filled with a tissue-mimicking material is presented in Fig. 3.3, along with an inset image of the fabricated antenna. The antenna demonstrates good transmission from about 3 – 12 GHz, with an S_{11} below -10 dB. At frequencies below 2 GHz the S_{11} exceeds -5 dB, indicating that the antenna is not transmitting a significant amount of the input energy in this range.

An example of the complete experimental system setup is shown in Fig. 3.4. A photograph of the experimental system from the laboratory bench is shown. This image allows the reader to envision the overall size of the initial experimental system. The impulse generator, clock generator, and the oscilloscope are the commercial equipment located at the right of the image (from bottom to top, respectively). The antenna radome and switching matrix are located at the centre of the photograph. The antennas embedded in the radome are connected to the switching matrix and the TX and RX ports through

a series of semi-rigid SMA cables. In total, there are 50 such RF cables in this initial experimental system. A laptop is used to automate the data acquisition process by communicating with the switching matrix and the PicoScope. A cost analysis of each of these components, based on the components approximate value at the time of purchase, and the total cost for this first-generation prototype is presented in Table 3.1.

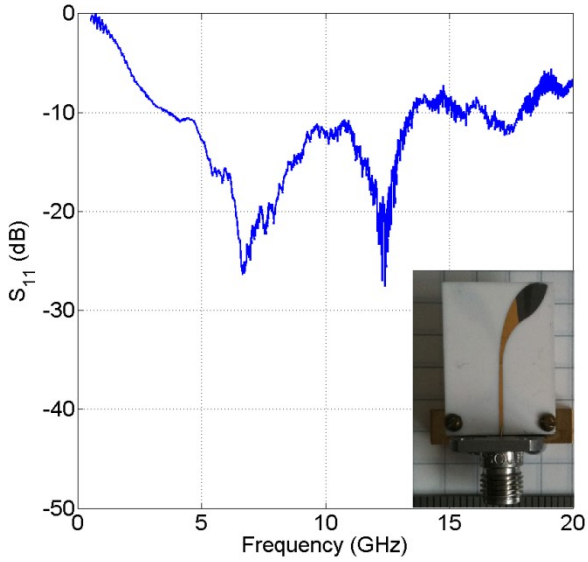

Figure 3.3. A plot of the S_{11} of the antenna embedded within the radome. The antenna operates with S_{11} < -10 dB over the 3 – 12 GHz bandwidth. At low frequencies the antenna is reflecting rather than transmitting much of the incident power. The inset is a photograph of the fabricated antenna [64].

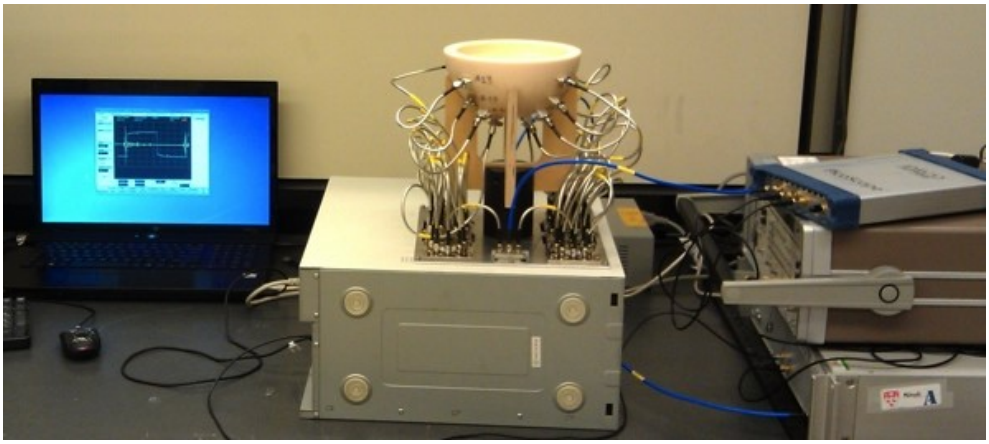

Figure 3.4. A photograph of the experimental system. The radome is the hemispherical bowl in the center

of the image, with the antennas attached to its exterior surface. Also visible is the clock, pulse generator, switching matrix, oscilloscope, and the recording computer.

TABLE 3.1. COST ANALYSIS OF THE INITIAL EXPERIMENTAL SYSTEM

Equipment	Estimated Cost (CAD $)
Tektronix gigaBERT 1400 generator	20 000
Picosecond Pulse Labs Model 3600 (now owned by Tektronix)	30 000
Custom-Built Switching Matrix	10 000
SMA cables (50)	5 000
Radome	3 000
Antenna Fabrication	1 500
picoTechnology PicoScope 9201	17 000
Power Supplies	500
Total System Cost	87 000

3.1.1 Data Acquisition

Each measurement is recorded with a pair of antennas; one antenna is the transmitter while another antenna is the receiver. The switching matrix allows for all possible antenna transmit-receive pairs to be connected, therefore, each scan with the system consists of performing 240 distinct measurements (16 transmit antennas $\times$ 15 receiving antennas). The PicoScope operates based on equivalent-time sampling; by taking advantage of the relatively slow changing human processes and the periodic nature of the transmitted pulses, a very high effective sampling rate can be achieved with a much slower real-time sampling rate. The PicoScope allows for the selection of a range of sampling rates; the work with this experimental system has focused on recording data with anywhere from 40 GSa/s [72] – [75] to 200 GSa/s [83]. The primary trade-off between the higher sampling

rate is longer scan times. The trade-off is approximately linear; a scan at 40 GSa/s will take approximately 90 seconds, while a scan at 200 GSa/s will take approximately 6 minutes. The other trade-off with the sampling rate is the time between samples. This can have an effect on the use of noise reduction techniques [84]; however, this may also be overcome by the use of interpolation in post processing. The PicoScope also offers the ability for hardware averaging by performing successive scans. This process is very useful in reducing random measurement noise in the system; using 16 hardware averages reduces the noise-floor of the system to approximately 1.5 mV (-47 dBm); with 16 averages the dynamic range of the system is 75 dB. As with the sampling rate, there is a direct link between the number of averages used and the scan time. Testing of the system has demonstrated there is little to no improvement going beyond 16 averages [70], [83].

A custom-built data acquisition program allows for the data for an entire scan to be recorded by a 'one-click' operation. Additionally, this software has the option to interface with the PicoScope to set the sampling rate and the number of averages, and to perform multiple scans of the same material under test successively. The data acquisition program communicates with both the switching matrix and the PicoScope, ensuring that the transmit-receive pairs are only switched after the data has been obtained from the PicoScope for a specific scan. The switching matrix is controlled through a custom-designed data acquisition program from a laptop. A microcontroller (STMicroelectronics model STM32-F4 Discovery board) is used to provide the link between the logic of the data acquisition program and each switch in the specific TX-RX chain.

The end result of each scan is a set of 240 signals that are saved onto the laptop connected to the Picoscope. These 240 signals form the entire data set for a specific scan and can be analysed to make a decision on whether the scan represents a healthy breast or whether there is the presence of a cancerous abnormality.

When using the system to create images of the material under test a differential calibration method is used. As the goal for the system is for a monitoring application for breast cancer screening, it is believed that access to an initial healthy scan will be available. This healthy scan represents a calibration data set. A differential data set is then created by subtracting the calibration data set from the latest data set. Additionally, an extended use of this system is to monitor the treatment of breast cancer; in that case the initial scan represents the unhealthy scan, each subsequent scan would then be compared to this scan and changes in the tumour size can be tracked. This calibration procedure removes the early-time signal response. The early-time signal response can be defined as the signal that represents the effects of antenna coupling (signal travelling directly between the two antennas), reflections from the radome walls, and background noise.

When using phantoms, this results in performing two measurements to create this differential data set. First, a scan of the 'healthy' breast phantom (no embedded tumour) is performed, representing the calibration data set or baseline. Then, a tumour phantom is embedded into the healthy breast phantom and a new scan is done, this represent the tumour data set. The differential data set is then found from subtracting the baseline data from the tumour scan. The differential data set can then be used for analysis.

To perform these measurements, the chosen phantom is placed into the radome surrounded by a thin layer of ultrasound gel. The ultrasound gel fills any air gaps between the breast surface and the radome. As ultrasound gel is a water-based material it has similar dielectric properties to water. Ultrasound gel is chosen for use as the breast immersion medium because of its favourable electrical and mechanical properties: it is lossy, so it attenuates unwanted multiple reflections between the skin and the radome wall [38], [63], and it conforms well to the breast shape without the spill risk of a liquid.

Ultrasound gel has been previously approved for medical use and is commonly available in hospitals and clinics.

3.2 Tissue and Breast Phantom Fabrication Summary

The use of tissue phantoms allows for the validation and testing of novel microwave systems in advance of a clinical trial. Tissue-mimicking phantoms are ideal for system design testing as they represent a less challenging scenario from the complexity of the human breast. Furthermore, the use of breast phantoms for a microwave breast screening device allow for the control of several factors, including; known breast composition (governed by the dielectric properties of the tissue-mimicking materials) and size, and tumour size and location. Previous work has focused on the development of anatomically realistic phantoms, in terms of both the physical appearance and the dielectric properties [67] – [69]. These phantoms can be fabricated from readily-available chemicals, but are primarily made from a mixture of oil-water-gelatin. The oil:water ratio of the mixture determines the permittivity and conductivity of the tissue mimicking materials. This process can be followed to create tissue phantoms that can accurately mimic the various tissues of the breast; namely, skin, fat, gland, and tumour tissues. The process of fabricating the complex breast phantoms can be summarized as follows: a skin layer is first made by compressing a skin tissue mimicking phantom between two skin moulds. Once the mixture is allowed to harden (24 hours is sufficient), the moulds can be removed. The result is a skin layer with a desired thickness, this thickness can be controlled by the amount of pressure used during compression. Then, conical glandular structures can be fabricated by pouring the gland tissue mimicking phantom into conical moulds. Once these structures have hardened they can be arranged and placed within the skin mould. The density of the breast phantom can be varied by changing the number of glandular

structures included in the phantom. Finally, the fat tissue mimicking phantom is poured into the skin mould, filling the gaps between the glandular structures and completing the breast phantom. An image of the skin mould with the embedded conical glandular structures, and the finalized heterogeneous realistically shaped breast phantom is shown in Fig. 3.5. Tumour tissue-mimicking phantoms can be fabricated and then carved into the desired shape. These tumours can then be embedded into the breast at the desired location.

Figure 3.5. An example of the heterogeneous breast phantoms. (Left) A photograph of the 2-mm skin layer and the conical gland structures embedded inside the phantom. (Right) An example of the realistically shaped breast phantom, exterior only [64].

The dielectric properties of these breast phantoms are highly dependent on the exact oil:water ratio. It is therefore straightforward to create a wide range of variation in the tissue phantoms to emulate the diversity of breast densities found within the human population, as reported in the literature in [23]. As an example of this, four healthy breast phantoms (skin layer filled with fatty tissue) are fabricated using four different oil:water ratios; similarly, four tumour-mimicking phantoms with varying ratios are made. Using a dielectric probe (Agilent HP85070E) connected to a microwave network analyser (Agilent

N5242A PNA-X) the dielectric properties were recorded at four locations on each of the four breast and tumour phantoms [78]. Fig. 3.6 and Fig. 3.7 show the measurement results for the healthy and tumour phantoms, respectively. These results confirmed that breast phantoms representing a range of different breast densities can be fabricated.

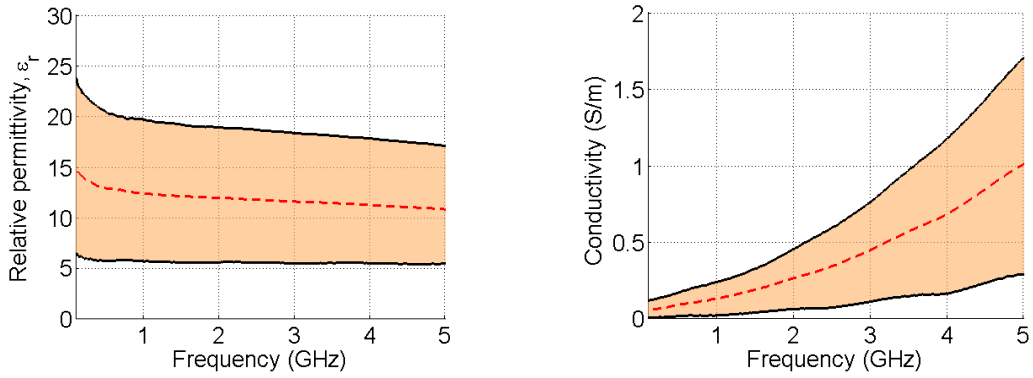

Figure 3.6. Plot of the measured variation in relative permittivity (left) and conductivity (right) for the healthy tissue phantoms. The red dashed line in the middle is the average while the black solid outer bounds of the shaded region represent the maximum and minimum measured values [78].

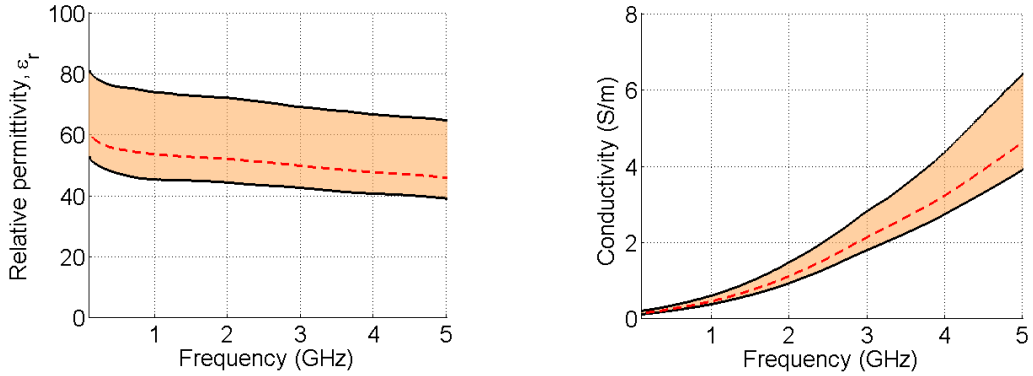

Figure 3.7. Plot of the measured variation in relative permittivity (left) and conductivity (right) for the tumor phantom. The red dashed line in the middle is the average while the black solid outer bounds of the shaded region represent the maximum and minimum measured values [78].

3.3 Initial Experimental Results

In this section, results related to the initial system testing with breast phantoms are presented. The results from these initial investigations into the system functionality serve as validation that the implemented system can detect tumours embedded in different breast phantoms. First, an analysis of the recorded time-domain signals is presented. This analysis represents an investigation in determining whether the system can detect the different signals that are reflected and scattered when a tumour is embedded in a healthy phantom. Following this discussion, the system functionality is further verified by using image reconstruction techniques to create images of the breast phantoms; demonstrating that the system can be used to detect and even localize the presence of an embedded tumour.

In [64], data was recorded from realistically-shaped breast phantoms that were made up of 100% fat (purely homogeneous), and heterogeneous phantoms of 60%, 70%, and 80% glandular tissues. All phantoms had a thin skin layer approximately 2 mm thick. A scan was done on each breast phantom (healthy baseline); then a spherical 1-cm radium tumour phantom is embedded in each phantom and a new scan is taken (tumour scan). To embed the tumour a hole is carved into the phantom at the desired location, and the excess phantom tissue is removed. After this process the phantom can no longer be used as a healthy baseline as it has been damaged. A 1-cm radius tumour is chosen as it represents the limit for Stage I diagnosis of breast cancer [1] – [3]. The tumour response signal is defined as the difference between the recorded healthy baseline signal and the recorded signal when the tumour is embedded into the given breast phantom. The differential data set, defined in Chapter 3.1, is composed of the tumour response signal from all possible channels. It represents the changes in breast tissue occurring between the current scan time and a previous scan in time. Assuming the system functions

correctly, the tumour response signal should be a time-shifted and lower amplitude signal when compared to the response from the entire breast.

A comparison of the computed tumour response signals for the purely adipose phantom (left) and the 80% glandular content phantom (right) is shown in Fig. 3.8. In both cases, the signal is recorded from nearest-neighbour antennas on the same side of the radome. Each plot in the figure contains two signals; the signal recorded directly from the PicoScope (shown in blue), and the tumour response signal (shown in red). In both cases, the tumour response is delayed relative to the main pulse and is of smaller amplitude. Further, the tumour response for the 80% glandular phantom has lower amplitude than the tumour response of the pure adipose phantom, which is as expected since the glandular phantom is a more lossy environment than the adipose phantom.

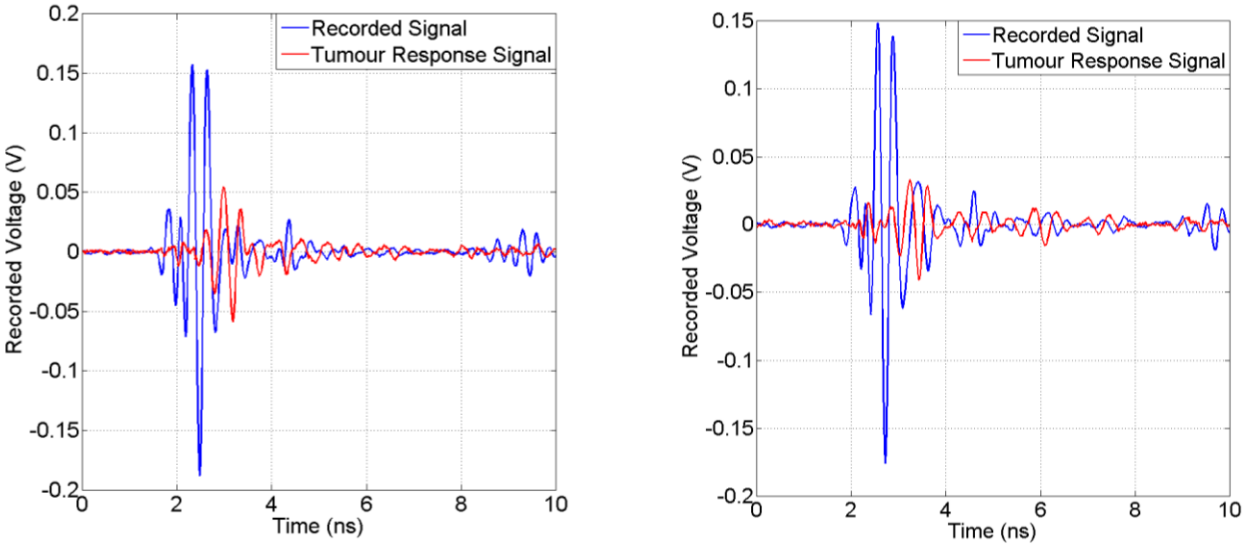

Figure 3.8. Time-domain comparison of the recorded signal and the tumour response signal for both the (left) fat (right) gland [64].

To further verify that the difference signal actually represents the response from the tumour, and not measurement differences between the two scans, the delay between the peak of the tumour response signal and the recorded signal can be computed. Since the

location of the tumour is known in the experimental setup, the approximate time delay between these two peaks can be computed:

$$\tau = \frac{\Delta x \sqrt{\varepsilon_r}}{c} \quad (3.1),$$

where c is the speed of light, ε_r is the relative permittivity of the breast phantom, and Δx is the difference in the path-length for the signal that travels between the two antennas (peak signal) and the signal that is reflected off the tumour. Since the approximate permittivity of each phantom is known, an estimate on the time delay between the peaks can computed for each phantom using equation (3.1). The estimated delay for the purely adipose phantom is 580 ps and 1100 ps for the 80% gland phantom. The measured time delays from Fig. 3.8 are 625 ps and 850 ps for the 100% adipose and the 80% gland phantom, respectively [64]. The calculated and measured time delays are well matched given the assumptions of the calculation. For example, the larger error in the heterogeneous 80% gland phantom can be explained by how the estimated delay is calculated; it assumes that the tissues in the path are composed of exactly 80% glandular tissue, whereas in reality the tissues directly in front of the antennas in the phantom may not be at exactly this ratio (based on the measured delay, one can expect the glandular content was in fact lower than 80%).

Reconstruction images of the breast phantom under test can be created from the differential data set. These images serve to further validate the system's functionality and detection capabilities as these reconstruction images require that the tumour response signal be recorded from numerous transmit-receive antenna channels.

Prior to implementing the image reconstruction algorithm, several pre-processing steps have been identified to greatly improve the quality of the reconstructed image [65]. These pre-processing steps can be summarised as follows: the data is time-aligned using two methods, first, the recorded data is aligned based on the reference clock signal that is used to trigger the pulse generator. This alignment procedure mitigates the jitter

inherent in the clock signal. Second, a correlation alignment of the early-time response of the signal is used to mitigate any other sources of jitter (impulse generator, amplifier, PicoScope, equipment drift), the data is then filtered using a Gaussian band pass filter over the frequency range of interest, as suggested in [85], and finally the data is windowed to reduce computational time. The Delay-and-Sum (DAS) algorithm was the first image reconstruction algorithm applied to time-domain data for microwave imaging of the breast [29], [85]. More recently, however, the Delay-Multiply-and-Sum (DMAS) image reconstruction algorithm has been reported [86]. These confocal imaging algorithms create a 3-D image which provides a profile of the intensity of the (EM) scatterers within the volume. While this algorithm is not the most robust, it easily allows for system testing (as opposed to algorithm development).

In [63], two homogeneous (100% adipose tissue, with a 2-mm thick skin layer) realistically-shaped breast phantoms are fabricated and tested with the system. A 1-cm radius spherical tumour is embedded in each phantom at different locations; in the first phantom the tumour is embedded on the left side of the phantom (this is denoted as Position A), for the second phantom, the tumour is embedded on the right side of the phantom (denoted as Position B). The tumours are centred at a depth of about 2 cm from the chest wall. The differential data set representing the tumour response signals are obtained, and these signals are used with the DMAS algorithm to create the reconstruction images of the breast phantom.

A 2-D coronal slice of the reconstructed 3-D image for each phantom is shown in Fig. 3.9. The 2-D coronal slice is chosen at a depth where the global maximum intensity is located; the global maximum represents the strongest EM scatterer throughout the entire 3-D image, which, assuming successful detection, is the embedded tumour. Within these images, dark red indicates regions of strong EM scattering, while dark blue suggests very weak EM scattering. The images are normalized to the global maximum.

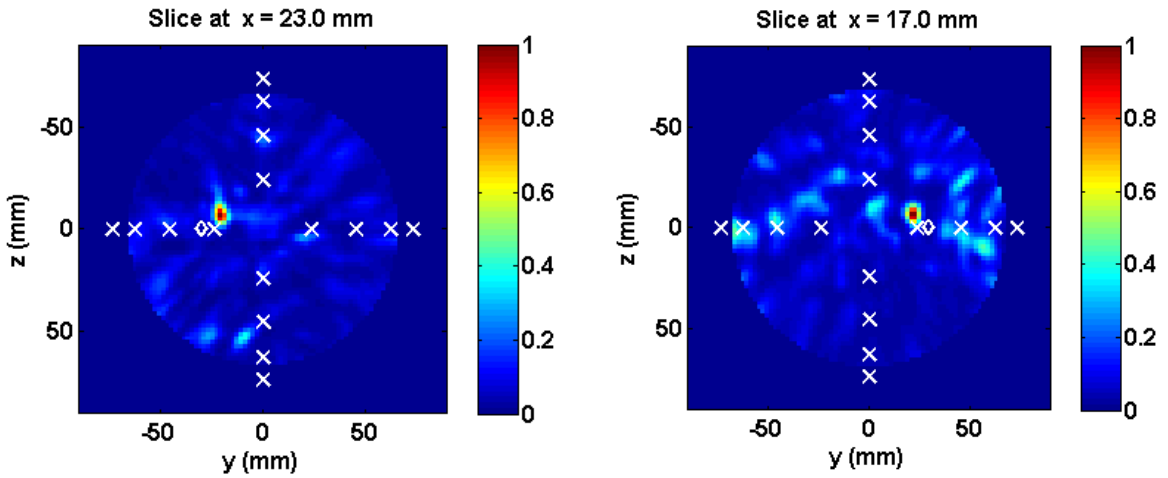

Figure 3.9. Image of a breast phantom with a tumour in Position A (left), slice depth x = 23 mm is from the chest wall. Image of a breast phantom with a tumour in Position B (right), slice is at a depth x = 17 mm from the chest wall. The "×" markers represent the positions of the antennas, and the diamond marks the actual location of the tumour center [65].

It is clear from Fig. 3.9 that in both cases the tumour is easily identified as the maximum scatterer and well localized. To quantify this detection, two metrics have been defined in [65]; the signal-to-clutter ration (SCR), defined as the ratio between the intensity at the tumour location and the next highest intensity in the 3-D image, and the tumour localization error, defined as the distance between the global maximum in the image and the true tumour location. These metrics are calculated for both phantoms (tumour at Position A and Position B) and shown in Table 3.2. The localization error is defined based on the 2-D error in the y-z plane, as the global maximum occurs in the range of depths in which the tumour is located (from 1 – 3 cm). The average localization error is 11 mm and 7 mm in the y- and z- direction respectively. One factor that can impact the localization error is the fact that the tumour is embedded by hand, and as such may not be at the exact location used in the localization error calculation. The SCR for Position A and Position B is 8.2 and 6.8 dB, respectively, demonstrating that the response from the tumour is significantly above the healthy background.

TABLE 3.2. SUMMARY OF IMAGE PARAMETERS FOR TUMOURS IN POSITIONS A AND B: SIGNAL-TO-CLUTTER RATIO (SCR) AND TUMOUR LOCALIZATION ERROR [65].

	Position A	Position B
SCR (dB)	8.2	6.8
Error (y, z) (mm)	(9, 7)	(13, 7)

3.4 Development of a Clinically-Ready Prototype

Following the successful demonstration of the system's capabilities to detect tumours in a variety of breast phantoms, clinical trials involving human patients were targeted. The aims for these initial clinical trials were to record user feedback (comfort, ease of use, any other concerns), demonstrate the repeatability of measurements with the system, and characterize how the system would perceive the healthy variations in the breast by monitoring patients. These results were presented in [70] – [76].

As part of an initial clinical trial with healthy volunteers, the system was modified to accommodate scans with a human patient. Similar to the systems presented in [35], [40], [47], the experimental system was integrated into a patient exam table. The equipment was secured beneath the table. A single circular hole was made in the table, the radome was placed inside this hole and provided the interface between the patient and the system. For each breast scan, a volume of ultrasound gel (based on the participant's breast size) was first placed in the radome, then the patient lay in the prone position on the table and placed the breast to be scanned in the radome. The table was designed for patient comfort; the table was padded and there was an adjustable headrest with a pillow provided. There was a covering along the sides of the table so that the electrical equipment was not visible to the patient. The patient interface was easily sanitized between patient scans; the table covering sheet and pillow cover were changed between each use, and the ultrasound gel

was replaced. A photograph of this initial clinical system is shown in Fig. 3.10, with an example of a patient volunteer undergoing a breast exam.

Figure 3.10. (Left) Photograph of the patient exam table without the side covering, headrest, or table sheets, to show the location of the equipment. (Right) Photograph of a patient volunteer undergoing a breast exam [74], [75].

Two pilot clinical trials were conducted with this patient exam table. The goals of the first trials were to assess the repeatability and usability of the patient exam table. In the first study, 13 patient volunteers were recruited with the aim of having monthly breast scans. As this was a preliminary trial, it was essential that the volunteers fit a specific recruitment profile A summary of the patient recruitment profile is presented in Table 3.3. The 13 volunteer recruited for participation in this trial were between 21 and 76 years of age, with cup sizes A - D. Each patient visited between two and six times over the course of eight months. Visits were scheduled in monthly increments; however, due to scheduling issues, not every patient was scanned each month. A summary of the patient information is presented in Table 3.4.

For the second trial, scans were done with a single healthy patient volunteer (age 44, cup size C). This trial involved daily scans over the entire menstrual cycle. The aim of

this second study was to demonstrate the repeatability of daily measurements with the clinical system and to track the healthy changes that can be observed at different stages of the menstrual cycle; tracking these healthy changes helps to create a profile of what the natural variation in microwave measurements may be.

TABLE 3.3. INCLUSION CRITERIA AND THEIR RATIONALE FOR SELECTION OF VOLUNTEERS FOR INITIAL CLINICAL TRIALS (ADAPTED FROM [87]).

Inclusion criteria	Rationale
Female	Good fit with system
Cup size A to D	
Aged 18 +	Legal age
No history of breast cancer	Interested in healthy tissues only
No mastectomy	Lacking natural tissues to scan
No breast implants	Safety not yet examined under these conditions
No piercings	
No pacemaker	

TABLE 3.4. PATIENT INFORMATION: AGE, BRA CUP SIZE, NUMBER OF VISITS, AND DURATION OF PARTICIPATION IN THE CLINICAL TRIAL.

Patient #	Age	Cup Size	# Visits	# Months
1	21	C	4	6
2	25	D	4	6
3	24	C	5	7
4	44	C	6	8
5	54	B	4	8
6	55	B	2	2
7	23	B	6	6
8	44	C	6	5
9	38	B	4	5
10	26	A	5	6
11	22	B	4	6
12	27	C	3	3
13	76	B	4	4

The initial testing of the table-based prototype with healthy volunteers provided feedback on patient comfort and the reliability and repeatability of the system [71] - [75],

[87]. However, some issues were identified: the use of delicate end-fire antennas required a sturdy hemispherical radome, and as a consequence, an immersion medium was necessary to mitigate any air gaps between the breast and the radome. The use of an immersion medium adds complications in that the precise breast location is unknown, the thickness and distribution of the immersion medium cannot be predicted, and thus the accuracy of imaging algorithms, which often rely on dielectric property estimates along transmit-receive paths, suffers. Additionally, there is no robust method to guarantee a repeatable orientation of the breast within the radome from scan to scan. For these reasons, the idea of a wearable prototype, using flexible antennas, was proposed. With flexible antennas, the array can be conformed to the breast removing the need for an immersion medium and all of the associated uncertainties.

Thus, after these first two clinical studies, flexible antennas were proposed. The implemented antennas are broadband monopole antennas that are printed onto a flexible dielectric substrate [88]. This allows for the easy, quick, and cost-efficient production of antennas. The antennas have been specifically designed for biomedical applications and are intended to be in direct contact with the skin [75], eliminating the need for an immersion medium. In [76], a wearable prototype is fabricated using a 16-element antenna array, of the above mentioned monopole antennas, embedded in a bra. The antennas are placed on the inside shell of the bra, ensuring that they are in direct contact with the skin when the bra is worn. The antenna connectors protrude out of the bra, where they are connected to cables that are connected to the switching matrix. This is the only change from the table-based clinical prototype; the wearable bra-based array has replaced the radome and the antenna array. Currently, only one cup of the bra has an integrated array, and as such all breast scans were performed only on the right breast. However, a final system design must accommodate both breasts. In Fig. 3.11, a photograph of the connectorized flexible monopole antenna (left) and of the wearable prototype worn by the

volunteer (right) is shown. The photograph of the patient demonstrates that at all of the antenna locations the bra is slightly pushing into the skin, ensuring that there is good contact between the antennas and the skin.

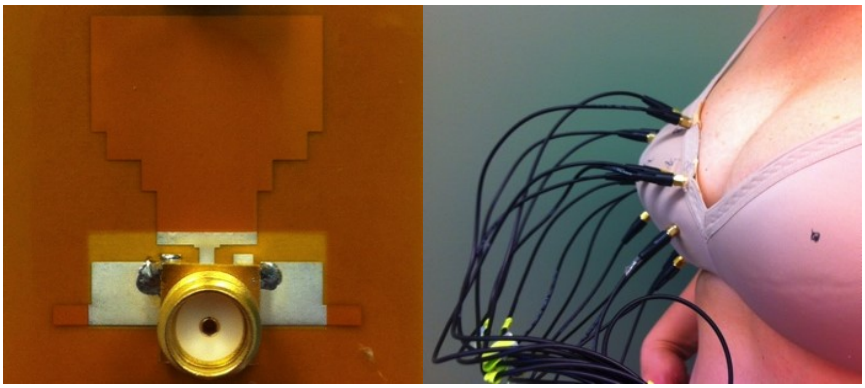

Figure 3.11. (Left) Close-up photograph of the connectorized monopole antenna, measuring 20×20 mm^2 (Right) The wearable prototype fitted to a volunteer with all antenna connections [76].

To examine the improvement in the measurements attributed to the use of flexible antennas, the second clinical study was repeated with the wearable prototype. Specifically, in [76], a comparison of the performance of the table-based and wearable prototype is presented. The results presented focus on scans of a single volunteer who participated in both studies. The volunteer is a healthy 45-year old woman with a cup size of C, ensuring a good fit with both the radome of the table-based prototype and the wearable bra-based prototype.

With both systems, daily scans were conducted over a 28-day period. The collected data is used to generate a set of 3-D images, following the process outlined in Chapter 3.3, for each day's measurements. The objective of these daily measurements is to categorize the reliability of the system to produce repeatable results and to identify the variation in healthy changes. In addition to daily scans with a patient volunteer, daily scans were performed with hemispherical breast phantoms with both prototypes. These scans with the phantoms served as a control case; the only differences in the phantom

data set are due to the equipment and minor differences in the positioning of the phantom from day-to-day. Further, unlike the breast tissues, these phantoms have dielectric properties that change minimally over a period of one month.

In order to contrast the performance of the two prototypes the Structural Similarity Index, SSIM, [89] is used. The SSIM metric considers three image characteristics: the luminance, the contrast, and the structure. When comparing two images, an SSIM value of one represents two identical images, an SSIM value of zero indicates the two images have no similarity. As SSIM operates based on 2-D images, and the images generated are a 3-D image, the reported SSIM values are calculated by first finding the SSIM for each 2-D slice, and then averaging over all the slices that make up the 3-D image. In Fig. 3.12, the SSIM value is shown for each day of measurements, in which the image from Day X $\{X = 2{:}28\}$ is compared to the image from Day 1. The data shown in orange (diamonds) corresponds to the volunteer data collected with the wearable prototype while the data with volunteer recorded with the table-based prototype is shown in blue (circles). The phantom data both prototypes (green '+' for the table-based prototype, and purple 'x' for the wearable prototype) is shown as the control group.

Table 3.5 summarizes the SSIM value statistics for the wearable prototype and the table-based prototype. From Fig. 3.12 and Table 3.5, it is evident that the images generated for the patient volunteer with the wearable system are more similar, indicating lower variability in the recorded data. The images obtained from volunteer scans with the wearable system lead to a mean SSIM of 0.925 over the 28-day period, whereas the same volunteer scans with the table-based prototype had a mean of 0.869.

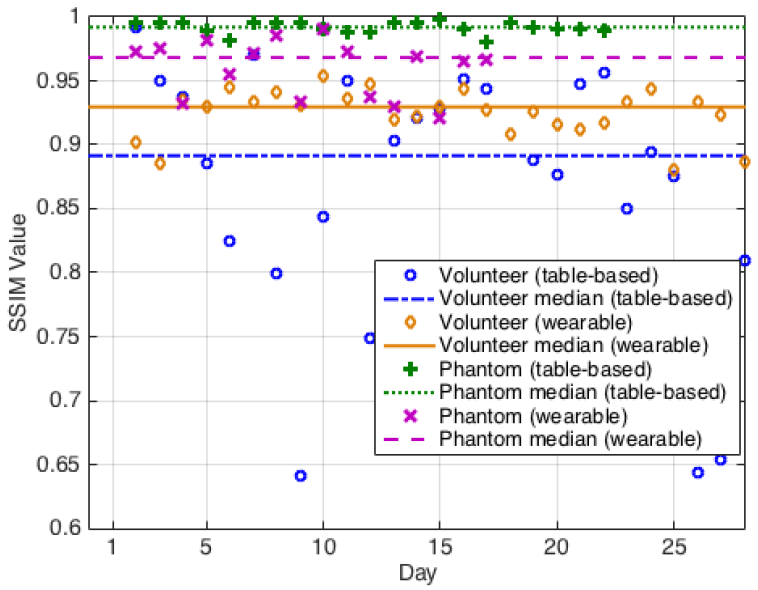

Figure 3.12. SSIM values for images from all days compared to the image from Day 1: with the table-based prototype with ceramic dielectric radome, volunteer data (blue, circles) and phantom data (green, crosses); with the wearable prototype, volunteer data (orange, diamonds) and phantom data (purple, x's). Volunteer data is from the right breast (same volunteer for all measurements) [89].

This improvement can be attributed to the fact that with the wearable prototype, the breast position is more fixed and known, due to the lack of immersion medium and the use of an antenna array in direct contact with the skin. The standard deviation and range of SSIM values are also lower for the wearable prototype than with the table-based prototype. This result confirms that the wearable prototype works at least as well as the table-based prototype for this volunteer.

In general, phantom measurements with both prototypes have higher SSIM than volunteer measurements. This is attributed to two factors: i) the phantom used was stable in dielectric properties over the measurement period, and ii) repositioning of the phantom is easier to control than repositioning of a person. The phantom measurements with the table-based prototype have a mean SSIM of 0.992, while the wearable prototype phantom measurements have a mean of 0.960. The higher SSIM with the table-based prototype is due to the fact that the phantom shape (rigid hemisphere) is designed to fit the table-based radome, and as a result the wearable prototype does not conform as well to the

phantom as it does to the breast. As the wearable prototype reduces the error associated with breast positioning, the residual differences in SSIM over the days are suggestive of breast tissue changes in accordance with the menstrual cycle.

A complete analysis of the patient volunteer data, for both clinical trials, with both system prototypes can be found in [75], [76], [87].

TABLE 3.5. SSIM STATISTICS FOR DATA FROM TABLE-BASED AND WEARABLE PROTOTYPES (WITH PHANTOM AND VOLUNTEER) [76].

	Table-Based		Wearable	
	Phantom	*Volunteer*	*Phantom*	*Volunteer*
Mean	0.992	0.869	0.960	0.925
Standard Deviation	0.005	0.101	0.022	0.019
Range	0.018	0.350	0.071	0.073

3.5 Signal Processing for Improved Detection

In this section, different signal processing methods to improve the detection capabilities of the system are presented. These methods are further divided into two groups: calibration techniques for data pre-processing and the implementation of classification algorithms for decision making. The calibration technique section focuses on methods to improve the quality of the tumour response extracted from the recorded data. This includes pre-processing steps such as time-alignment and normalization and the application of hybrid artifact removal strategies to remove the early-time response. Then, an investigation into implementing machine learning algorithms for data analysis is presented. The aim of using machine learning algorithms is to make a decision on whether the measured data is from a healthy or cancerous scan; this decision making process would eliminate the need for human interpretation of an image.

3.5.1 Calibration Techniques

This section is aimed at identifying pre-processing methods to improve the quality of the tumour response signal that is extracted from the measured data. In [77], a method was proposed to modify the data pre-processing prior to image generation. This method was focused on using a healthy baseline scan that did not come from the same source as the tumour-bearing scan. This scenario aims to represent the cases when there are significant changes to the breast tissue composition, besides the development of the tumour, between the regularly scheduled breast scans (such as changes in breast density associated with the menstrual cycle).

A set of reference signals were recorded, using the experimental system in 3.1, from three different materials by completely filling the radome with either safflower oil, $\varepsilon_r = 3$, fat-mimicking tissue, $\varepsilon_r = 10$, or ultrasound gel, $\varepsilon_r = 68$. These data sets are used for the healthy baseline signals, and represent a range of different breast densities (safflower oil – very low, fat-mimicking phantom – normal, ultrasound gel – very dense). Data was then recorded from the realistically shaped breast phantom made up of 100% adipose tissue, with a 2-mm thick skin layer, with a 1-cm radius spherical tumour embedded in the left half. The fat-mimicking tissue is the most similar, in terms of dielectric properties, to the phantom under test. The utrasound gel and safflower oil represent significant differences in the dielectric properties from healthy breast tissues.

One of the major issues of the previously defined method (section 3.3) for obtaining the tumour response signal is the direct pulse residual. The direct pulse, also referred to as the early-time response, is a group term referring to the early part of the recorded signal. This signal contains the pulse travelling directly between antennas and the initial reflections that occur at the first interfaces that the pulse encounters (radome wall – immersion medium, immersion medium – skin, and skin – fat interfaces).

In [77], a simple normalization method is proposed to address the issue of the direct pulse residual. The calibration problem can be visualized in Fig. 3.13; the top signal represents a signal from the tumour-bearing scan and the bottom signal is for the corresponding healthy baseline. To mitigate the time-shift, ΔT, that arises from the jitter effects from the various active components of the system, the alignment procedure defined in Section 3.3 is used. Then, a normalization procedure adjusts the amplitude of the direct pulse in the reference signal. Without this, the direct pulse residual would drown out the weaker tumour response, thereby making imaging impossible. A normalization factor, k, is found such that:

$$k = M_1/M_2 \tag{3.2},$$

where M_1 and M_2 are the maximum amplitudes of the direct pulse for the recorded and reference signals respectively, as shown in Fig. 3.13. The reference signal is then multiplied by this normalization factor. The final step of the calibration procedure is to subtract the time-aligned and normalized healthy baseline signal from the signal recorded from the tumour-bearing breast. This process is repeated for the 240 signals recorded to create the differential data set. An example of the resulting tumour response signal is shown in Fig. 3.14. This plot demonstrates that the direct pulse has been successfully removed from the tumour-bearing signal and the tumour response remains unaffected by the calibration. The signals plotted in Fig. 3.14 were obtained from nearest-neighbour antenna pairs when using the fat-mimicking tissue as the healthy baseline signal.

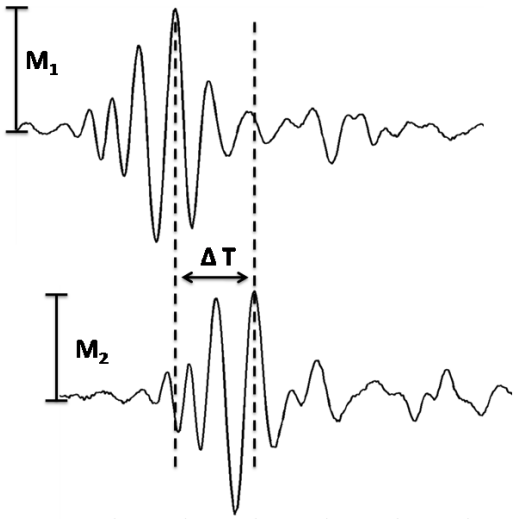

Figure 3.13. An example demonstrating the potential mismatch between the recorded signals for a tumour-bearing scan and the healthy baseline. Here ΔT represents the time-shift between the two signals that is compensated for by the time-alignment procedure. M_1 and M_2, respectively, represent the maximum signal amplitude for the recorded and reference signal [73].

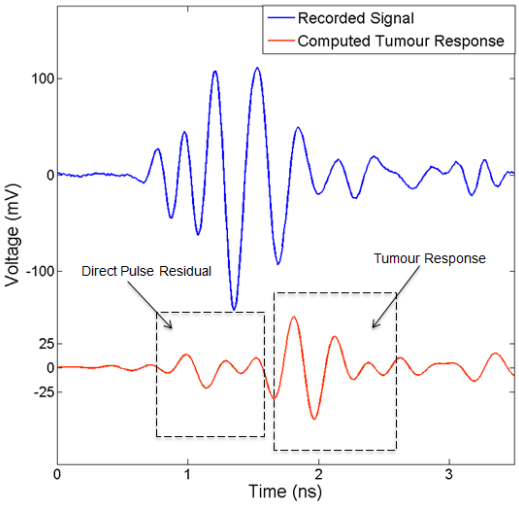

Figure 3.14. An example of the resulting tumour response signal after calibration. We highlight the direct pulse residual and the tumour response. This is an example of successful calibration as the direct pulse and the early-time response has been removed from the recorded signal while the tumour response is now revealed [73].

To assess the performance of this modification to the data pre-processing, images of the breast phantom are created when using the various healthy baseline signals (safflower

oil; fat-mimicking phantom; ultrasound gel; and the realistically-shaped breast phantom itself, without the embedded tumour, as the control). The reconstruction images are created using the DMAS imaging algorithm with the differential data set. In Fig. 3.15, a comparison of 2-D coronal slice images, at a depth where the global maximum intensity is located, are presented for three different calibration cases; first, using the previous method outlined in Section 3.3 with data from the same phantom without the embedded tumour used as the healthy baseline signal. The second and third images are generated using the new method that employs the normalization protocol to baseline signals that are recorded from materials different than the tumour bearing scan.

In addition to a visual inspection of the reconstructed images, the quality of the tumour detection can be assessed and compared with the SCR and tumour localisation error. These metrics are presented in Table 3.6.

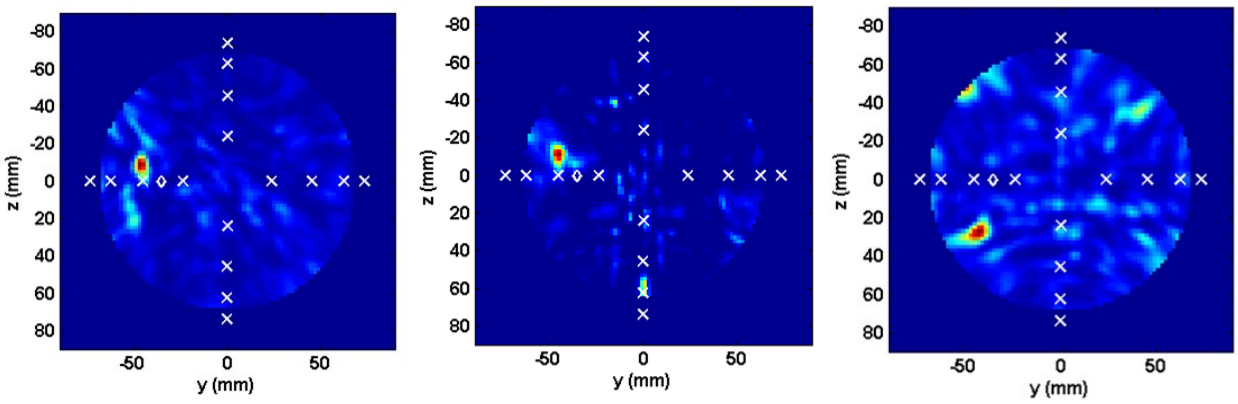

Figure 3.15. Comparing the reconstructed images of the breast phantoms from the various calibration methods; (left) using the same phantom (without the embedded tumour) as the baseline signal, (center) using the fat-mimicking material as the baseline signal, and (right) using the ultrasound gel to obtain the baseline signal. In the images the '×' markers denote antenna locations and the '◊' symbol denotes the physical location where the tumour is inserted into the phantom. Modified from [73].

TABLE 3.6. COMPARING TUMOUR DETECTION AND LOCALISATION FOR THE VARIOUS CALIBRATION TECHNIQUES

	SCR [dB]	Localisation Error [cm]
Differential Method	7.06	1.50
Fat-mimicking Tissue	4.59	1.49
Ultrasound Gel	3.99	2.82

From a comparison of the images of Fig. 3.15 (left and centre) and Table 3.6, it is possible to conclude that the addition of the normalization procedure allows for the tumour to be detected and localised, even when the healthy baseline scan is not performed on the exact same breast phantom as the tumour bearing scan, at a similar level to the ideal method proposed in Section 3.3. It is important to note however, that the normalization procedure fails with both the ultrasound gel and safflower oil data sets. This outlines the fact that small changes in the breast tissue composition, such as those between the realistic breast phantom the fat-mimicking tissue, can be mitigated with pre-processing techniques to ensure that the image reconstruction is successful in detecting the presence of the tumour. However, when the changes in tissue composition are more pronounced, such as the cases represented by the ultrasound gel and safflower oil scans, the ability to use signal processing methods to extract the tumour response signal becomes impossible as this signal is much lower than the other changes introduced. These results also agree with the results presented in [38], that suggests the data set used for calibration should be chosen based on the known density of the breast, as the density of the breast is highly correlated to the dielectric properties.

More recently, a hybrid artifact removal (HAR) algorithm has been suggested to minimize the early-time response and extract the tumour response signal from the measured data [90]. This process involves a two-stage approach: the early-time response window is estimated and, subsequently, a Wiener filter is applied within this window [90]. In [91], a modification of this algorithm was proposed in order to apply the HAR technique

to experimental data collected with realistic breast phantoms with the developed time-domain experimental system from Section 3.1.

As opposed to the previously outlined calibration methods, which relied on time-alignment to account for jitter in the system, the HAR algorithm does not have such requirements. This makes the HAR algorithm more robust to measurement uncertainty in repeated scans, such as antenna positioning and equipment drift, that can greatly impact the removal of the early-time response [63], [65]. An example of failure to remove the early-time response using the method outlined in Section 3.3, for a breast phantom test, is shown in Fig. 3.16. The artifact removed signal is defined as the signal after the calibration process, in this case it is clear that the tumour response signal has not been successfully extracted from the original measurement data. The estimated tumour window is defined based on the known location of the tumour within the phantom and the known permittivity of the breast phantom.

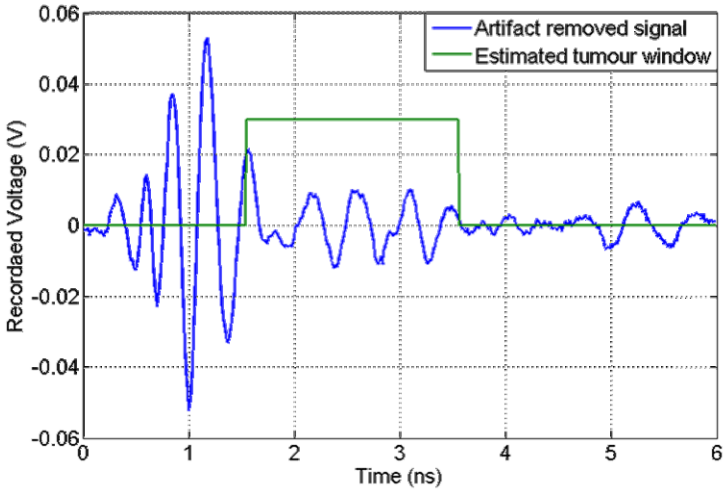

Figure 3.16. Example of failed removal of the early-time response, it is clear from this plot that even after calibration the artifact removed signal has more energy in the early-time response as opposed to the expected tumour window.

The HAR algorithm in [90] is implemented as follows: signals from a recorded data set are grouped such that they have the same early-time response, this is achieved by choosing antenna pairs with the same distance between them; then the early-time window is estimated using an entropy based analysis [90]; finally, a Wiener filter [85], which removes the common signal of each group, is applied over the entropy defined window to remove the early-time response. The application of the HAR algorithm to a time-domain experimental system, as was done in [91], represents the first time use of these type of algorithms for early-time response removal with a bistatic system; all previous analysis was done on monostatic systems. In this section, a modified HAR algorithm is applied to the data collected from realistic breast phantoms with the developed experimental system.

For this system, data is first grouped into two categories: reflection signals and transmission signals. The reflection signals are recorded from antennas on the same side of the radome. The transmission signals refer to the case when the antennas are not on the same side of the radome (this refers to those antennas separated by either 90° or 180°). Each group of signals can be further divided into different subgroups based on the exact antenna locations and the antenna pair being investigated (the antennas spaced 90° and 180° apart are in separate subgroups). Note, in all cases the cross-polarized signals have been removed from this analysis. As there are only four cross-polzarized antennas, there are not enough data paths for effective filtering. The result is that only 12 of the 16 antennas are used in this analysis. A figure of the radome and the grouped antennas is shown in Fig. 3.17. Antennas of the same colour represent the possible reflection groups, the transmission signals come from antennas on the same ‘ring’ of the array but of different colours. Furthermore, examples of the signals for both a subgroup of the reflection signals and of the transmission signals is shown in Fig. 3.18.

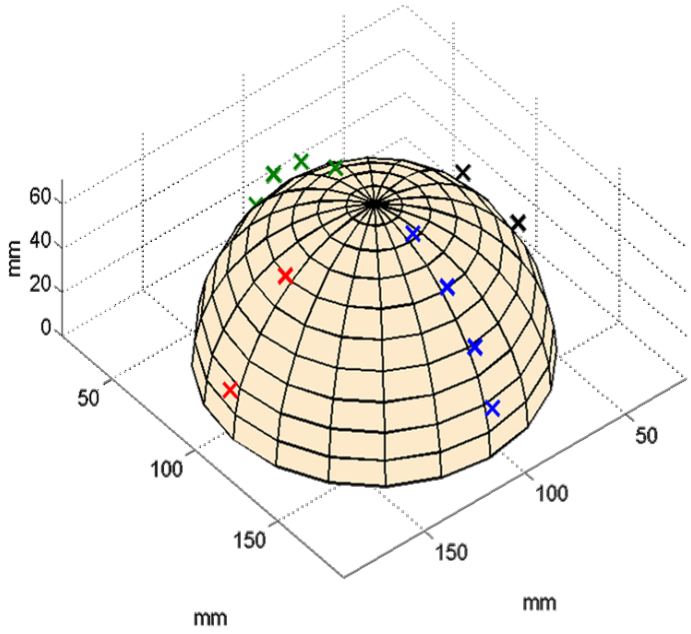

Figure 3.17. An example of the antennas being grouped into the reflection signals and the transmission signals. Antennas of the same colour correspond to the reflection signals; transmission signals come from antennas of different colours.

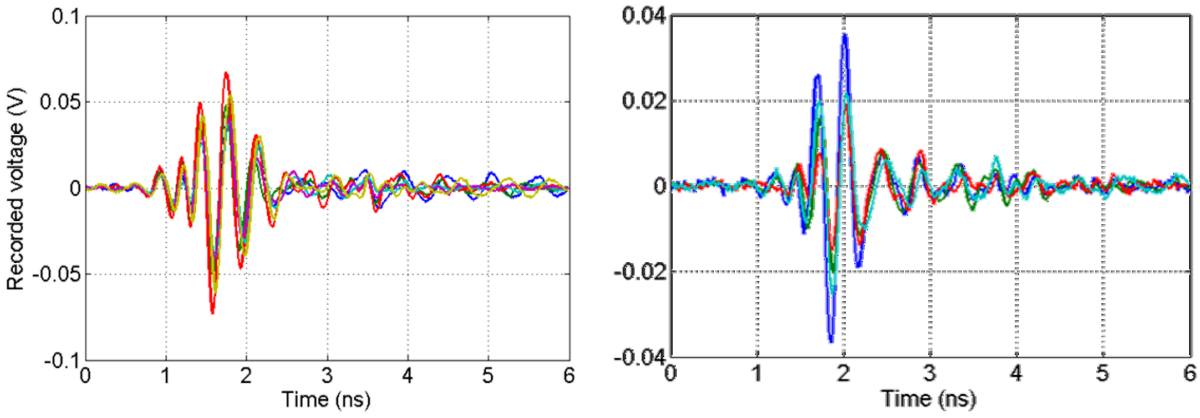

Figure 3.18. An example of (Left) grouped signals for one of the subgroups of reflection signals and (Right) for one of the subgroups of transmission signals.

In order to apply the Wiener filter, the early-time window must first be identified for each group of signals. The identification of this window is based on the summed entropy of the group of signals. Regions of high similarity in the grouped signals will have higher

entropy. These regions of high entropy represent the early-time response where the direct pulse between antennas and the skin reflection are the predominant contributors to the measured signal, which should be fairly similar across the channels in the group. The regions of lower entropy represent the irregular differences along that transmission path (such as the presence of glandular tissue or a tumour). The early-time window is then estimated when the entropy of the group falls below a certain threshold. For the experimental data with the system presented here, the following modification to entropy-based window estimate is proposed: define the early-time window based on the first local minima in the theoretical entropy signal that occurs after the maximum value in the transmitted signal. An example of the computed entropy, for a sample reflection and transmission signal group, and the corresponding estimated early-time window is shown in Fig. 3.19. The location of this window in the corresponding group of signals is also plotted.

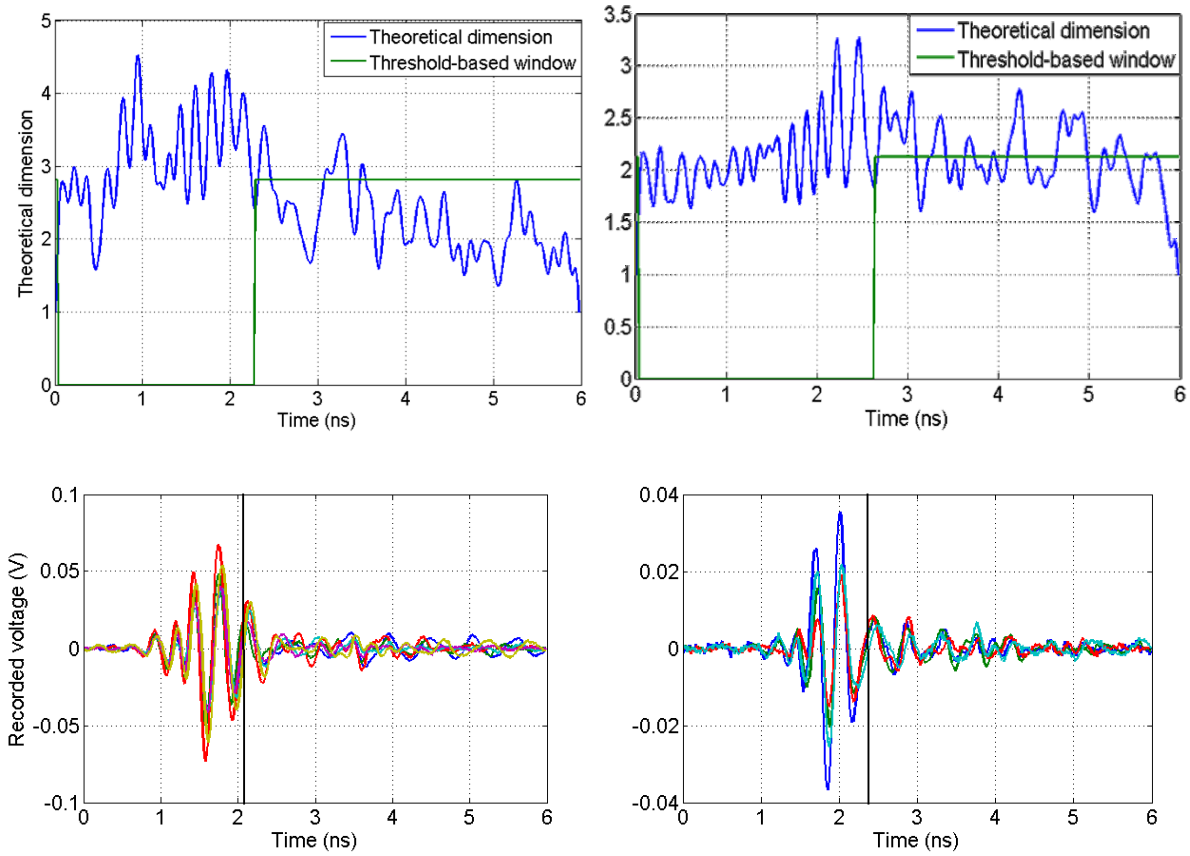

Figure 3.19. (Top left) The calculated entropy for the group of reflection signals. (Bottom left) The corresponding group of reflection signals, with the vertical black line marking the end of the early-time window. (Top right) The calculated entropy for the group of transmission signals. (Bottom right) The corresponding group of transmission signals, with the vertical black line marking the end of the early-time response.

The final step of the HAR algorithm is to apply the Wiener filter for each group of signals over the early-time window. The goal of the application of the HAR algorithm with this experimental system is to help remove the direct pulse residual and help extract the tumour response signal while in the context of a monitoring application. Therefore, the HAR algorithm is applied to both the healthy baseline and the tumour-bearing phantom measurements. The tumour response signals are computed by subtracting the artifact removed healthy baseline signals from the artifact removed tumour-bearing

signals. A comparison of the final tumour response signal for the HAR algorithm as defined in [90] and the modified HAR algorithm as in [91], with the estimated tumour window, is shown in Fig. 3.20. It is clear from this plot that the modified HAR algorithm proposed greatly reduces the signal that is outside the estimated tumour window and preserves the response from the tumour itself.

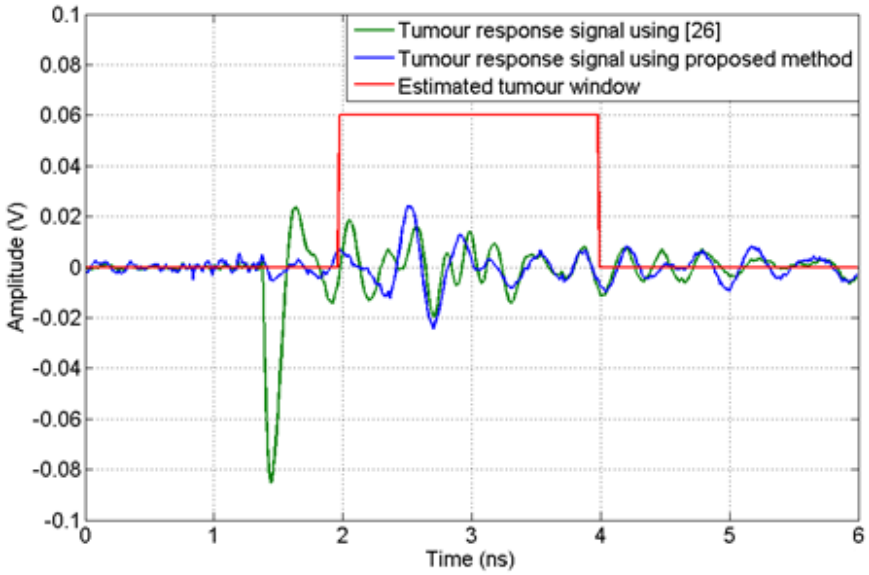

Figure 3.20. A comparison of the artifact removed signals using the method proposed in [90] and in [91]. The artifact removed signal corresponds to the tumour response signal. The estimated tumour window is also shown to indicated where the expected tumour response signal should be located.

3.5.2 Initial Investigation for Machine Learning Algorithms for Classification

The primary focus of the various systems and data analysis presented in this thesis so far has been on the generation of reconstructed images of the breast in order to detect the presence of a tumour. In this section, machine learning algorithms are applied to the data collected with our developed experimental system to make a decision on whether the data comes from a healthy breast scan or a tumour-bearing scan. This analysis was carried out in [78], and represents the first experimental demonstration of applying machine

learning algorithms to classify scans of breast phantoms with a microwave breast screening system. The benefit of using machine learning algorithms is that it provides a binary response on the presence of an abnormality; there is no need for a human user to interpret an image. Additionally, machine learning algorithms offer an easier problem to solve relative to reconstruction algorithms, reducing the computational complexity of the data analysis. The drawback of using machine learning for classification is that it does not provide any information of the size, shape, or location of the tumour, and it requires a training data set prior to being tested.

Machine learning algorithms for classification purposes have been successfully implemented in related medical fields. In [92], mammogram images were analyzed to classify the breast tissue density in accordance with the BIRADS system using a k-Nearest Neighbors (kNN) classifier after feature extraction. In [93], the data obtained from electrical impedance measurements (400 kHz up to 1 MHz) of breast tissue samples was classified between non-carcinoma and carcinoma samples using Principal Component Analysis (PCA) to extract selected features and Linear Discriminant Analysis (LDA) to classify the tissue samples.

Recent literature has demonstrated that classification techniques can be extended to various microwave system applications; from those aiming to detect breast cancer [32], [33], [94] – [97], to stroke detection [55], and to bladder monitoring [58]. These works have focused primarily on the numerical analysis of applying Support Vector Machines (SVM) to a microwave system for breast cancer detection [33], [95] – [97].

In [78], machine learning classification techniques were applied to experimental data obtained from breast phantoms with a time-domain microwave system. In particular, the accuracy of the Linear Discriminant Analysis (LDA) and SVM classifiers in detecting the presence of a tumour embedded in two possible locations within the breast phantom was

investigated as these were the primary classification methods implemented in the literature, [96], [97].

In this study, a total of 230 breast scans from 15 different breast phantoms were performed over a period of eight weeks. Of the 230 scans, 200 from 10 different breast phantoms were used to train the classification algorithms. The breast phantoms used in this study are composed of adipose-mimicking tissue that fills the radome entirely. The differences in the ten breast phantoms are in the oil:water ratio used in fabrication; this ratio is varied so that the permittivity of the ten fabricated phantoms falls within the range of Fig 3.6. Two tumour locations are tested, one centred at a depth of about 2 cm positioned on one side of the phantom ("Position A"), and the other centred at a depth of about 3 cm on the other side of the phantom ("Position B"). An illustration depicting the two possible tumour locations within the breast phantom is shown in Fig. 3.21, the tumours are both spherical in shape, with a radius of 1 cm.

Scans were performed daily for each phantom over a week-long period to collect the training and test data. The training data set consisted of an equal number (100 scans) of healthy and tumorous breast scans. Additionally, the tumorous breast scans were equally divided (50 scans) into recordings from both tumor positions. The 30 test data sets were obtained from a completely different set of five newly fabricated phantoms, with an equal number of recordings, 10 scans each, from healthy phantoms, tumour Position A, and tumour Position B.

This process of data collection was chosen to emulate the clinical application of our system. The data required to train the classification algorithms is first obtained from a specific set of breast phantoms. Testing data is then obtained from newly fabricated phantoms; thus, the procedure of first training the classifier with a known entity and then testing the trained classifier with an unknown data set (new patient) is simulated. This

procedure ensures that there is no overlap in the data source distribution, testing the robustness of the system.

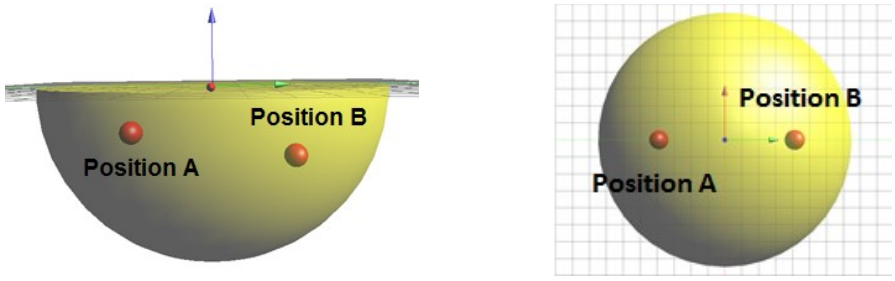

Figure 3.21. An illustration showing the breast phantom (yellow), and the two possible tumor locations, denoted by the red spherical tumors. A side (left) and top (right) view is shown, [78].

The proposed classification method requires several steps including: data pre-processing, feature extraction, training of the classifiers, and finally testing the classification performance with the test data set. This procedure is explained in detail below, and can be summarised by the flow chart in Fig. 3.22.

The first step is the data pre-processing. Signals recorded by the same antenna pairs (i.e., all the signals recorded with Antenna X as transmitter and Antenna Y as receiver, for all possible antenna pairs) were grouped for all of the breast scans. This process creates 240 separate data matrices to represent the recorded data for each antenna pair; allowing for the investigation of the effects of including or removing specific antenna pairs on the accuracy of the classification algorithms. The grouped data was then windowed, based on the longest possible path for a wave to travel within the radome, to only include the 400 samples (first 5 ns) immediately after the start of the direct pulse. Thus, the entire training data set (200 breast scans) is represented by 240 matrices with dimension of 200 $\times$ 400. Each of these matrices is referred to hereafter as $\widetilde{\boldsymbol{X}}_i$, where $i = 1, ..., 240$.

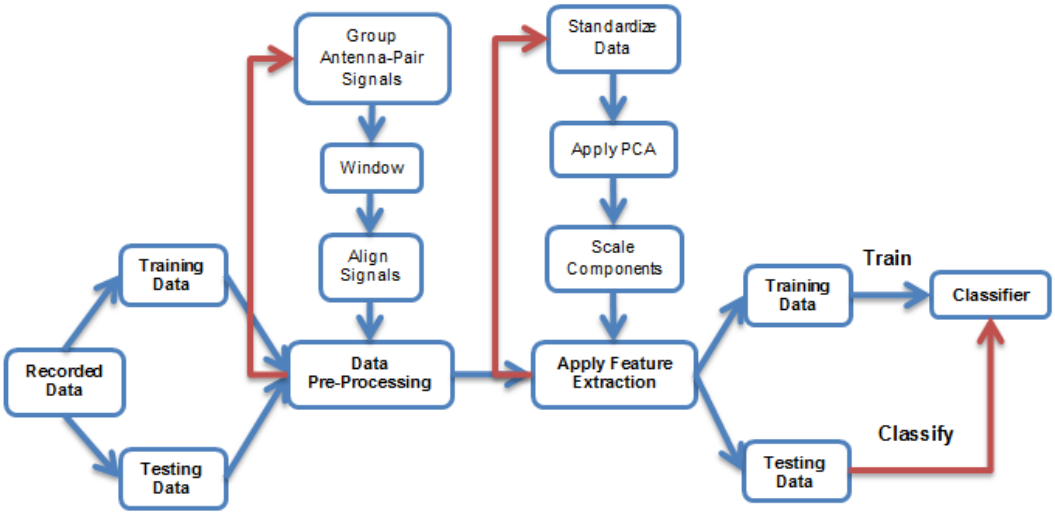

Figure 3.22. A flow-chart showing the steps followed to implement the detection algorithm [78].

The second step of the pre-processing algorithm was to mitigate sources of measurement uncertainties. This was accomplished by applying the time-alignment techniques discussed in Section 3.3 [65].

In Fig. 3.23 the result of data pre-processing is shown. A plot of all the collected signals, from both the healthy and tumourous phantoms, for a specific antenna pair is shown before and after the data pre-processing. From this comparison it is clear that the phase difference and the horizontal noise between recordings has been greatly reduced. The remaining variation between the signals is due to the differences between phantoms, the inclusion of the tumour, and the difference in the tumour locations.

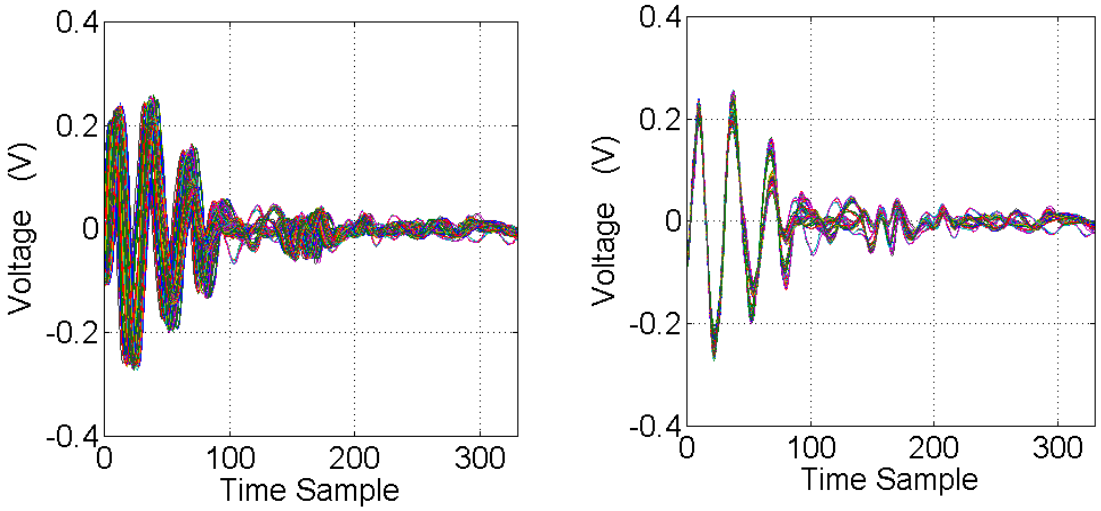

Figure 3.23. All received signals before (left) and after (right) data has been pre-processed, for one specific antenna pair [78].

After the data pre-processing, a feature extraction method was applied to the data to reduce the dimensionality of the data. Feature extraction minimizes the processing of the input data by extracting only the essential components, and using these components for analysis with the classifier. In [98], it was shown that PCA was the best feature extraction method on average; additionally, when combined with the SVM classifier, it yielded the best results compared to the combination of other classifier and feature extraction methods.

Prior to feature extraction the data set was first standardized on a signal-to-signal basis; the mean of the standardized data set is 0 and the standard deviation is 1. The standardized data set can be defined as:

$$\boldsymbol{X}_i{}^m = \frac{\widetilde{\boldsymbol{X}}_i{}^m - \mu_i{}^m}{\sigma_i{}^m}, m = 1,\ldots,200, \quad (3.3),$$

where X_i and $\widetilde{\boldsymbol{X}}_i$ are the standardized data set and the original data set, respectively, for a specific antenna pair i, where $i=1,\ldots,240$, m is a specific row of the matrices, and $\mu_i{}^m$ and $\sigma_i{}^m$ are the mean and the standard deviation, respectively, of a specific row m of matrix $\widetilde{\boldsymbol{X}}_i$. Thus, resulting standardized data sets X_i are the same size as $\widetilde{\boldsymbol{X}}_i$.

PCA was applied to the standardized data set, X_i, in order to extract the most important features. The extracted data feature set was stored in x_i, with i defined as above. The use of PCA reduces the dimensionality of the data by performing an orthogonal linear transformation to express the data in a new vector space such that each component that makes up this new coordinate system represents a diminishing amount of variance of the data (the projection of the data onto the first principal component represents the most variance), thus not all principal components need to be kept. This procedure diminishes the influence of the inherent noise of the experimental system. At this point only the first 50 components are saved. The training data is now represented by 240 matrices, x_i, with dimension of 200×50. The optimal number of components to use is computed during the cross-validation phase of the implemented protocol.

After the principal components have been extracted, the classification algorithm was applied to the data. Previous applications of classification algorithms for breast cancer detection with a microwave system have demonstrated that the SVM method outperforms other classification methods [96], [97]. While these studies were focused on data obtained numerically, the analysis presented here aims to confirm that these findings are relevant for an experimental system by applying the SVM classifier to our data and contrasting its performance with the LDA classifier. The classifiers were trained with the x_i matrices found from feature extraction, such that classification is performed for each transmit-receive antenna pair independently (total 240 pairs).

A procedure to optimize classifier performance was proposed in [99], and was used to optimize our implemented classifier. This procedure can be summarized as follows:

(i) Choose the appropriate SVM kernel function.

(ii) Scale the training data to ensure that it is in the [-1, +1] range. Apply the same scaling factor to the test data set.

(iii) Use cross-validation to find the optimal number of principal components, n, and the ideal SVM parameters (C, the box constraint, and γ, kernel scaling factor).

(iv) Train the SVM classifier with the optimal settings solved for using cross-validation.

As suggested in [99], a Radial Basis Function (RBF) kernel is implemented. The training data set is then scaled to the [-1, +1] range; this process ensures that training data in higher numeric ranges do not dominate the classifier [99]. A linear scaling was applied to each principal component to determine the necessary scaling factor; this factor is then applied to the test data.

A 10-fold cross-validation was performed to search for n, and (C, γ). In 10-fold cross-validation the training data set was equally divided into 10 randomly chosen subsets. Each subset was then sequentially tested with a classifier trained with the 9 remaining data subsets; thus, each subset of the training data was tested exactly once. The cross-validation accuracy is the mean of the correctly classified data across the 10 tests.

As suggested in [99], a coarse-then-fine grid search was used to determine the optimal (C, γ) values. The results for the coarse- and fine-grid search are shown in Figures 3.24(a) and 3.24(b), respectively, as contour plots. The colour intensity of the contour maps represents the mean classifier accuracy from the 10-fold cross-validation. The fine-grid search was conducted in the region within the most accurate region of the coarse grid search.

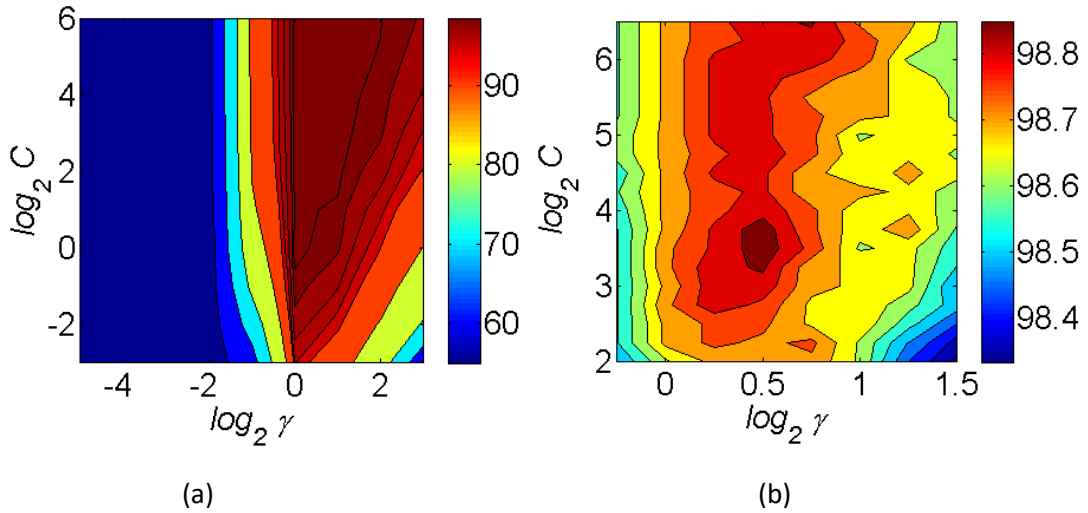

Figure 3.24. Results of grid search to find the optimal C and γ. A coarse grid search, (a), and a fine grid search, (b), are shown. The colour intensity represents the mean classifier accuracy for 10-fold cross-validation [78].

A simple linear search, ranging from 1 to 50, was used to determine the number, n, of principal components to use for the SVM classifier; additionally, a similar search was used to find the optimal value of n for the LDA classifier. In both cases, a 10-fold cross-validation was used to find n. In Figure 3.25, a plot comparing the mean cross-validation accuracy for the LDA and SVM classifiers as the number of principal components is varied is shown. The optimal number of principal components, based on the maximum cross-validation accuracy, is $n=31$ and $n=42$ for the SVM and LDA classifiers, respectively. It is clear that the SVM classifier is more computationally expensive than the LDA classifier; however, it also outperforms the LDA classifier.

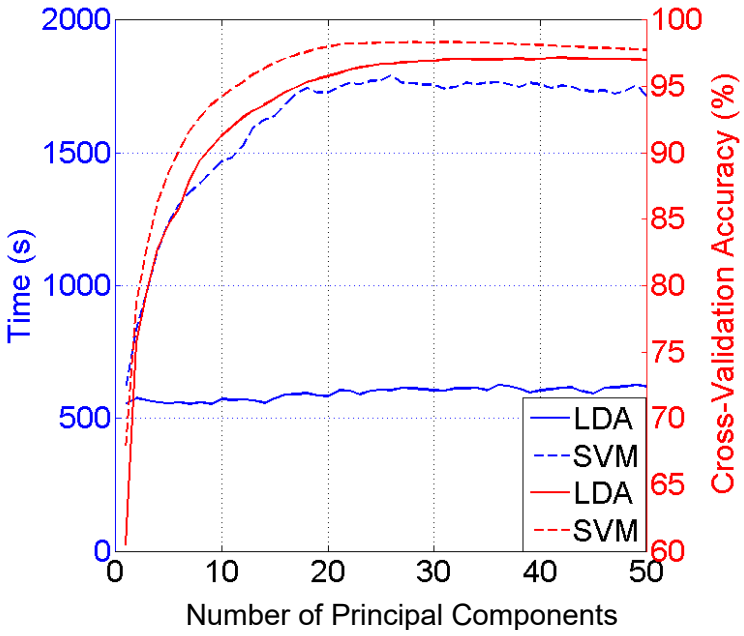

Figure 3.25. Comparison of computational cost (blue, left-hand axis) and accuracy (red, right-hand axis) versus the number of principal components for SVM (dashed) and LDA (solid), [78].

The final classifier was trained with the optimal values of (n, C, and γ) found from the optimization procedure. The trained classifier was tested with signals collected from newly fabricated phantoms, thus ensuring that there is minimal correlation between the training and testing data sets; the test data set is made up of signals recorded from 30 new breast scans.

The performance of the optimized SVM and LDA classifiers are compared in Table 3.7. The overall detection performance as well as the percentage of correctly classified signals for each of the three phantom types (healthy, tumour position A, tumour position B) is shown. This analysis confirmed that SVM algorithm improved the detection accuracy (defined as the percentage of correctly classified signals) of the system when compared with the LDA method; however, the difference is not as pronounced as was seen in [97]. Additionally, the prediction accuracy of the LDA classifier, here, outperforms the one presented in [97], perhaps suggesting that the LDA classifier, and not just the SVM classifier, is also suited for experimental analysis. The overall detection accuracy for the

LDA and SVM classifiers, respectively, is 70.30% and 73.64%. It is interesting to note that the while the LDA classifier slightly outperforms the SVM classifier in correctly identifying signals from healthy breast phantoms, with a detection accuracy of 70.00% for the LDA classifier compared to 67.48% for the SVM classifier, the SVM classifier is much more successful at identifying tumours, correctly identifying signals from the tumorous phantoms with an accuracy of 76.71% as opposed to only 70.45% for LDA. Additionally, regardless of the choice of classifier, the system is more adept at classifying signals recorded with the tumour embedded in Position B (an increase of over 15% and 12% for the LDA and SVM classifiers, respectively) than in Position A.

TABLE 3.7. DETECTION ACCURACY OF EACH CLASSIFICATION ALGORITHM [78].

	Healthy	Tumour		Overall
		Position A	Position B	
LDA (%)	70.00	70.45		70.30
		62.90	78.00	
SVM (%)	67.48	76.71		73.64
		70.48	82.95	

For the results described above, the LDA and SVM classifiers were applied on a signal-to-signal basis; each of the 240 signals making up a test data set was classified as being a signal derived from a healthy or tumourous phantom. Results from our previous work, [63], has suggested that there is high signal-to-noise ratio (SNR) from transmit-receive antenna pairs that are located on the same side of the radome; suggesting that these clusters of antennas can be used for more reliable detection. The four antennas of each quadrant of the radome make up an antenna cluster, for a total of four antenna clusters.

In Table 3.8, the detection accuracy for both the LDA and SVM classifiers, for each phantom type, when using only signals from the four antenna clusters is shown. Using these selected signals significantly improves the tumour detection accuracy, from 70.48%

to 83.50% for a tumour in Position A, and from 82.95% to 91.75% for a tumour in Position B, for the SVM classifier. For LDA, an improvement from 62.90% to 71.04% and from 78.00% to 83.75% are observed for Positions A and B, respectively. These values suggest that further investigation into the effect of antenna groupings on detection may be worthwhile to improve detection in scenarios with complex tissue composition.

TABLE 3.8. THE DETECTION ACCURACY FOR SVM AND LDA WHEN ONLY SIGNALS FROM THE FOUR ANTENNA CLUSTERS ARE USED [78].

	Healthy	Tumour	
		Position A	Position B
LDA (%)	54.79	77.40	
		71.04	83.75
SVM (%)	57.00	87.63	
		83.50	91.75

The results from Table 3.8 suggest the improved tumour detection is a direct trade-off for higher false-positive rates for both classifiers. In an attempt to improve the classification accuracy of the SVM classifier the design of a modified classification protocol, with the potential to control the false-positive rates, was then researched.

To this end, the developed protocol for applying the SVM and LDA classifiers was applied to the differential data set, as presented in [79]. In addition, the investigation of using a data-fusion technique was also investigated. Following the procedure outlined in Section 3.3, a differential data set for 10 breast phantoms is obtained. A total of 150 breast scans from 10 breast phantoms were used to obtain the training data set. Let X_m be the complete data set recorded from a specific breast phantom m, where $m = 1, \ldots, 10$. The k^{th} differential signal data set, ΔX_{mk}, can be defined as the difference between the initial breast scan X_{m1} and some future breast scan, X_{mj}, of the same phantom, such that:

$$\Delta \boldsymbol{X}_{mk} = \boldsymbol{X}_{mj} - \boldsymbol{X}_{m1} \qquad for\ j = 2, 3, \ldots, n\ and\ k = 1, 2, \ldots, n-1 \quad (3.3),$$

where n is the total number of breast scans performed on each specific phantom m. This process is repeated for each of the 10 breast phantoms; thus, 140 differential data sets are obtained, of 240 signals each, to train the classifier. The training data is evenly divided (70 data sets each) between healthy differential data sets and tumourous differential signals. Of the 70 data sets representing a tumourous differential, half are obtained from scans when a tumour is embedded in Position A and the other half from Position B. To ensure there is no overlap between the training and testing data, the test data set is obtained from two breast phantoms not included in the initial 10 breast phantoms used to train the classifier. The first scan of each new breast phantom is used as the reference (X_1), and each subsequent scan is used to obtain the differential data set, ΔX_k, for each phantom. The test data set is made up of 32 scans, equally distributed between scans when no tumour has developed (healthy) and when a tumour is embedded at one of the two positions; i.e. 16 scans where no tumour is inserted into the phantom, 8 cases where the tumour is inserted into the phantom at Position A, and 8 cases when the tumour is inserted into Position B.

An example of the three types of differential signals for a specific antenna pair is shown in Fig. 3.26. These differential signals represent the difference between two successive scans of a breast phantom when (i) there are no changes to the tissue, shown in blue, (ii) a tumour is embedded in the phantom at Position A, shown in red, and (iii) a tumour is embedded at Position B, shown in green. From Figure 3.26 it can be observed that, starting at about 50 samples, there is a region of interest (highlighted in the plot with the dashed box) where the three signal types vary significantly. Thus, prior to any further analysis, the data set is windowed to only retain information after the first 50 samples.

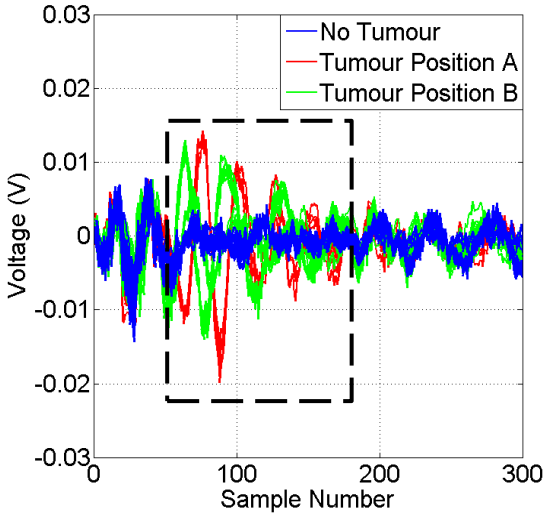

Figure 3.26. A comparison of the three types of differential signals obtained for a specific antenna pair. The region of interest where the three differential signals are most varied is highlighted [79].

The differential data set was pre-processed to mitigate the effects of random measurement noise and jitter and PCA was performed to extract the most important features from the data. The LDA and SVM classifiers were trained with the extracted features from the training data set. The SVM classifier was optimized, following procedure defined earlier in this section, to determine the optimal value of the number of principal components, n, and the SVM operating parameters (C and γ) from a 10-fold cross-validation. The LDA classifier can be implemented without any optimization. The trained classifiers were tested with the testing data set obtained from the two newly fabricated breast phantoms.

In Table 3.9, the results of applying the LDA classifier and the optimized-SVM classifier to the differential data set are shown. The correctly classified, the false-positive, and the false-negative rates are all compared. The classifier performance without using differential signals, as presented in Table 3.7, are shown in parenthesis. When using the differential signal analysis, the overall correctly classified percentage is decreased by 8.6% for the LDA classifier, while it is increased by 3.89% for the SVM classifier. Additionally,

the false-positive rate, when using the SVM classifier with the differential data set is greatly reduced to 8.33%.

TABLE 3.9. A COMPARISON OF THE CLASSIFICATION RESULTS FOR LDA AND SVM WITH AND WITHOUT [78] THE USE OF DIFFERENTIAL SIGNALS. RESULTS FROM TABLE 3.7 SHOWN IN PARENTHESIS.

	Correctly Classified (%)	False-Positive (%)	False-Negative (%)
LDA	61.70 (70.30)	66.39 (30.00)	10.27 (29.55)
SVM	77.53 (73.64)	8.33 (32.52)	37.41 (23.29)

The above implementation of the LDA and SVM classifiers has been done on a signal-to-signal basis. All the data recorded from each specific antenna pair, over all the breast scans performed, were grouped together. Feature extraction and classification was applied to this grouped data. Thus, for each breast scan PCA and then classification is performed 240 times. The resulting output of the classification step is then 240 'decisions'; for each antenna pair the classifier gives a decision of 'healthy' or 'tumour'.

A data fusion technique aims to take into account the recordings of these antenna pairs simultaneously; that is to say, data is grouped from different antenna pairs *prior* to feature extraction (data from each antenna pair within a group are concatenated). Thus, the information of the group of antennas as a whole is used. This process also drastically reduces the computational complexity of applying the different classifiers.

In [79], the 240 signals from each breast scan, which represent the 240 antenna pairs, were grouped into 20 equally sized groups. Each group contains data from 12 specific antenna pairs. Four of these groups, 48 antenna pairs, represent the four quadrants of the antenna array. This was chosen based on the results from Table 3.8, which suggested that using these clusters of antennas improved the detection capabilities of the classifier. The remaining 192 antenna pairs were randomly distributed into 16 groups of 12. These antenna pairs were included to help mitigate the increased false-positive rate that was

seen as the trade-off in Table 3.8. By implementing the data fusion technique prior to feature extraction, PCA and the subsequent classification (LDA or SVM) will only need to be applied 20 times per breast scan. In Fig. 3.27, flow charts for the initial classifier protocol and the newly defined data fusion technique are compared.

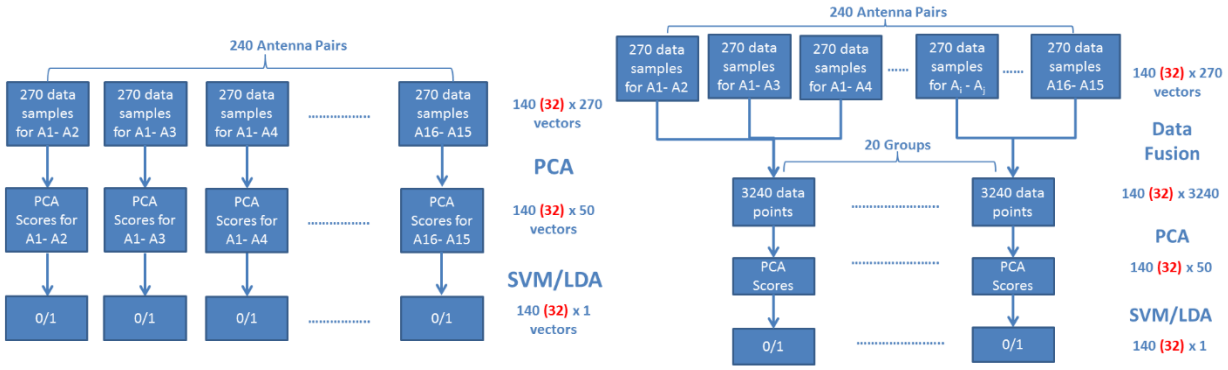

Figure 3.27. A contrast of the initial classifier protocol that is applied (Left) on a signal to signal basis and (Right) the newly developed data fusion technique. In this example, 270 data sample from each scan are stored for analysis.

The output of the classification algorithm is a numerical value, a 0 or 1 depending on the decision made, healthy or tumour respectively. The total number of decisions per breast scan is equal to the number of antenna pairs, or groups, used in the analysis. In [79], using information from all the antennas to decide on the type of scan (healthy or tumorous) is proposed. By averaging the result from each antenna pair, or group of antenna pairs (for data fusion), a single numerical value representing each specific breast scan can be calculated. This numerical value is hereafter referred to as NV. Depending on the NV value, a decision on whether the signals collected for that specific scan represent changes within the breast that are benign or malignant can be made.

It is therefore possible to choose a specific threshold value, t_h, such that if $NV > t_h$, the breast scan contains a tumour, and if $NV < t_h$, the scan represents a healthy breast phantom. In this analysis, a range of threshold values, such that adopting any threshold value within that range guarantees a 100% correct decision on the nature (healthy or

unhealthy) of the phantom being scanned, is presented. This provides an initial investigation into controlling either the false-positive or false-negative rate. Future work will focus on an automated process to choose the threshold value to minimize the false-positive rate without increasing the false-negative rate past a certain boundary.

To assess the benefit of the data fusion technique, a naïve form of grouping is used as a benchmark comparison. The data fusion technique groups data *prior* to feature extraction and classification, whereas the naïve grouping is performed *after* analysis. The naïve grouping analysis is performed by applying the same grouping as implemented in the data fusion technique, but a majority-vote on the output of the classifier is used to obtain a group decision. The comparison of the data fusion technique and the naïve grouping is shown in Table 3.10.

In comparison to the results presented in Table 3.9, using data fusion provides an increase in performance for both classifiers. The overall detection rate is greatly improved for both classifiers (an increase of about 28% and 14% for the LDA and SVM classifiers, respectively), and the difference in performance between the two classifiers is greatly reduced. Both the false-positive and false-negative rates for both classification algorithms are greatly decreased. Additionally, it is clear that using the data-fusion technique provides an increased improvement in comparison with a naïve grouping analysis. Clearly, the data fusion technique is very useful in improving the performance of the classification algorithms.

TABLE 3.10. CLASSIFICATION RESULTS FOR LDA AND SVM USING DATA FUSION TECHNIQUE FOR SPECIFICALLY GROUPING 12 ANTENNA PAIRS COMPARED WITH NAÏVE DATA GROUPING IN PARENTHESIS [79].

	Correctly Classified (%)	False-Positive (%)	False-Negative (%)	Threshold Value Range
LDA	89.58 (58.51)	15.28 (78.82)	5.56 (4.17)	[0.222, 0.944]
SVM	91.15 (80.73)	5.56 (2.43)	12.15 (36.11)	[0.056, 0.833]

3.6 Summary and Conclusions

In this chapter the design and development of a first-generation microwave system for breast health monitoring was presented. This system operates in the 2 – 4 GHz range and is used to record bistatic signals from a material under test. The system functionality was tested first with realistic breast phantoms that can accurately model the breast, both in terms of its shape and size and its dielectric properties. Images of these phantoms, with embedded tumours were created to demonstrate the system's functionality. The system was then tested with female patient volunteers in several early-stage clinical trials. These trials were used to demonstrate the reliability and repeatability of the measurement scans performed with this system. Furthermore, a novel wearable bra array was also developed and tested with the system.

This chapter also focused on the development of signal processing methods to improve the performance of the system to detect the growth of abnormalities. This involved the use of optimized calibration methods to remove the direct-pulse residual in the early-time response of the signals to improve the quality of the extracted tumour response signal.

Finally, machine learning algorithms were implemented to perform a non-bias decision making process on the type of scan (healthy or unhealthy) that the measurement data is recorded from. An optimized protocol for the SVM classifier, for this system, was presented, and the results from this SVM classifier was compared to the LDA classifier. The SVM classifier showed improved performance compared to the LDA classifier in all the tested cases. Furthermore, the idea of a data fusion technique that makes use of information from a group of signals was presented. The data fusion technique is used as part of the data pre-processing prior to the classifier implementation. This modification to the implemented classification algorithms lead to significant improvement in the overall

classification rates, and a significant reduction in the false-positive rates for both classifiers. To date, the testing of the machine learning algorithms has only been completed with a limited number of breast phantoms. While every effort was made to increase the complexity and variety in these breast phantoms, it is impossible to mimic the real-world scenario in which breast size, shape, and composition varies significantly. It is believed that as these techniques are extended to a clinical setting, an increased training data set would be required to maintain a high level of performance. Additionally, as there is a high variation in the measured response to different breast shapes, it is believed that for each breast size a separate classifier would be trained and used only for new data of that breast size.

The system was designed to work with a differential data set, as a monitoring application was envisaged. In the case when a decision must be made on an initial scan, it is possible to use the classification algorithm to compare the most recent scan of the patient to a database of healthy scans of women with a similar breast size. The classification algorithm can then be used to make a decision on whether the scan comes from a healthy patient or represents the development of an anomaly.

Chapter 4: Stable and Modular Breast Phantoms

This chapter is focused on the development of novel carbon-based breast phantoms that are both stable over time, and offer the potentially for highly modular fabrication. Complex breast phantoms, such as those presented in Section 3.2, are composed of various tissue-mimicking materials (TMMs). As the dielectric properties of human tissues are highly related to the water content of the tissues, many of the initial TMMs were fabricated based on different water solutions [67] – [69], [100], [101]. The primary drawbacks of using water-based TMMs are the difficulties in the fabrication procedure, often using hazardous chemicals and requiring the mixture of water, oil and gelatin, and issues related to storage that can cause dehydration and changes in the dielectric properties [67] – [69], [100]. Hence, there is a desire to develop new breast phantoms to address these concerns.

A key advantage motivating the development of stable breast phantoms is that they offer a consistent reference for an experimental system. This allows for the accurate assessment of any improvements to the system by isolating changes introduced due to hardware modifications from variations due to phantom composition or construction. This chapter presents the fabrication of stable carbon-based TMMs that eliminate the concerns with water-based TMMs and enable reliable system comparison. A method of creating TMMs that can cover the wide range of biological tissues of the human body is presented. A fabrication procedure for modular breast phantoms from various carbon-based TMMs is then presented. The carbon-based breast phantoms are then validated by measurements performed with the experimental prototype discussed in Chapter 3. Finally, high-resolution images, using MRI and X-ray, of rectangular phantoms fabricated from these TMMs are obtained and presented.

4.1 Development of Carbon-Based Tissue-Mimicking Materials

Tissue-mimicking materials are a vital element in safely testing, and validating, the development of novel biomedical devices and applications. To create an accurate, stable, and realistic breast phantom, it is necessary to ensure that TMMs can represent each of the various tissues that make up the breast structure. Thus, the development of novel TMMs must be able to represent the large range of dielectric properties exhibited by biological tissues. Additionally, TMMs that can be easily fabricated, without the need for handling hazardous materials or the use of specialized laboratory equipment, would be ideal.

Recently, researchers at the University of Calgary demonstrated that new carbon-based TMMs, created from a mixture of polyurethane, graphite, and carbon black, can be used to represent the tissues of the breast [102], ultimately using these TMMs to create realistic and stable breast phantoms [103]. These proposed carbon-based TMMs are stable over time; in [102], changes of less than 5% in the dielectric properties over an 8-month period were reported. Additionally, as these TMMs are made from a polyurethane rubber base, they are flexible and machinable, allowing for complex, stable, and reconfigurable breast phantoms to be fabricated.

The fabrication procedure for these carbon-based rubber TMMs is very simple: mix the appropriate amounts of polyurethane, carbon black, and graphite to re-create the desired tissue type; then let set overnight until solidified. By varying the amount of carbon black and graphite it is possible to control the complex permittivity of the material. This process was developed in [102] to create TMMs that can represent skin, bone, and fat. However, as high-permittivity TMMs require a large amount of carbon black and graphite, it was observed in [102] that this simple mixture procedure would fail (due to the rubber-carbon mixture becoming saturated, with the excess carbon remaining unmixed) when

trying to represent tissues such as glands or tumours. Due to this issue, results were not presented for tumour or glandular tissue in [102].

In [104], a modified procedure to the method proposed in [102] was suggested in order to fabricate TMMs that can represent high-water content tissues, such as tumour and gland tissues. This modification involved the use of small volumes of acetone, in the 3 – 8 mL range, to be used as a thinning agent to improve the mixability and increase the overall permittivity of the sample, creating materials that mimic high-water content tissues. A finalised list of the required materials for the fabrication of these TMMs is provided below:

1. Smooth-On PMC-120/30 wet Part A, polyurethane
2. Smooth-On PMC 120/30 wet Part B, polyurethane
3. Graphite powder, <20 µm, from Sigma Aldrich
4. Carbon black, acetylene, 50% compressed, Alfa-Aesar
5. Smooth-On Universal mould release
6. Acetone

A detailed generalised procedure for fabricating these carbon-based TMMs is as follows:

- Weigh equal parts of Smooth-On PMC-120/30 Part A and Part B
- Weigh graphite and carbon black for desired composition
- Apply mould release to final TMM container
- Thoroughly mix Part B prior to adding to Part A
- Gradually add graphite into the Part A/Part B mixture. Ensure that the mixture is homogeneous prior to adding more graphite.
- Gradually add the carbon black (after the graphite allows for easier mixing) to the current mixture. If making a high-permittivity sample, add in a small volume of acetone.

- Once homogeneous, pour mixture into desired mould. High-permittivity samples will become very viscous and will not be liquid at this stage.
- Let mixture cure for 16 hours at room temperature.

4.2 Dielectric Properties of Carbon-Based TMMs

In this section, the characterization of the dielectric properties of a variety of carbon-based TMMs is presented; additionally, an analysis on the effects of acetone, de-gassing, and time on the dielectric properties of these TMMs is also shown. By varying the relative concentrations of carbon black, graphite, and acetone, twenty different TMM-samples, spanning a wide range of complex permittivities, were fabricated and measured. These TMM-samples were fabricated, following the procedure outlined above in Section 4.1, to represent the range of dielectric properties that are exhibited by biological tissues. By examining the dielectric properties of such a large variety of TMMs, it is possible to identify concentrations of graphite and carbon black needed to match the dielectric properties typical of fat, gland, skin, and tumour tissue types in order to fabricate a realistic carbon-based breast phantom.

Measurements were done with an Agilent Dielectric Probe Kit (85070E) with 201 points recorded, using a linear scale, from 100 MHz to 20 GHz. For each sample, ten measurements a day, from different locations on the sample, over a period of at least seven days were recorded; this data is then averaged to get a mean-representation of the complex permittivity of the sample. The relative permittivity and conductivity, for all twenty

TMM-samples, over the 1 – 10 GHz range is shown in Fig. 4.1. These plots focus on the 1 – 10 GHz range as the majority of microwave medical devices operate in this frequency range.

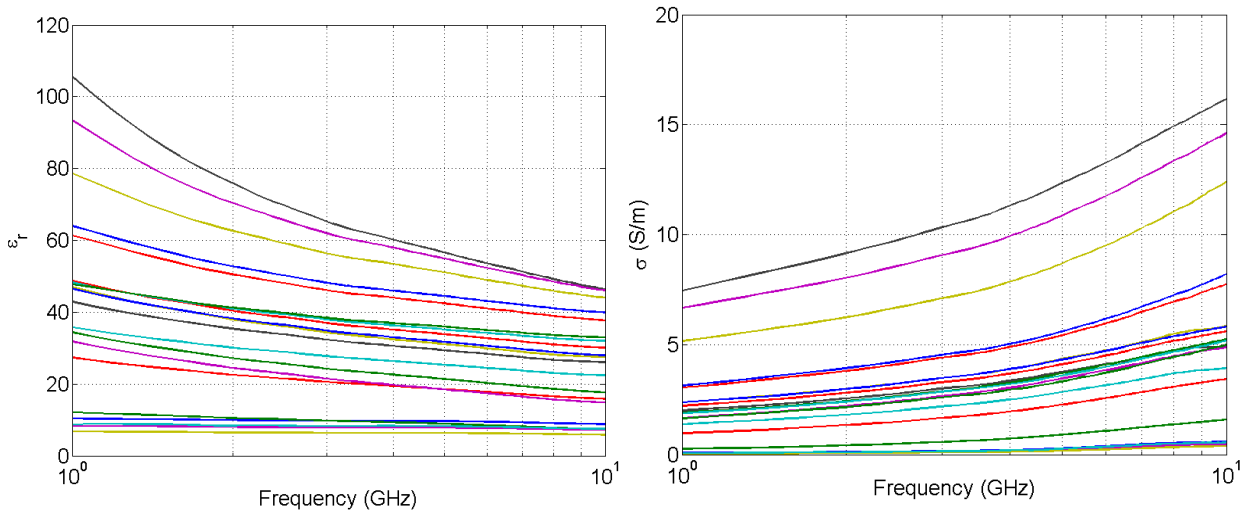

Figure 4.1. A comparison of the relative permittivity (left) and the conductivity (right) of all 20 different TMM-samples that were fabricated over the 1 – 10 GHz frequency range.

The measurements shown in Fig. 4.1 demonstrate that the fabricated TMM-samples can span a very wide range of permittivities in the microwave frequency range. Additionally, these plots show that the use of the modified fabrication procedure, with the use of acetone, allows for high permittivity and conductivity TMMs to be fabricated; addressing the issues raised in [102] where the fabrication of such TMMs were impossible due to the difficulties mixing the amount of graphite and carbon black required. Adding acetone to the mixture acts as a thinning agent, decreasing the viscosity of the mixture and allowing for more graphite and carbon black to be mixed. The addition of acetone also increases the permittivity and conductivity of a given TMM-sample. Figure 4.2 demonstrates the effects on the dielectric properties of a high-permittivity TMM-sample when adding 5 mL of acetone (the amount of graphite and carbon-black are unchanged, by total mass).

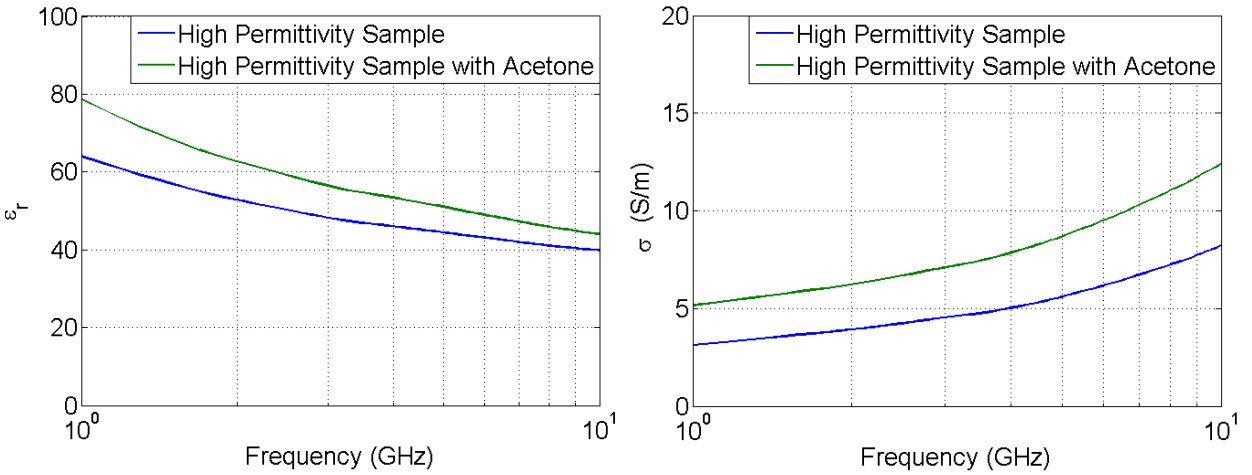

Figure 4.2. The effects of adding 5 mL of acetone on the relative permittivity (left) and the conductivity (right) of a high permittivity TMM-sample over the 1 – 10 GHz frequency range.

During the fabrication process, it was often seen that the vigorous mixing process can induce a large number of air bubbles to form in the rubber-carbon solution. These air bubbles can be partially mitigated by ensuring a very slow pouring procedure into the final container shape. However, this only helps to mitigate some of the air bubbles, as some will continue to be trapped into the final mixture. One solution that was investigated was to use degassing techniques to remove the trapped air bubbles in the mixture by using a vacuum pump. However, this solution requires that the mixture remain in a liquid state, thus it was only applicable to low permittivity TMMs. An example on the effects of degassing are shown in Fig. 4.3. It can be seen that removing the air bubbles does have a slight impact on the dielectric properties; as expected from removing air from the samples, there is a slight increase in the permittivity and conductivity over the 1 – 10 GHz frequency range. However, this change is very slight, and is less than 5% across all frequencies. Thus, for most experimental designs, degassing is unnecessary.

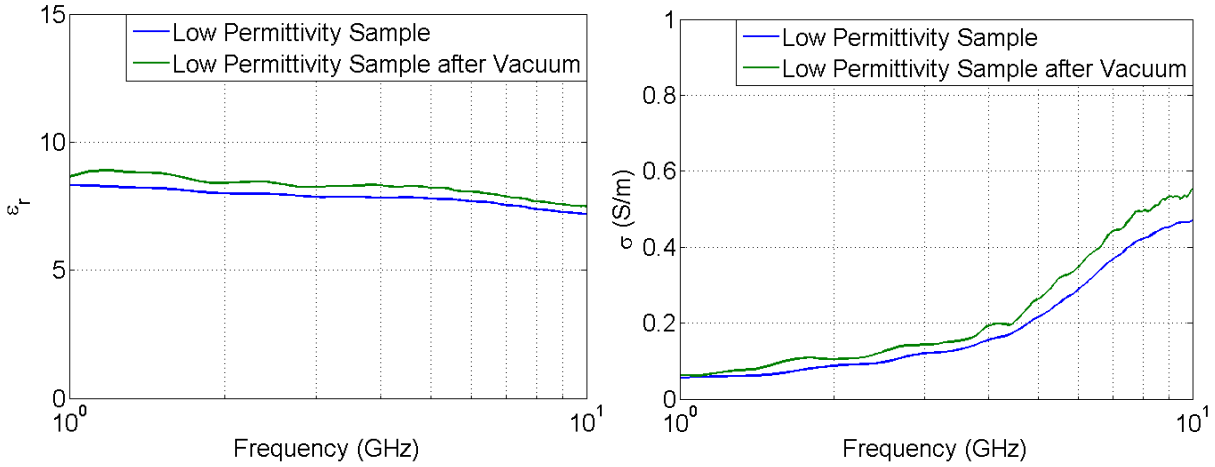

Figure 4.3. An example on the effects of degassing on the permittivity (left) and the conductivity (right) of a low permittivity TMM-sample, over the 1 – 10 GHz frequency range, using the vacuum pump technique.

Finally, recordings were taken with the twenty different TMM-samples measurements weekly for the first four months after fabrication. These measurements were then repeated one year later. The results confirmed what was observed in [102]; the changes in the dielectric properties of the carbon-based TMMs are very stable, with a measured difference of only $\pm 5\%$ over a prolonged time frame.

As shown in Figures 2.3 – 2.7, human tissues can span a wide range of dielectric properties. This is particularly true for glandular and tumour tissues, as the percentage of identified cells in the measured sample can greatly influence the overall permittivity making it difficult to precisely determine the dielectric properties solely of the glandular or tumorous tissues. Further, the same tissue type can have properties that vary significantly from one patient to the next. For this reason, TMMs should be designed in such a way that the range of expected human tissue properties is covered.

In Fig. 4.4, plots of the relative permittivity and conductivity of the twenty different TMM-samples are divided into three groups: high, medium, and low dielectric property ranges. The curves are plotted such that each coloured region represents the measured

data from all samples falling within that specific category (the upper and lower bound of each group is from actual measured data).

The high permittivity range represents the TMMs that can be used to mimic the high-water content tissues in the human body; more specifically, this group has properties that align around the reported median properties reported in the literature for breast tumour samples [9], [24]. The medium permittivity range represents the TMMs that can be used to mimic skin and gland breast tissues [9], [24], [27], and the low permittivity range is for TMMs that will mimic the high-adipose tissues in the breast [10], [24].

In Table 4.1, the range of concentrations, by percent weight (wt%), for graphite and carbon black that can be used to fabricate TMMs that match the reported dielectric properties for fat, skin, gland, and tumour are presented. This table represents a summary for the fabrication of specific TMMs that match the tissues of the breast.

It is found that for fat-mimicking tissue, a mixture of only graphite and polyurethane satisfactorily reproduces the desired dielectric properties. For the other tissues, a combination of graphite, polyurethane, and carbon black must be used. The fabrication of the tumour TMMs required the addition of between 3 and 8 mL of acetone.

TABLE 4.1. RANGE OF CONCENTRATIONS, BY WEIGHT, OF GRAPHITE AND CARBON BLACK THAT ARE USED TO CREATE EACH TISSUE TYPE. A "*" INDICATES THAT ACETONE WAS ALSO ADDED TO THE MIXTURE [104]

Graphite (wt.%)	Carbon Black (wt.%)	Tissue Type
[15.0 - 25.0]	0.0	Fat
30.0	[5.5 - 6.5]	Skin
[35.0 - 42.5]	[3.0 - 5.0]	Gland
[42.5 - 45.0]	[3.0 - 4.0]	Tumour*

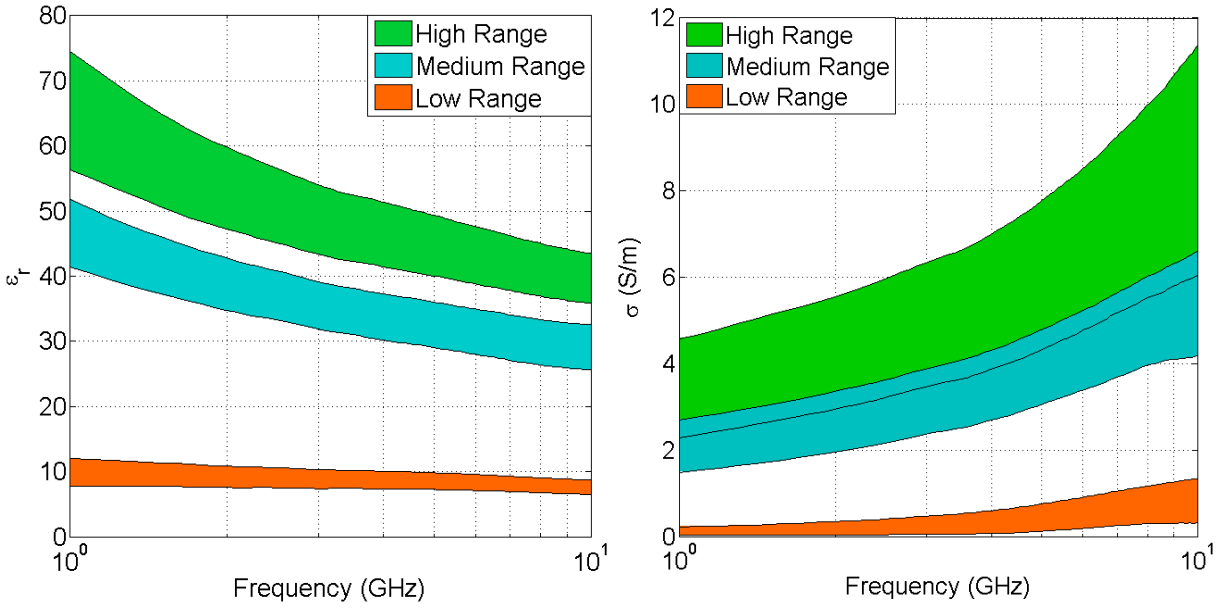

Figure 4.4. Measured relative permittivity (left) and the conductivity (right) for TMMs of high (green), medium (blue) and low (orange) dielectric properties. Modified from [104].

4.3 Fabrication of Realistic Breast Phantoms

In this section, the steps necessary to create a stable, heterogeneous, and modular breast phantom from the carbon-based TMMs are presented. A sequence of photographs that describe the fabrication process for these breast phantoms is shown in Fig. 4.5. The first image illustrates a thin, 2.5-mm shell of skin-mimicking material; the skin phantom must be fabricated first so that the other tissues can be placed inside of it. The next picture shows the complex glandular structures, chosen to encompass a specific volume and placed at a desired location within the breast phantom. The glandular structures are manually carved and shaped to mimic a real-life scenario, wherein they originate at the nipple and expand outwards toward the chest wall. Next, a photograph of the process of filling the area around the glands with the fat TMM is shown. During this process, a small metal cylinder is used to create a cylindrical hole inside the phantom. This hole can be filled with a 'plug'. A plug is a cylindrical object that exactly matches the size of the hole in the phantom. This exact match is created by first making a counter mould of the metal

cylinder, and then using that mould to create plugs. Plugs can be made of any combination of TMMs, allowing a variety of different plugs to be used with each breast phantom. Finally, a photograph of a complete phantom, with several different plugs, is shown.

Figure 4.5. A set of four images depicting the phantom fabrication process (clockwise from top left): empty skin, placement of glandular structures, filling the breast with adipose tissue while maintaining a spot for the plug, and a complete phantom with several plugs, [104].

The use of these plugs allow for these breast phantoms to be modular in nature. The plugs may contain only healthy (fat or gland) tissues, a tumour embedded within the fat or gland, different contrasts between the tumour and healthy tissue, and different depths or sizes of tumours. The plugs enable rearranging of the phantom structure to maximize the number of effective scenarios. While not demonstrated here, it is also possible to

fabricate breast phantoms with multiple plugs, allowing for the possibility of multiple tumours to be embedded in the phantom. A schematic that provides an example of what the plugs look like and a subset of some of the plugs that can be fabricated is shown in Fig. 4.6.

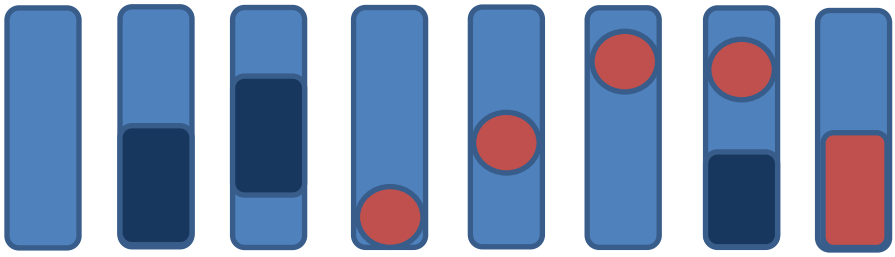

Figure 4.6. A schematic depicting a variety of different potential plugs that can be fabricated, some composed entirely of fat tissue, some composed of fat and gland, fat and tumours (of varying size), and of all three tissue types. The pale blue represents the adipose TMM, the dark blue represents the glandular TMM, and the red represents the tumour TMM.

4.4 Carbon-Based Breast Phantom Verification

In this section, data is collected from realistic carbon-based breast phantoms with the experimental system presented in Section 3.1. This measurement data is used to verify that the breast phantoms can be used for testing and validating an experimental microwave system for breast health monitoring. Using these new breast phantoms, the same validation tests of the system as was carried out in Chapter 3, the generation of reconstruction images and use of classification algorithms, are performed.

In [104], six homogeneous phantoms, each with a different relative permittivity, ε_r, and conductivity were fabricated (made from a different adipose TMM). For these phantoms, the relative permittivity ranged from 6 to 10 at the centre frequency of 3 GHz. In addition, three heterogeneous phantoms, with approximately 23%, 37%, and 50% glandular content by volume were fabricated. The glands have a relative permittivity

between 36 and 39 at 3 GHz. For the heterogeneous breast phantoms, the background adipose tissue has a relative permittivity between 6 and 10, depending on the phantom, at 3 GHz. All phantoms have a layer of skin (2.5 mm thick, $\varepsilon_r = 35$ at 3 GHz). Each of these phantoms has a singular 'plug' hole location. A total of 6 different plugs were used during this study. Within each plug, there may be only healthy-mimicking tissues (e.g., fat tissue, of any given ε_r) to represent the healthy baseline case, or there may be an embedded tumour (ε_r of 55 to 65 at 3 GHz, depending on the plug) to represent the case where a cancerous tumour has developed within the breast. The tumours considered were roughly spherical with a 1-cm radius, embedded in fat-mimicking tissue.

Measurements were performed on all nine fabricated phantoms. In addition to these phantoms, six extra phantoms were artificially synthesized by rotating the three heterogeneous phantoms by 120° and 240° from their original position. As the antennas are distributed around the radome in 90° subdivisions, this rotation will alter the region that is scanned by each quadrant of the antenna array. The net result is a total of 15 distinct phantoms that were used in this study.

Data is recorded from 'healthy' and 'tumour-bearing' phantoms every day over a period of twenty days. In between each scan of the same phantom, one day had passed and the phantom was removed from the system and then replaced. This scan procedure mimics the clinical scenario; the patient has one scan on each visit, each subsequent visit will lead to a new scan, thus each scan will have some inherent difference in the exact positioning of the breast within the radome. For each phantom, a total of 10 healthy scans and 10 scans with tumour were obtained. Healthy scans are here denoted by "B_x", where $x = 1{:}10$, and ones with tumour as "T_y", $y = 1{:}10$, for each phantom.

Reconstruction images of all the breast phantoms were generated from the differential data set using the DMAS imaging algorithm. As before, prior to applying the imaging algorithm the pre-processing methods (filter, alignment, normalization) to mitigate noise,

jitter, and other random measurement errors were applied. The use of differential signals replicates the goal of monitoring, where only changes that occur between breast scans need to be analyzed. In this way, a differential image of B_x using B_1 as calibration ("$B_x - B_1$") represents healthy changes in tissue between the x^{th} scan and the initial scan; on the other hand, "$T_y - B_1$" is a scenario in which a tumour has developed between the y^{th} tumour scan and the initial healthy scan. In this study, however, the phantoms were stable and thus no significant healthy tissue changes between scans was observed. Therefore, changes in images B_x - B_1 are predominantly attributed to repositioning of the phantom in the radome, and the effects of random noise. Using this procedure, a total of 275 images were generated.

In Fig. 4.7, a subset of the reconstructed images are shown. Four reconstructed images from two different phantoms, one homogeneous the other heterogeneous, are depicted. For each phantom, an image is shown representing the healthy difference and tumour difference. Each image is normalized to the maximum pixel intensity of the tumour scan for that phantom. Fig. 4.7 (a)-(b) shows a perspective view of the healthy case for a homogeneous and heterogeneous phantom, respectively. Fig. 4.7 (c)-(d) shows a perspective and side view, respectively, of the tumour embedded in a homogeneous phantom. Finally, Fig. 4.7 (e)-(f) shows a perspective and side view, respectively, of the tumour embedded in a heterogeneous phantom. As can be seen from the images, there is a clear difference between the healthy case and the case in which a tumour is present. We note that in the heterogeneous case there is a higher level of background clutter than in the healthy case and, as a result, it is more of a challenge to correctly identify the tumour location. As the heterogeneity is increased, the imaging methods struggle to identify and localize the presence of the tumour as the contrast between the malign and healthy tissues is decreased. It is also noted that the tumours are mostly located in the half of the breast closer to the chest wall as very few tumours occur near the nipple.

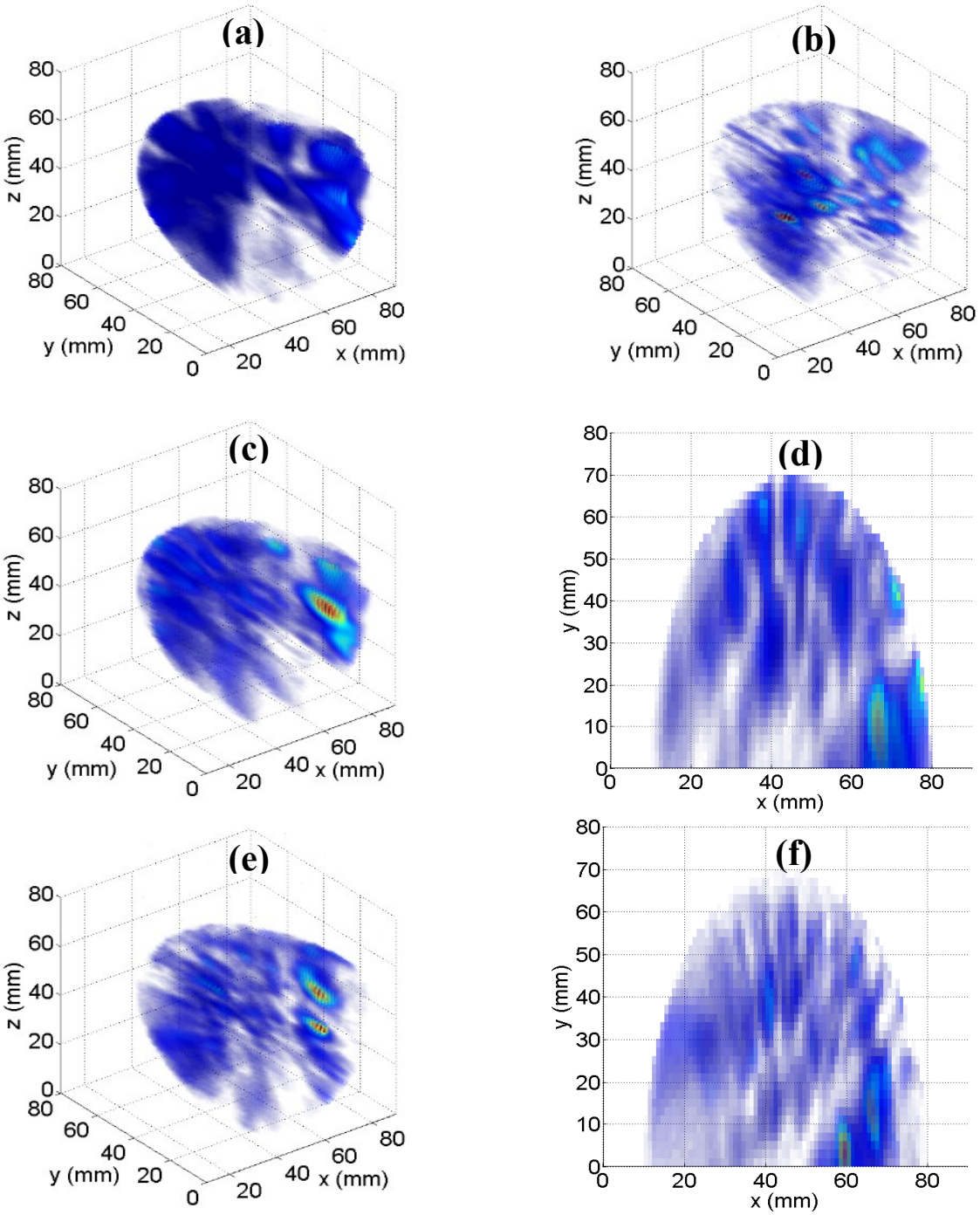

Figure 4.7. Comparison of images of the various types of phantoms for both healthy and tumour scans, [104]. (a) - (b) Perspective view of the homogeneous and heterogeneous baseline (healthy) scans, respectively. Perspective and side view, respectively, of the tumour embedded in the homogeneous phantom (c) - (d) and of the tumour embedded in the heterogeneous phantom (e) - (f).

In Section 3.5.2, the use of machine learning classification algorithms, namely SVM and LDA, were demonstrated to be a useful tool when classifying whether a breast scan is from a healthy or tumour-bearing phantom. Another possible method to do classification is to use the maximum pixel intensity of an image. In Fig. 4.8 a histogram of the maximum pixel intensity for each of the images generated, on a $\log_{10}$ scale, is shown. There is a noticeable separation between the distributions of the healthy and unhealthy scans in regards to the maximum pixel intensity. This suggests that it might be possible to make a binary classification of a breast scan (healthy or unhealthy) based on the maximum pixel intensity. A simple method to implement such a classification is to use a threshold method; if the maximum pixel intensity is greater than a specific value then the scan is from a tumour-bearing scan, if it is lower it represents a healthy scan. A receiver operating characteristic curve (ROC) curve is a graphical plot that can be used for a classifier to contrast its performance (in this case defined as the true positive rate) as the false positive rate is varied. The ROC curve is a useful measure to identify the ideal operating parameters of a classifier (based on the limits of the acceptable false positive rates). In this case the false positive rate is controlled by the choice of the maximum pixel intensity threshold value. The ROC curve for the classification of a breast scan based on the maximum pixel intensity of the image is shown in Fig. 4.9. From this curve, it is possible to extract specific information on the detection rate at certain false-positive limits. For example, when the false-positive rate is limited to 10%, the true positive rate is just under 72%, as the false-positive rate is increased further to 20%, the detection rate is now above 82%. The ROC curve allows the performance of the classifier to be easily assessed with a graphical plot.

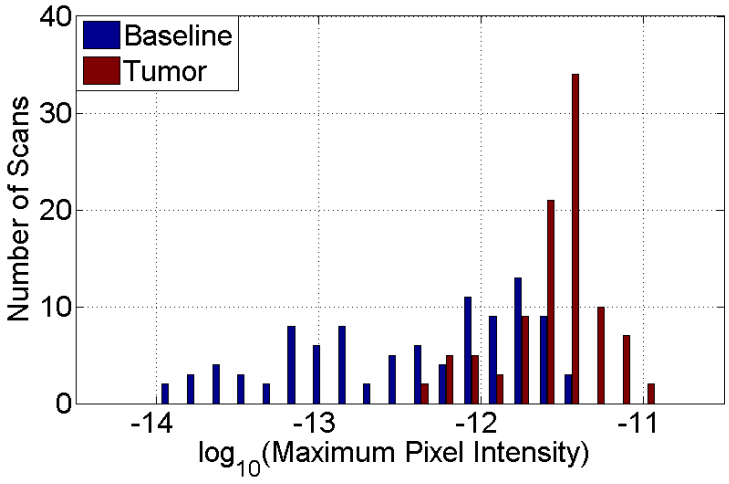

Figure 4.8. A histogram comparing the $\log_{10}$ value of the maximum pixel intensity of each image for the two types of scans, healthy baseline and when the tumour is embedded in the phantom, [104].

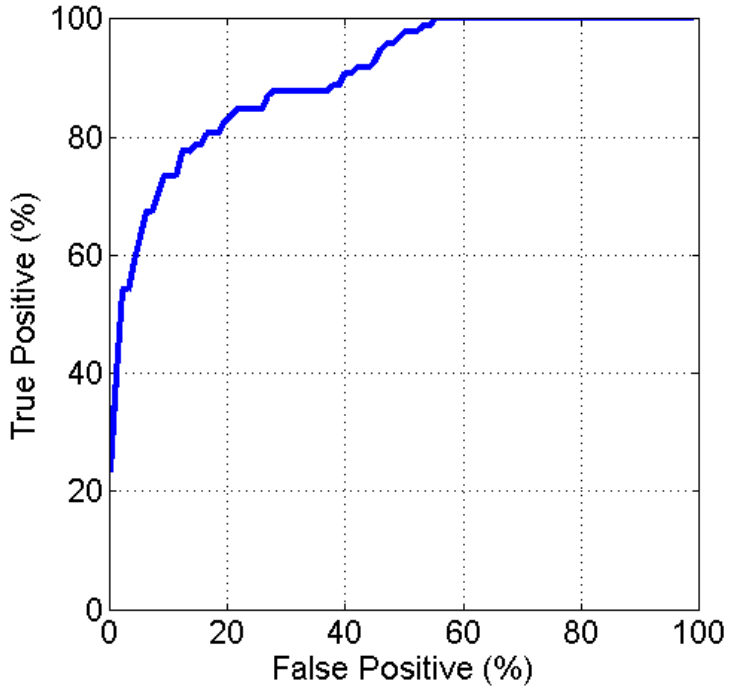

Figure 4.9. The ROC curve for a simple threshold classifier based on the maximum pixel intensity of reconstructed images, [104].

In [105], the use of an improved ensemble classifier was tested with the set of carbon-based rubber phantoms. This work was a continuation of the work proposed in

[78] and [79], where the SVM classifier was used to detect the presence of a tumour in the breast scan data. The novel work in [105] was to use a cost-sensitive ensemble classifier. A cost-sensitive classifier, in this case the 2ν-SVM, allows for the control of the false-positive rate. During the training of the 2ν-SVM classifier it is possible to set bounds on the maximum false-positive rate during the search for the ideal operating parameters of the classifier, hence it offers significant promise for use in a system to be used as a screening tool for breast cancer.

In [105], two ensemble classifiers were tested: the classifier fusion method, where the outputs of each classifier is averaged and then a threshold value is used to control the decision making process, and a feature fusion classifier, where the outputs from the feature extraction method PCA were concatenated and then used as the input to the 2ν-SVM classifier. In both cases, the training data set consists of the data from 13 phantoms, and the test set was from the remaining two phantoms. The results were the average performance of the classifiers after all possible permutations of the training and testing data sets were examined; in total there were 105 total training and testing combinations. In training a 13-fold cross validation was performed to identify the ideal operating parameters for the classifier. The number of principal components to be used was set to 30, and the maximum false-positive rate set by the 2ν-SVM during training was set to 5%. The final result is that both ensemble classifiers perform extremely well, and vastly outperform both the classifiers presented in Section 3.5.2, and the image based classifier discussed previously in this section. For the classifier fusion method, the detection rate is 99% when the false positive rate is held to 5%; for the feature fusion classifier, the detection rate is 96% when the false positive rate is held to 5%. This demonstrates that the presence of the embedded tumour in the carbon-based phantoms can be detected using classifications methods. Further, these new cost-sensitive ensemble classifiers work extremely well, even with heterogeneous breast phantoms.

4.5 Verification of TMMs with Standard Imaging Modalities

This section is focused on verifying the interior of the carbon-based TMMs, under high resolution, using standard imaging modalities such as MRI and computed tomography (CT), and assessing the performance of these standard imaging modalities when low contrast inclusions are embedded in a carbon-based phantom. This study is part of a preliminary collaboration work with Goethe University in Germany on comparing the images from a microwave system with MRI, CT, and other standard imaging modalities.

A large (235 mm x 235 mm x 100 mm) experimental carbon-based phantom, made up of a mixture of graphite and polyurethane, was fabricated. The phantom was made up of a background material, 20% graphite by weight, and four cylindrical inclusions, 25% graphite by weight. The cylindrical inclusions have diameters of 5, 10, 15 and 20 mm, and are 60 mm in length. Due to the time-sensitive nature of the graphite-polyurethane mixture, it begins to set within 15 minutes, there are limitations on the volume of a phantom which can be fabricated in one instance. Thus, due to the large size of the desired phantom, it was necessary to fabricate the phantom in stages. First, a 10 mm base layer of the background material was poured into the phantom mould. Four counter-moulds of the inclusions are placed in the phantom mould and the surrounding area was filled with the background material. This process of filling the background material around the inclusion counter-moulds was repeated until the phantom was 70 mm tall. At this stage the inclusion counter-moulds were removed. The partial phantom is 70 mm tall with four holes whose size matches the desired inclusion size exactly. The holes were then filled with the inclusion material. Once the inclusion material is set the phantom was finalized by

filling the phantom mould with the background material until the desired height was reached, thus the inclusions were embedded within the phantom with minimal air gaps.

An example of the finalized phantom is shown in Fig. 4.10. A comparison of the relative permittivity and the conductivity of these two materials is shown in Fig. 4.11.

Figure 4.10. A photograph of the finalized large scale rubber phantom. There are four inclusion embedded within the phantom.

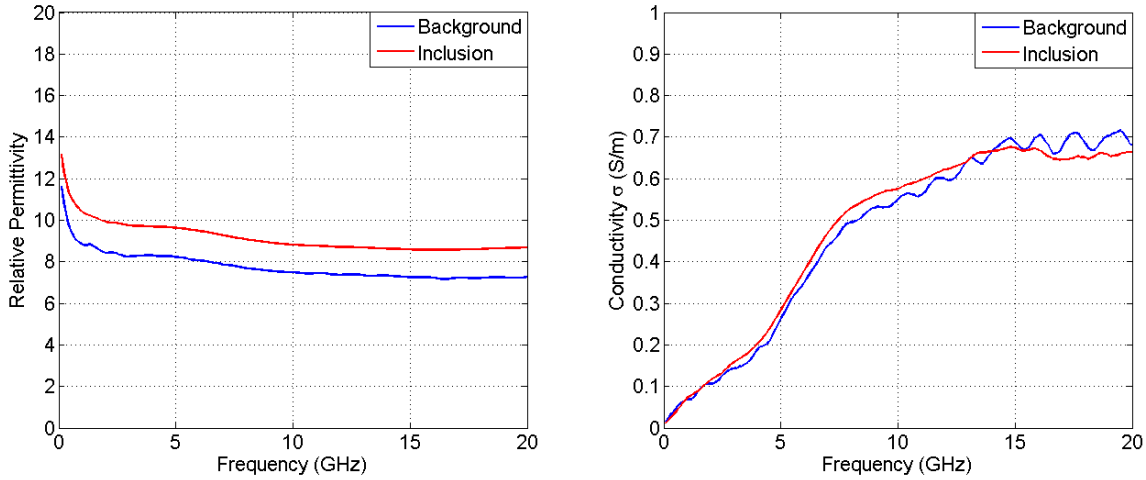

Figure 4.11. Comparison of the relative permittivity (left) and conductivity (right) of the background and inclusion materials.

To assess the quality of the phantom, high resolution images were obtained from a MRI scanner and a CT scanner. The MR images were acquired on a 3-tesla scanner (Siemens Magnetom Verio). A 2-D coronal slice of the 3-D volumetric MR images is shown in Fig. 4.12. In the image, various regions of interest (ROI) have been defined, these areas are marked by the small circles shown in Fig. 4.12. The pixel values inside the ROI in terms of mean and standard deviation are evaluated for comparison purposes. As shown in Fig. 4.12, the signal intensity recorded from the two inclusions on the right side of the image is almost the same (349 and 342) and differs from the one recorded in the surrounding phantom material (509). This demonstrates that the small contrast between the inclusion and the background material can be differentiated by an MRI scanner. Additionally, there are smaller streaks that can be seen that run through the phantom. These are believed to be air bubbles (based on the low pixel intensity), but the phantom must be cut up to confirm this result.

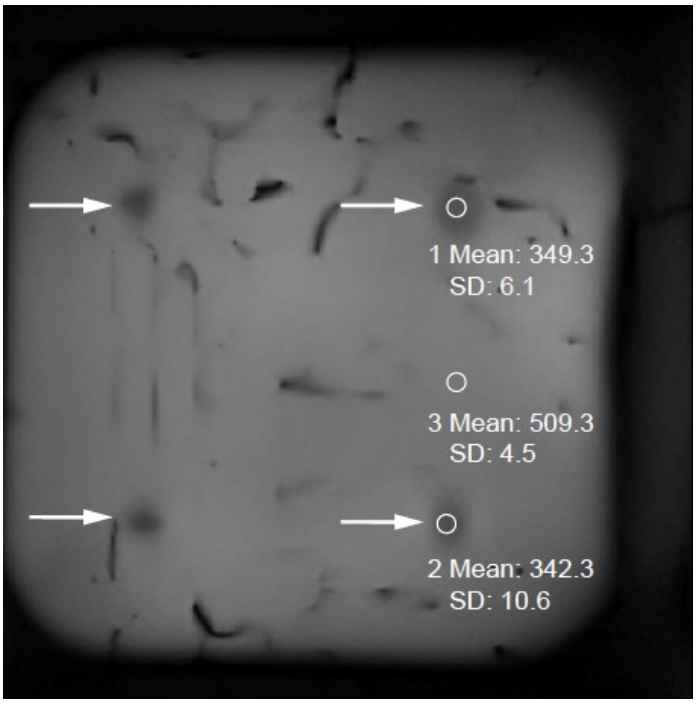

Figure 4.12. Cross-section through the volumetric MRI image. Four shadow-like regions can be observed at the intended inclusion positions.

The CT acquisition was performed on a dual source scanner (Siemens Somatom Force). A 2-D coronal slice through the 3-D volumetric CT images is shown in Fig. 4.13. The two inclusions on the right side have, as in the case of MR acquisition, almost the same signal intensities; with CT numbers of 66 and 68 Hounsfield Unit (HU), respectively. For the background material a CT number of 46 HU is observed; thus, CT is also able to discern between the background and inclusion material despite the low contrast in the dielectric properties between the two. The inclusion sizes are comparable with the ones defined on the MR image. However, unlike the MR images, the CT images cannot detect the two inclusions on the left side accurately. As seen in Fig. 4.13, from the CT image it is observed that air is at the location of the left side inclusions.

Interestingly, with the CT images, a fine granular structure can be observed which may also be related to very small air gaps within the phantom. Comparing the MR- and CT-images leads to the conclusion that MRI outperforms the CT measurements in terms of spatial resolution as well as the ability to image the inclusion material. Further research is required to compare these high resolution images with those generated with a microwave system. Part of this future work will aim to identifying whether the presence of air bubbles is detectable with a microwave system.

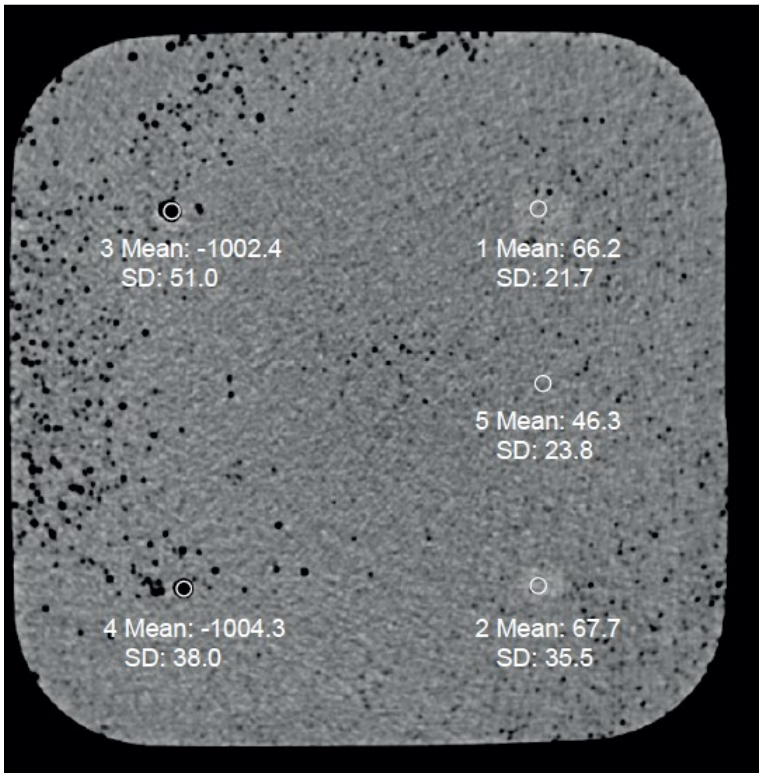

Figure 4.13. 2-D slice through the volumetric CT image showing the CT number at the locations of the inclusions.

4.6 Summary and Conclusions

In this chapter, the design and fabrication of TMMs that can represent a variety of biological tissues was presented. These TMMs are made from a combination of polyurethane, graphite, carbon black, and acetone. This work represents the first time that carbon-based TMMs have been fabricated to accurately model high water content tissues such as tumours and glands. The effects of acetone and degassing on the carbon-based TMMs were also analysed. Finally, permittivity measurements of twenty different TMMs, spanning a time frame of over 1 year, were presented.

This chapter also focused on the development and testing of realistic, stable and modular carbon-based breast phantoms. These phantoms can be easily fabricated from the carbon-based TMMs to include skin, glands, fat, and tumour tissues. The fabrication

method was outlined, and a method to make these phantoms modular by using phantom plugs that can contain a variety of tissues was also included. These phantoms were then tested using an experimental system, and measurement data confirmed that the phantoms can be used in the testing of a system for breast health monitoring.

Finally, high resolution images of these carbon-based TMMs were obtained using MRI and CT images of a large phantom that included four tumour inclusions of low dielectric contrast.

Chapter 5: Development of a Low-Cost System Prototype

This chapter is focused on the design, development, and testing of an experimental system that can be built from off-the-shelf components, to create a miniaturized and low-cost microwave system prototype. First, a multilayer flexible circuit with an embedded switching matrix and antenna array was designed to replace the bulky radome and switching matrix of the initial experimental system. This circuit was fabricated, characterized, and ultimately tested with phantoms after being integrated into a system prototype. These results have been published in [83], representing the first time that a switching matrix and antenna array were embedded in the same structure for a microwave medical diagnostic system. Secondly, based on these initial tests, the design for a second-generation of flexible circuit was completed. The next section of the chapter is focused on the identification, testing, and integration of several off-the-shelf components to create a low-cost system prototype that can be used in a screening protocol for breast cancer detection. Finally, this chapter concludes with a cost-comparison between the initial system prototype and the finalized low-cost design.

5.1 A Flexible Multi-Layer Circuit System

5.1.1 Motivation

In both TD and FD microwave systems for breast cancer detection, multiple antennas can be placed around the target area to gather information from the breast interior. The use of a switching matrix enables each antenna to communicate with the other antennas [38], [47], [50] – [52], [54], [76]. This switching matrix is usually fabricated by a custom-built cascade of electromechanical switches [47], [76], or as a commercially available device

[50] – [52]. Additionally, microwave systems for medical purposes other than breast cancer also often require a switching matrix, such as those in head imaging and stroke detection [55], [106], and in bladder-monitoring [58]; currently these systems use electromechanical switches. Significantly, these electromechanical switches are typically larger, slower, and several orders of magnitude more expensive than other switching options.

These drawbacks of using electromechanical switches has fuelled the search for possible alternatives. One alternative is to use a single antenna that can be rotated around the target, and the monostatic data is recorded at many locations, as in [40], [57]. However, this approach limits the amount of data attainable to only monostatic information and requires the implementation of an accurate motor-control. Further, only a small number of measurements is possible within a reasonable measurement time. Most recently, the research group at Hiroshima University has developed a custom-built 8×1 switch implemented in CMOS technology, fabricated on a PCB, [54], [107], intended to replace their commercially-available 16x2 switching matrix. However, their system switches between 8 distinct transmit antennas and 8 distinct receive antennas, all of which are located off-board; requiring a set of RF cables for each antenna. The other possible alternatives are to use microelectromechanical systems (MEMS) or solid-state switches to design a switching matrix. Solid-state switches remain considerably cheaper (approximately 50 times) than MEMS switches, enabling the design of a compact, low-cost system.

In this section, the design of a flexible PCB that incorporates a 16×2 switching matrix, composed of solid state switches, with an integrated 16-element antenna array, is presented. To date, there have been a few demonstrations of a microwave medical diagnostic system that made use of a solid state switching matrix [38], [108]; however, none of these designs integrated the switching matrix and antennas on a single circuit board without the need for cumbersome RF cables.

Furthermore, the design presented in this chapter is fabricated on a flexible substrate, allowing it to conform to the shape of the breast; thus, the electromechanical switching matrix, the antennas, and the antenna radome of our previous system design, are all integrated on one circuit board. By integrating these elements, the overall cost and size of the system has been significantly reduced. The cost savings are due to the reduced number of RF cables required for the system (only two RF cables are required, compared to 50 in the original system [76]), the removal of an antenna housing structure, and by the lower associated cost with solid state switches compared to their electromechanical equivalents. Additionally, since this flexible circuit was implemented in printed circuit board (PCB) technology, mass production becomes more straightforward. Not only does this reduction in the number of RF cables represent a saving in cost, size, and hardware complexity, it also improves matching and eliminates any potential source of noise due to cable movement and position [109].

5.1.2 System Design

A top-level block diagram of the system is presented in Fig. 5.1. The basis of this system is similar to that of the original system described in Chapter 3. An impulse generator was used to provide -7.5 V quasi-Lorentzian impulses of 70 ps full-width half-maximum which were subsequently re-shaped by a custom reflection-mode filter implemented in microstrip technology [64]. The resulting RF pulse featured energy concentrated in the 2 – 4 GHz frequency band. This pulse was then amplified by +35 dBm and passed to the main circuit board through coaxial cable edge-connectorized to the board using a 50 Ω end-launch connector (Southwest Microwave 292-07A-5). The system output (bearing received pulses after transmission through the breast) was connected to the sampling input of a digitizing oscilloscope (Pico Technology PC Oscilloscope 9201) and transmitted to a laptop for analysis.

The switching network was designed using a cascade of 4×1 and 2×1 switches. The network was divided into quadrants, with each quadrant controlling four antennas. A core switching region selects one of the quadrants, allowing each of the 16 antennas to independently act as either a transmitter or receiver. A detailed schematic of the switching network is shown in Fig. 5.2.

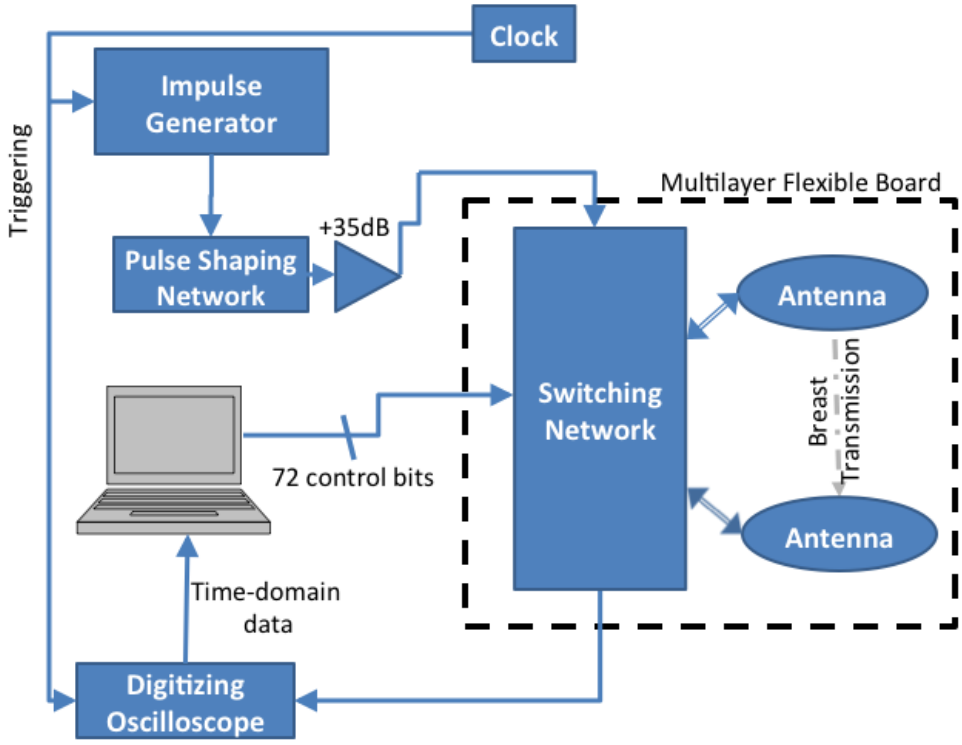

Figure 5.1. Top-level block diagram of the time-domain system [83].

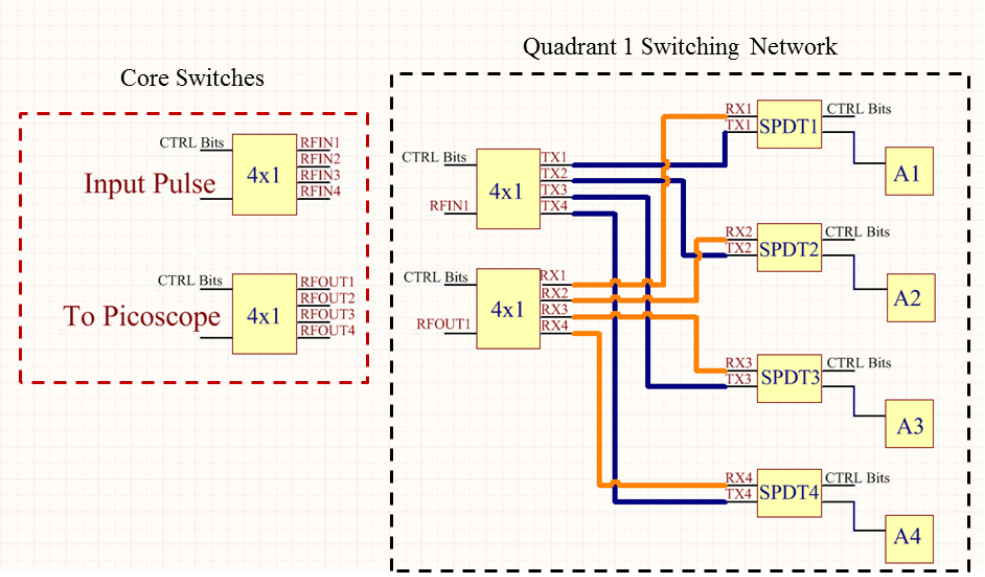

Figure 5.2. A detailed schematic of the switching network, [83]. The core of the switching network is a pair of 4x1 switches that connect the input pulse or the recording Picoscope to one of four quadrants. The remainder of the network is divided into four equal quadrants. The design of Quadrant 1 is shown in the figure. Each quadrant consists of two 4×1 switches, one for the transmit (TX) and receive (RX) signal chains, and 4 single-pull dual throw (SPDT, 2×1) switches to allow each antenna (labeled as A1 – A4) to be connected to the TX or RX signal chains as required. The transmit connections are highlighted in blue, while the receive lines are highlighted in orange. Each switch is controlled via the voltage control bits from a laptop controlled microprocessor.

The first decision in the design of the multilayer flexible circuit board was the selection of an appropriate board substrate. Since GHz-range signals had to be routed, with minimal losses, on traces having a length commensurate with the human breast, a low-loss material was sought that would preserve flexibility even when multiple layers were stacked to support the necessary routing network. To achieve the necessary routing, a four-core multilayer design using a liquid crystalline polymer core material, Rogers UltraLAM® 3850 ($\varepsilon_r = 2.9$, $\tan\delta = 0.0025$), with five active metal layers was employed. This material exhibits low-loss in the 2 – 4 GHz range and has a low tensile modulus (high flexibility).

The layer stack-up can be seen in Fig. 5.3, and the functionality for each metalized layer can be explained as follows: the top layer contains all the soldered electronics (switches and capacitors) and the microstrip traces that route the RF signals. The first

inner layer, L_1, was used as a common ground for the microstrip traces on the top layer and on the second inner layer, L_2. The second inner layer also contains the DC control lines for the switches. The third inner layer, L_3, contains the embedded patch antennas. The bottom-most metal layer was used sparingly for soldering some through-hole ribbon-cable connectors and is etched away everywhere else.

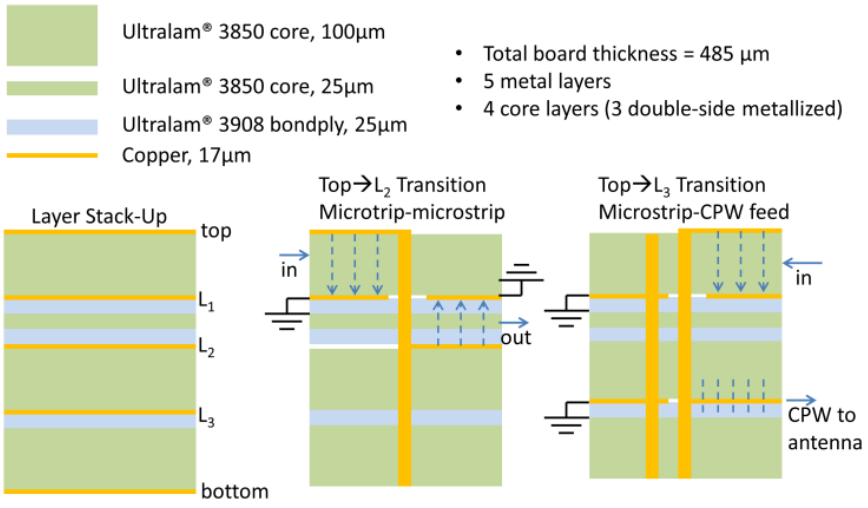

Figure 5.3. Layer stack-up of finished board (left), including side-views of inter-layer transition geometries for microstrip-to-inverted-microstrip (middle) and microstrip-to-CPW-feedline (right), [83].

All of the microstrip traces have been designed to ensure an input impedance of 50 Ω. This was accomplished using a full-wave electromagnetic simulation software package (HFSS, Ansys Co.), using a parametric search to determine the optimal trace thickness for the two sets of RF traces, those on the top layer and the embedded traces on L_2. The optimal trace widths were found to be 0.28 mm and 0.27 mm, for the top and L_2 layers, respectively. Additionally, the use of a simulation package such as HFSS allowed for the calculation for the path loss for each trace across different frequencies. The path loss for each of the microstrip traces is summarized in Table 5.1. Traces on the L_2 layer experience greater attenuation, due to the thinner dielectric between the ground plane and the microstrip, thus, the number of traces on the L_2 layer will be kept to a minimum.

TABLE 5.1. MICROSTRIP PATH LOSS AT THREE KEY FREQUENCIES, ON DIFFERENT ROUTING LAYERS

Microstrip Path loss (dB/cm)	Frequency		
	2 GHz	3 GHz	4 GHz
Top Layer	0.104	0.147	0.181
L_2 Layer	0.138	0.202	0.266

The layout design of the flexible circuit board, including antennas, electronics, and DC and RF traces, is shown in Fig. 5.4. The functionality of the flexible board, specifically the switching matrix aspect, can be described as follows: From the edge of the board, a top-layer microstrip trace (using layer L_1 as a ground, visible as pink regions in Fig. 5.4) is used to transport the RF input pulse to two cascaded sets of surface-mounted 4×1 RF switches (SKY13322-375LF). These switches were selected for their low insertion loss (0.45 dB), bandwidth extending to 6 GHz, and good linearity at the signal power levels required (P1dB = +30 dBm, the input signal to the board had a peak voltage of 28.5 dBm). All switches on the board were computer-controlled using a parallel set of 72 DC control lines (routed in layer L_2, yellow traces in Fig. 5.4), that were connectorized in four places near the board edges using standard 90-degree ribbon cable connectors. Computer control of these DC lines was used to route RF signals between any two of sixteen on-board antennas, resulting in a 16×2 switching matrix. During a typical scan, each of 240 possible pairings of antennas was selected in a programmed sequence for a total scan time of about 4.5 minutes when using 16 averages. Control was achieved using two STMicroelectronics model STM32-F4 Discovery boards.

Duck-unders allowing the RF traces to cross past each other were implemented in layer L_2 as needed using the layer-transition geometry shown in Fig. 5.3 (middle), which makes use of the common ground layer (L_1) for isolation between paths except at transition points. A final 2×1 switch (SKY13348-374LF) just before each antenna was

used to set it to either receive or transmit mode. Travel to the antenna (layer L_3) from the top layer was achieved by a via transition to the coplanar geometry of the antenna feedlines as shown in Fig. 5.3 (right). Once the pulse was transmitted through the breast tissue, the recovered signal from a chosen antenna was then multiplexed using a cascade of 4×1 switches to a single output trace running to the edge of the board and the output coaxial cable.

In order to make the flexible board conform to the surface of the breast, radial cuts were made in each quadrant of the design that made it possible to fold the square board into a quasi-hemispherical shape. The centre of the design, containing the densest electronics, is relatively flat during operation against the nipple region of the breast. Drill holes were added to the folded regions to make it possible to pin the board in a desired shape.

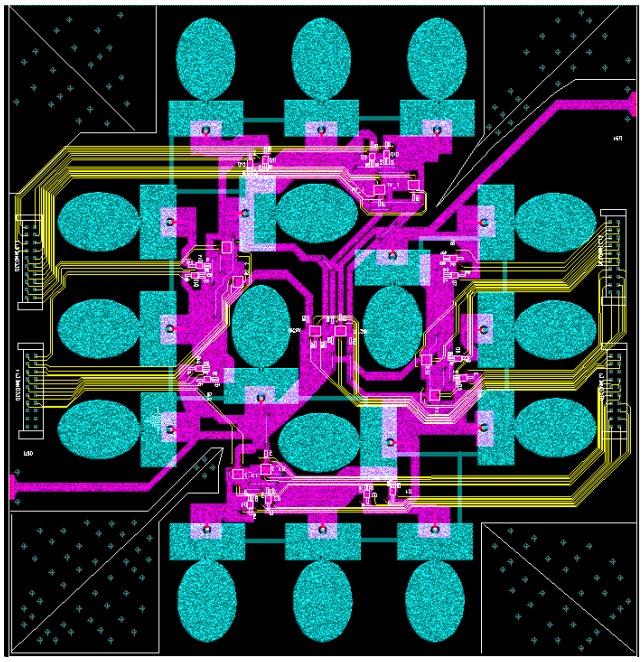

Figure 5.4. Layout illustration of the circuit board, designed with the PCB123 software [83]. The 16 ellipse-shaped antennas are shown in cyan, with DC control lines in yellow, and the microstrip ground in fuschia. Also shown are the radial cut-lines in each corner. The RF traces, on both the top layer and L_2 layer, cannot be seen as the common ground is covering them.

A photograph of the fabricated board is shown in Fig. 5.5; photographs of the board (from a top and side view) curved to demonstrate the flexibility of the finished design are also included. The size of the fabricated board is 20 cm by 21 cm.

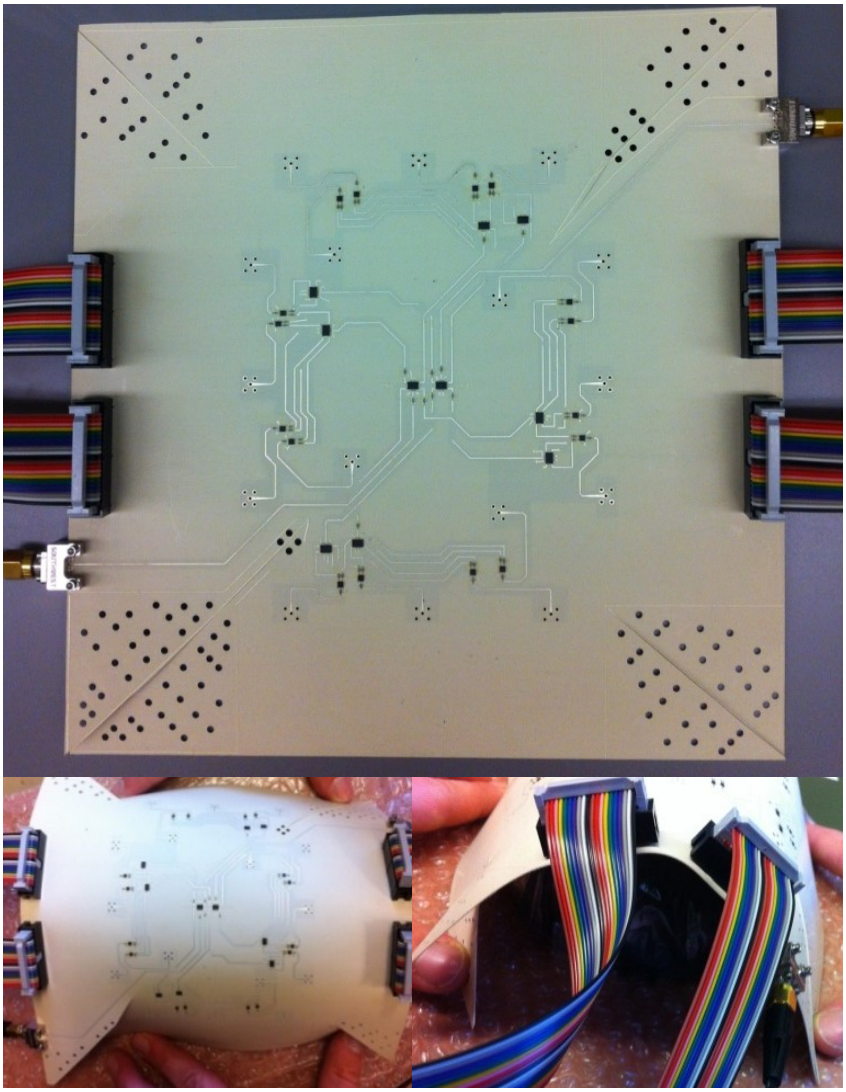

Figure 5.5. Photograph of the fabricated board lying flat (top). Example of the board held in a fully flexed position from the top view (bottom left), and the side view (bottom right), [83].

5.1.3 Antenna Design

The antenna integrated into the board is a modification of the design presented in [110]. It is a coplanar waveguide (CPW) fed elliptical patch antenna, designed for on-body operation in the 2 – 4 GHz range. The antenna presented in this paper has been altered from [110] for implementation in layer L_3 of the board, which required the antenna to be embedded between cores and to interface with the top-layer microstrip carrying the RF signals. The microstrip-to-coplanar waveguide transition (Fig. 5.3, right-side) is achieved by vias connecting the grounds and feed lines through the layers of the PCB. On the microstrip layer, the line is tapered from the size of the antenna coplanar waveguide feed (0.9 mm) down to the required microstrip width of 0.28 mm. The CPW feed lines were optimized using HFSS to achieve return loss below -10 dB and port impedance of 50 Ω over the frequency range of interest.

The numerical model for the antenna with the feed transition arrangement is shown in Fig. 5.6, along with a photograph of an isolated, connectorized antenna for experimental testing. The CPW dimensions were optimized through parameter sweep simulations, yielding a centre trace width of 0.9 mm and a gap of 0.12 mm. The antenna was optimized for operation in close contact with human tissues. The first layer, skin, had a thickness of 2.5 mm with relative permittivity $\varepsilon_r = 40$, conductivity $\sigma = 2$ S/m, and a loss tangent $\tan\delta = 0.2996$. The next layer mimicked the tissue with high adipose content (80 mm thick, with $\varepsilon_r = 10$, $\sigma = 0.4$ S/m, $\tan\delta = 0.2397$). The electrical properties for both tissues were chosen to match those of reported measurements [23], [28], at the centre of the considered frequency band. The simulated reflection coefficient, S_{11}, plotted in Fig. 5.7 in decibels (dB), is below -10 dB over the 2 – 4 GHz range. In fact, the maximum S_{11} over this band is -13.1 dB. Furthermore, the port impedance (Z_o) was expected to be well matched to 50 Ω: it was predicted to be 49.90 Ω at 2 GHz and 49.83 Ω at 4 GHz.

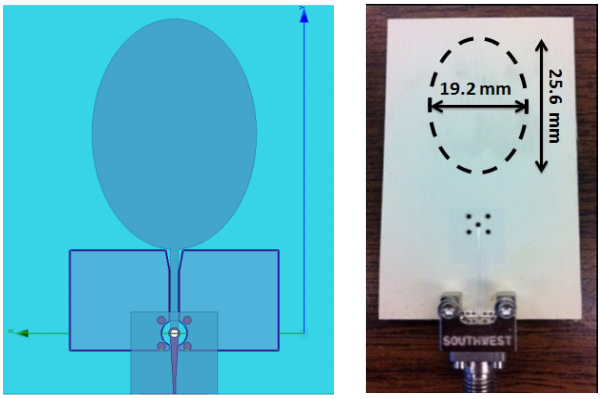

Figure 5.6. The elliptical patch antenna used in the board array [83]: Numerical model for embedded antenna with microstrip-to-coplanar waveguide feed structure (left), and the fabricated antenna connectorized to an edge-launch connector for testing (right). Note that only the top layer is visible as the antenna is embedded in the multi-layer board.

For the experimental testing, S_{11} was measured with the antenna contacting a carbon-based breast phantom, as described in Chapter 4, that was composed of a thin skin layer filled with fat-mimicking material. In this manner, the measurement was matched to the simulation scenario. An Agilent vector network analyzer (VNA, model 8722ES) was used to collect the S_{11} data. The VNA was calibrated using standards up to the antenna connector. A total of 1601 points were recorded from 1 GHz to 20 GHz. The resulting measured S_{11} is shown in Fig. 5.7. While the S_{11} still meets the criteria of being below -10 dB from 2 – 4 GHz, the measured S_{11} is several dB higher than the simulated S_{11}. One of the issues observed with the experimental testing, that may explain this discrepancy, is the proximity of the connector to the antennas, an issue that is not present in a fully integrated circuit board. This closeness to the board edge limited the flexibility of the antenna to conform to the surface of the breast phantom due to the physical barrier of the connector. Unfortunately, it was not possible to measure the S_{11} when the antenna was embedded in the board because the switching matrix does not allow for monostatic recording.

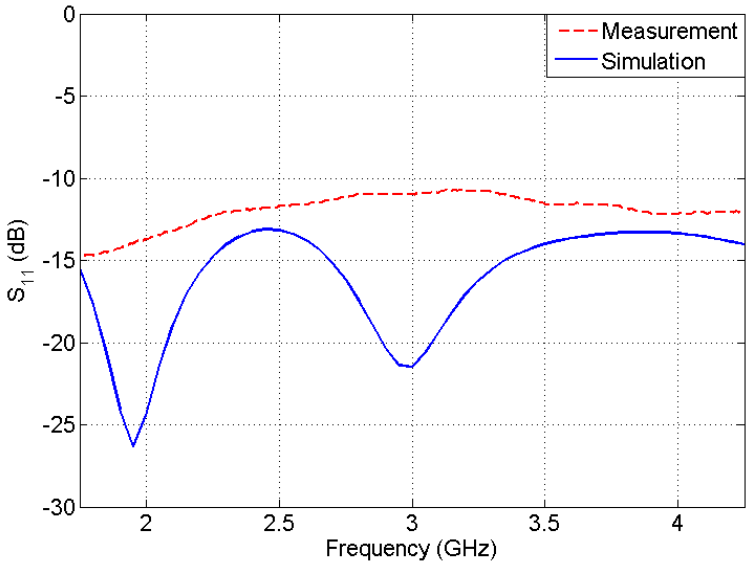

Figure 5.7. Simulated (blue, solid line) and measured (red, dashed line) return loss (S_{11}) of the embedded antenna. Simulations were carried out assuming realistic tissue properties, [83].

5.1.4 Finalized Prototype

The flexible circuit board was then integrated into the original system prototype, replacing the switching matrix, antenna array, and the antenna radome. In Fig. 5.8, photographs of the initial system prototype [78] and the newly designed system prototype are compared. Significant size reduction was achieved in this iteration by removing the electromechanical switch assembly and integrating the switching into the board. The two remaining RF cables were edge-launch instead of perpendicular to the board surface, which makes it possible to conceal them in a bra's fabric band/strap. We used plastic clasps and the additional drill holes in the folded region to pin the board in a specific shape around a hemispherical breast phantom.

To address the possibility of air-gaps (and thus unwanted interface reflections) due to an imperfect fit between the breast phantom (or breast) and the flexible PCB, a silicone gel (Ecoflex® Gel 00035, Sial) was used to act as a matching medium between the circuit

board and the breast phantom. The silicone gel (low-loss, with $\varepsilon_r = 6$ at 3 GHz) is a liquid that cures into an extremely soft gel; thus, it is possible to make an exact counter-mould to fill air-gaps between the breast phantom and the board. Unlike the ultrasound gel, the silicone gel does not remove many of the unwanted multi-path signals that may arise since it is a low-loss material. However, this material is only necessary in these initial tests of the flexible PCB. The final system will be in direct contact with the skin, and no matching medium would be necessary.

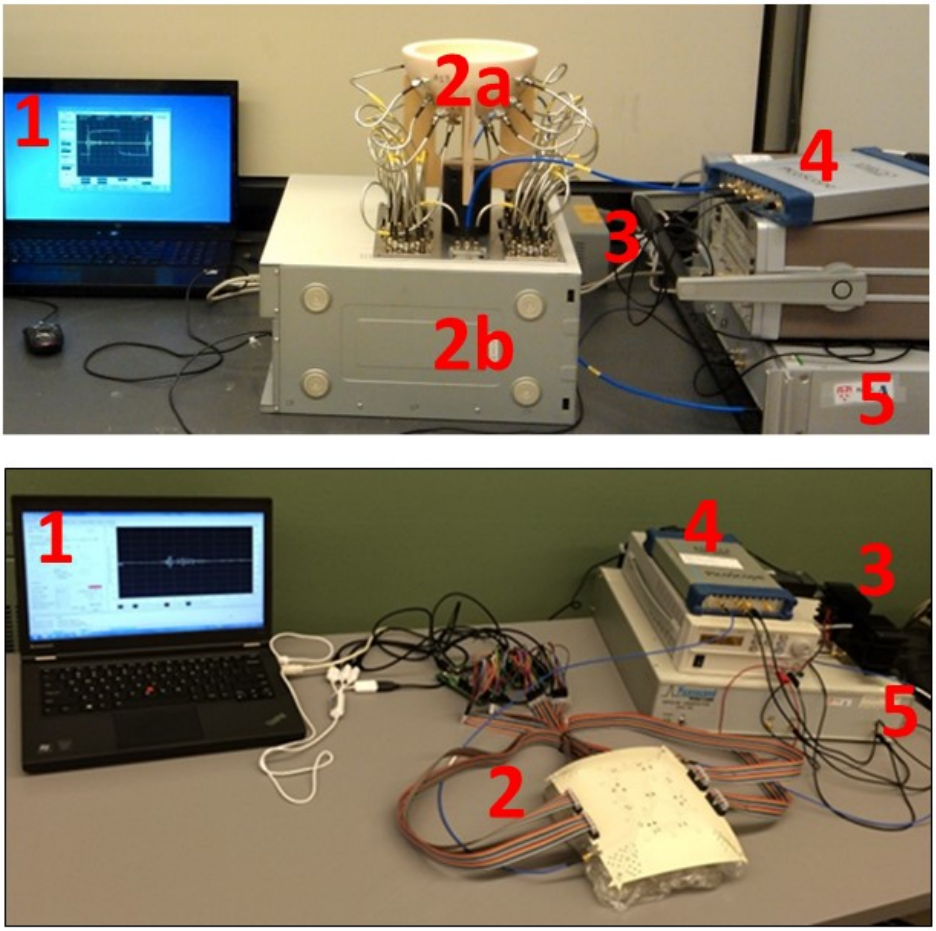

Figure 5.8. A comparison of the original system [78] (top) and the new system incorporating the new flexible circuit board (bottom) [83]. In the bottom image the board is flexed around a hemispherical breast phantom, held in place using plastic clasps. The system components are numbered as follows: 1) The operating PC for sending out control bits and saving the recorded time-domain data. (Top image) 2a) The radome and the 16 antennas, 2b) The switching matrix console. (Bottom image) 2) The new flexible circuit board containing the 16 antennas and the switching matrix and the two microcontrollers for logic control. 3) The pulse shaping circuitry. 4) The recording oscilloscope. 5) The impulse generator.

5.1.5 System Characterization and Results

This section is focused on presenting results of the newly developed system prototype. This includes measurements in regards to the insertion loss and the isolation, and a comparison of the data recorded from breast phantoms with both the new flexible prototype and the initial experimental system.

The total system loss for the newly fabricated circuit board was calculated based on the total path the RF signals travel along the board and the total number of switches and vias the signal passes through. As the loss for each of these components is frequency dependent, different frequency components of the signal will experience differing amounts of loss. Further, the design of the switching network is not perfectly symmetric, and different transmit-receive antenna pair connections required different lengths of microstrip trace along the circuit board. This resulted in clear-cut worst and best-case scenarios for the path loss and total system loss. Specifically, the total signal path length was 55 cm and 41 cm, for the worst and best-case scenarios, respectively. In Table 5.2, the loss associated with microstrip routing (Path Loss) and the total system loss (including switch insertion losses), for the worst and best-case scenarios, is presented for the three key frequency points in the range of operation for the system. These values are similar to those measured with the electromechanical switching matrix, which had a total system loss between 12 – 15 dB over the 2 – 4 GHz range.

TABLE 5.2. A COMPARISON OF THE WORST-CASE PATH LOSS AND TOTAL SYSTEM LOSS FOR TRAVEL ACROSS THE FLEXIBLE CIRCUIT BOARD FOR VARIOUS FREQUENCIES. THE BEST-CASE IS SHOWN IN PARENTHESIS [83].

Frequency	Path Loss (dB)	Total System Loss (dB)
2 GHz	6.02 (4.29)	11.62 (7.99)
3 GHz	8.56 (6.02)	15.39 (10.48)
4 GHz	10.69 (7.49)	18.55 (12.35)

The isolation of the switching matrix was measured for each channel of the switching matrix. The isolation for each channel is directly affected by the proximity of the microstrip traces for each channel. As the design of the switching matrix is based on a quadrant design, channels in the same quadrant have microstrip traces that are quite close together in comparison to those channels that are from different quadrants, thus the RF signal that is mutually coupled between the channels in the same quadrant is higher than those that are further apart. This leads to another 'best-case' and 'worst-case' scenario. The 'best-case' scenario here represents the channel with the best isolation (lowest mutual coupling), the 'worst-case' scenario represents the channel that has the transmit and receive RF traces the closest and has the worst isolation (highest mutual coupling). A comparison of the measured best- and worst-case isolation for the newly designed switching matrix is shown in Fig. 5.9. The worst-case scenario insertion loss is in line with the values quoted on the switch's data sheet (which quote a typical isolation figure of 36 dB), thus, demonstrating that the design does not significantly impact the cross-channel coupling. The concerns for cross-talk in this system are mitigated by the fact that this system is used as a monitoring application. As the cross-talk between channels will remain constant, as there will be no physical changes between the distance of the separate traces or any effects due to cable movement, the cross-talk between channels can be effectively filtered out in the differential signal; additionally, when implementing machine learning algorithms, this common signal will be ignored as it appears constant in all the recorded data.

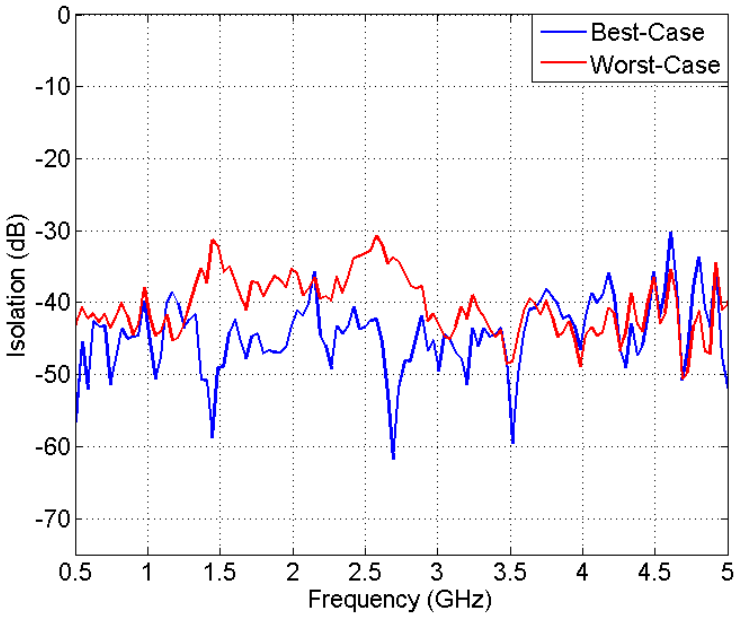

Figure 5.9. A comparison of the isolation of the newly designed switching matrix, for a 'best-case' and worst-case' scenario.

In this section, the data collected from the newly designed system prototype is compared to the data collected with the initial experimental system. For this analysis, the carbon-based rubber phantoms were used, as they represent a stable material to allow for a more direct comparison of the performance of the two systems. Data was obtained from two different hemispherical phantoms, each with a skin layer, and a plug to allow for healthy and tumour-bearing measurements. As before, a total of 240 signals per scan were recorded with an equivalent-time sampling oscilloscope operating at an effective sampling frequency of 200 GSa/s, with each signal representing the average of 16 successive recordings.

In Fig. 5.10, a comparison of the recorded time-domain signals for two nearest-neighbour antennas (antennas that are closest and located on the same side of the array), and for the two antennas at the maximum distance from each other (on opposite sides of the breast), for both systems testing a homogeneous breast phantom is shown. From this comparison, it is clear that, besides an inversion of the signal (due to the new antenna

orientation), the newly recorded signal is very similar to the previous system and demonstrates an increase in received power. The signal for the antennas furthest apart undergoes significant attenuation and distortion due to the dispersive and lossy nature of the breast tissue, making a direct comparison of the two recorded signals more difficult.

In Fig. 5.11, a comparison of the frequency content of the input pulse with the recorded signals after transmission through the breast phantom (for both nearest-neighbour and most distant antenna pairs) is shown, demonstrating that for various transmit-receive antenna pairs the new system maintains the frequency content of the input. Additionally, in Fig. 5.11, a comparison of the frequency content of the recorded signals between the original system prototype and the newly developed prototype is shown.

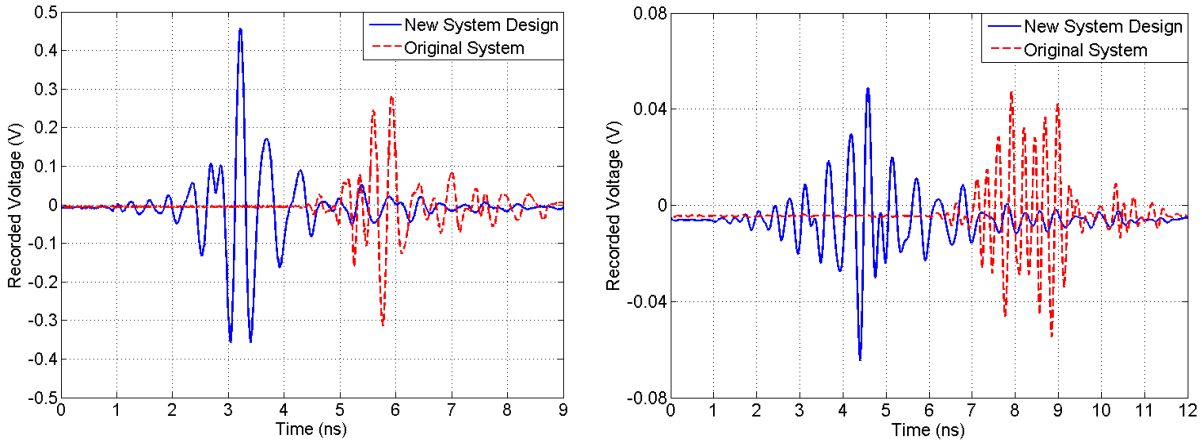

Figure 5.10. Comparison of the recorded signal after transmission through the breast for the new system design (blue) and the original system (red-dashed), [83]. (Left) A comparison for nearest-neighbour pair of antennas, and (Right) a comparison for antennas located furthest apart.

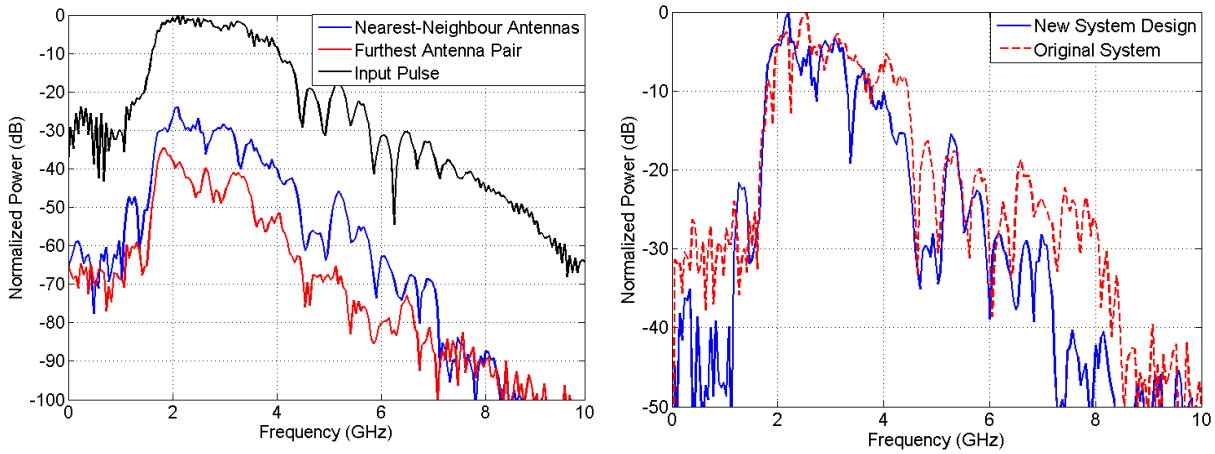

Figure 5.11. (Left) A comparison of the frequency content of the recorded signals for nearest-neighbour and furthest antenna pairs with the new system and with the input spectrum [83]. This plot demonstrates the fidelity of the system as the input spectrum is maintained after transmission through the system. (Right) A comparison of the frequency content of recorded signals using the new system and the original system.

The reconstructed 3-D images of the two breast phantoms, created with the data recorded from both the new, flexible system prototype and the original system, is used as a final comparison. As with the previous analysis, the differential data set is used to create the 3-D reconstruction images (two scans for each phantom are done, one with the healthy plug and one with the tumour-bearing plug). The differential data set is then used with the DMAS algorithm to create the 3-D reconstruction images.

In Fig. 5.12, 2-D coronal slice images, taken at the depth that contains the highest pixel intensity across the image, are compared for both systems and both phantoms. These two phantoms, hereafter referred to as Phantom 1 and Phantom 2, were fabricated to represent a high-adipose content breast with an average relative permittivity of 7 and 10, respectively. The reconstructed images for Phantom 1 are shown in (A) and (B) for the original and the new system, respectively. The images for Phantom 2 are shown in (C) and (D) for the original and new system, respectively. Both systems are able to correctly identify the presence of the tumour, whose correct location is denoted in the images by a white circle.

In Table 5.3, the tumour localization error and the Signal-to-Clutter Ratio (SCR), as defined in Chapter 3, are used as quantifiable metrics to demonstrate that the imaging results with the newly developed system are comparable to the original system.

These results demonstrate the successful implementation of a flexible multilayer circuit board to replace three distinct components of our initial system prototype; the switching matrix, which had been implemented with electromechanical switches, the antenna array, and the ceramic antenna-housing radome. These changes represent a cost savings of almost $20 000.

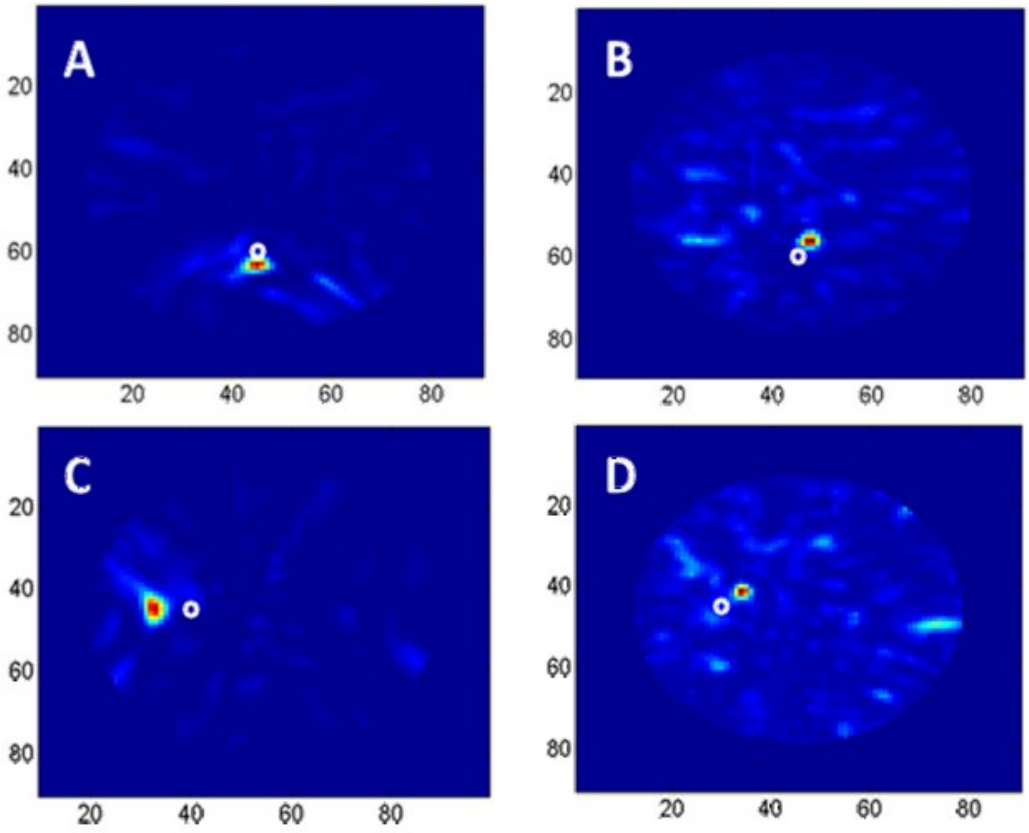

Figure 5.12. A comparison of a coronal-slice through the *xy* plane of the reconstructed images for two stable rubber breast phantoms when using the original system and the new system implement the flexible circuit design [83]. We chose the slice that contained the highest electromagnetic scatterer, in this case the tumour. The imaging results for Phantom 1 are shown in (A) and (B), for the original and new systems, respectively. The imaging results for Phantom 2 are shown in (C) and (D), for the original and new systems, respectively. The true location of the tumour is indicated by the white oval. The x and y axis are in mm.

TABLE 5.3. COMPARISON OF TUMOUR DETECTION METRICS FOR THE ORIGINAL AND NEW SYSTEM [83]

	True Tumour Location (x,y,z) mm	Localization Error (mm)		SCR (dB)	
		Original	New	Original	New
Phantom 1	(45,60,10)	5.83	6.16	4.67	8.17
Phantom 2	(30,45,10)	8.06	6.00	7.96	5.85

5.2 Development of a 2nd Generation Flexible Prototype

5.2.1 Motivation

One of the primary concerns arising from the testing of the initial design of the flexible circuit board was in regards to the overall flexibility of the circuit and the number of logic control lines required. After metallization, and due to the size and arrangement of the antennas in the array, the board was not as flexible as desired, and could not be bent sufficiently in multiple planes to allow for the board to be conformed to the human breast geometry.

The design of the second generation of the flexible circuit board was focused on three main aspects to improve the flexibility and performance of the board: first, using a more flexible dielectric substrate, second, using different switches to reduce the number of control lines and reduce the number of metallization layers, and, lastly, using a new, smaller antenna along with a newly designed antenna array layout.

5.2.2 Design Parameters and Constraints

The first design choice was to choose a more flexible dielectric substrate for the PCB to be fabricated with. Based on PCB manufacturer's recommendations (more flexible, easier to work with), the DuPont Pyralux AP 8545 ($\varepsilon_r = 3.25$, $\tan \delta = 0.0028$) material was chosen as the dielectric substrate; the DuPont Pyralux FR Bondply0111 ($\varepsilon_r = 3.12$, $\tan \delta = 0.022$) material was chosen to be used as the binding agent between layers. The drawback of using this new substrate was a slightly higher loss tangent ($\tan \delta = 0.0028$ for the Pyralux, compared to $\tan \delta = 0.0025$ for the UltraLAM material from the first-generation prototype). The higher loss tangent of the substrate material would cause increased attenuation for the signals being carried on the microstrip traces on the board. This drawback was mitigated by reducing the overall size of the design, leading to shorter path lengths on the board.

The next design choice was to identify an appropriate alternative to the solid-state switches used previously. The new switches would ideally require less control bits; as the switches used in the initial flexible prototype were passive, they required 2 bits and 4 bits, respectively, for the SPDT (single-pole, double-throw) and SP4T (single-pole, four-throw) switches. Additionally, the switches should have relatively linear insertion loss over the 2 - 4 GHz range, to match the frequency range of operation for the system. With these design constraints, the SKY13384-350LF and the SKY13286-359LF switches, which feature an on-chip decoder, were chosen. By implementing these switches in the design, the number of DC logic control lines were reduced from 72 to 36, allowing the PCB to be easily controlled by a single microcontroller. Additionally, as these switches can be operated at very low power (in total all 18 switches require 3.2 mA at 5 V VDD), they can all be powered by the same individual microcontroller.

Another design decision to help improve the overall flexibility of the system was to reduce the number of metalized layers from six to four. With the reduction of the number of control lines, and the minimization of the 'duck-under' signals, it was now possible to remove some of the unnecessary bottom metalized layers from the initial design. In Fig. 5.13, the new design of the layer stack-up, with the different substrate thicknesses and the four metallization layers, is shown.

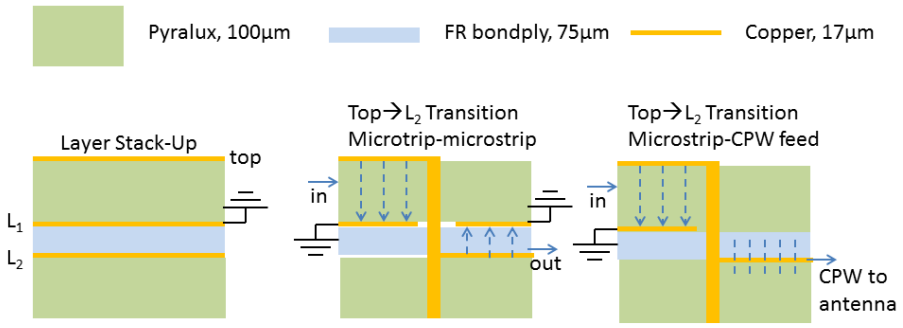

Figure 5.13 Layer stack-up of the proposed new design (left), including side-views for the microstrip-to-inverted-microstrip transition (middle) and microstrip-to-CPW-feedline (right) transition [111]. Not shown is the metallization layer for the DC routing (simple copper traces).

With these changes to the substrate materials and thicknesses, it was necessary to re-optimize the trace widths to minimize the loss and to have a characteristic impedance of 50 Ω on the transmission line. This optimization was done through a parametric analysis with HFSS. The optimal values for the microstrip traces were found to be 0.26 mm and 0.20 mm wide, for the Top and L_2 layers, respectively. This is in comparison to the 0.28 mm and 0.27 mm wide traces for the Top and L_2 traces, respectively, in the previous design. The path loss for each of the microstrip traces is summarized in Table 5.4. As expected, the higher loss tangent leads to an increase in the path loss for the microstrip traces embedded in the PCB (L_2 layer traces) as compared to the initial flexible PCB design. The difference in the path loss for the Top layer microstrip is negligible.

TABLE 5.4. MICROSTRIP PATH LOSS AT THREE KEY FREQUENCIES, ON DIFFERENT ROUTING LAYERS

Microstrip Path loss (dB/cm)	Frequency		
	2 GHz	3 GHz	4 GHz
Top Layer	0.099	0.139	0.171
L_2 Layer	0.241	0.333	0.435

In [88], a compact, coplanar waveguide (CPW) fed, flexible rectangular patch monopole antenna for on-body operation in the 2 – 4 GHz range was designed. The antenna was designed with a smaller footprint (20 mm x 20 mm, including the feed-line) than the elliptical monopole patch antenna (32 mm x 24 mm, including the feed line) used in the first design of the flexible PCB. The antenna is a broadside antenna with a wide radiation beamwidth so that it can illuminate a large region of the breast. The antenna was designed to be on a single layer of the DuPont Pyralux substrate and in direct contact with the skin; thus, it was necessary to modify the antenna for operation when embedded in a multi-layer PCB. The antenna and the microstrip-to-CPW transition were optimized for the new board design (where the antenna is not in direct contact with the skin – due to the other circuit board layers) to achieve S_{11} below -10 dB and port impedance of 50 Ω over the frequency range of interest. These simulations were done with a layer of skin (thickness of 2.5 mm, relative permittivity $\varepsilon_r = 40$, electrical conductivity $\sigma = 2$ S/m) and a layer of fat (thickness of 80 mm, $\varepsilon_r = 10$ and $\sigma = 0.4$ S/m) placed in contact with the bottom layer of the board.

An image of the optimized antenna is shown in Fig. 5.14. The complete dimensions of the antenna can be found in [88]. The optimization procedure required changes to the feed width, 'A', and the feed gap, 'A_1', to 0.75 mm and 0.4 mm, respectively (from 0.9

mm and 0.5 mm, respectively). The S_{11} for the embedded antenna is also shown in Fig. 5.14, confirming the low return loss over the frequency range of interest.

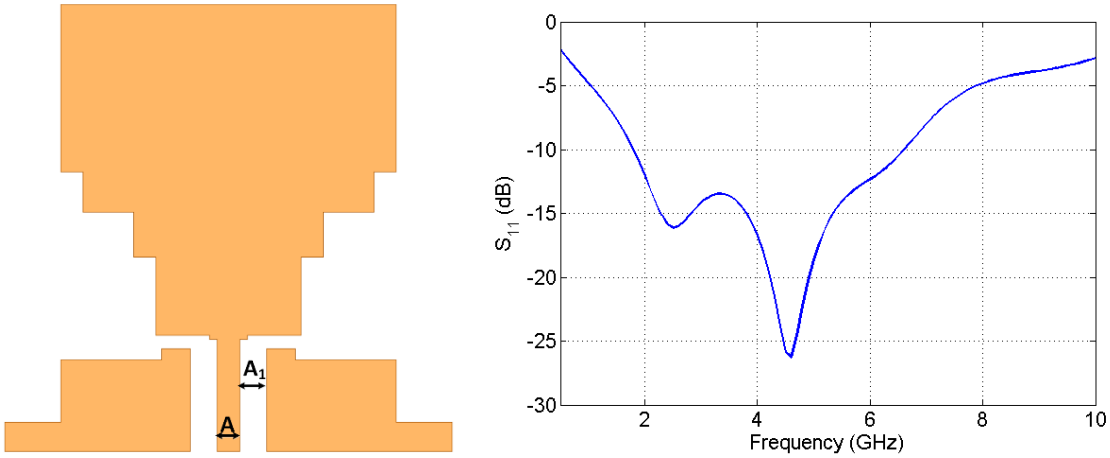

Figure 5.14. (Left) An image of the antenna adapted from [88]. For integration with our circuit board we have changed the feed width A, and the feed gap A_1, as shown in the image. The remaining dimensions can be found in [88]. (Right) Simulated return loss (S_{11}) for the embedded antenna when the circuit board is in contact with realistic tissues (skin and fat layer) [111].

The smaller footprint associated with these new antennas allowed for the re-design of the antenna array to improve the flexibility of the circuit board. This second-generation flexible circuit board was designed to integrate with our clinically tested system that can be worn by the patient, akin to a bra [76]. Hence, the desire to create an array that can be conformal to a breast like shape and fit into a bra structure. The first step in the re-design of the antenna array was to determine a region to restrict the antennas. This decision was based, once again, on a quadrant design that would feature more aggressive 'cuts' made into the board (creating something similar to a cross-structure); ultimately, these large cut-out regions would allow for improved flexibility, as there will be less material. The concept of this design is shown in Fig. 5.15. To test the flexibility of this concept, two stacked layers of metallized Pyralux substrate were glued together (to mimic

the thickness and flexibility of the final circuit) and then cut into the proposed shape of the second-generation prototype, and placed it on the torso of a mannequin. This suggests that the flexibility of the new circuit board should be adequate to conform to the breast as desired.

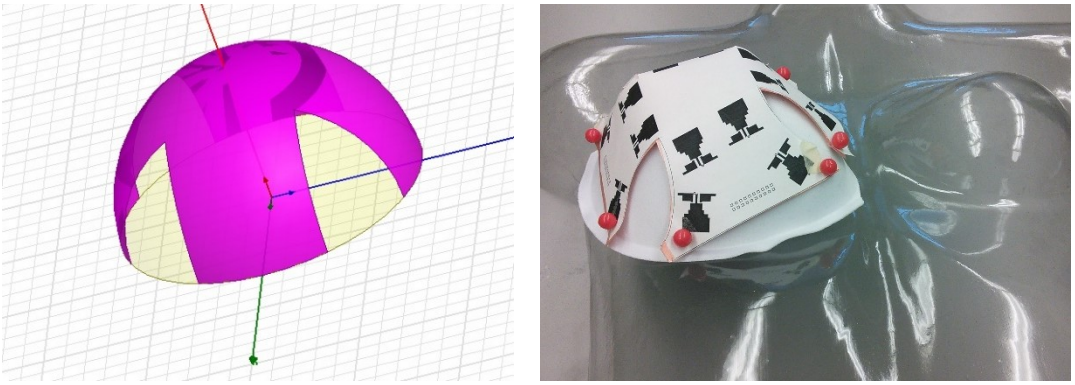

Figure 5.15. (Left) Concept of the design for the second-generation flexible circuit board, conforming to a hemispherical structure. The highlighted purple region represents the region that the antenna array, and electronics) would be limited to. (Right) Testing of the concept with the metallized Pyralux stack, with a sample antenna array with 16 antennas, conforming to the shape of a mannequin.

5.2.3 Antenna Array Design

One of the primary aims of this study was to determine whether a specific antenna array layout would lead to improved results. Recently, in [112], it was found that spiral and random array configurations produce higher resolution images compared to regularly spaced arrays. However, this work focused solely only the use of a planar antenna array, placed over a breast phantom. In [41], several simulation scenarios were conducted with MRI-derived breast phantoms in order to determine whether cylindrical, spherical, or patient-specific (set distance from the skin) antenna arrays would lead to the best results. This work found that the spherical and patient specific arrays outperformed the cylindrical array. However, this work focused solely on monostatic data. The optimization

of the array for the 2nd generation prototype required a layout for a bistatic array conformal to the breast surface.

The antenna array design was optimized through HFSS simulations. Limitations on the potential antenna locations for the array were defined based on the proposed design of the flexible circuit board, as shown in Fig. 5.15. The antenna used was the optimized rectangular patch antenna defined in Section 5.2.2. The antennas were placed exactly as they would be in the experimental scenario, with the layer stack up defined in Fig. 5.13. The choice of the potential antenna arrays was then limited to three potential options:

- a regularly spaced 'cross' design, similar to the initial experimental prototype from Chapter 3 [63] – [75];
- a spherical based array, divided into two equal rings;
- an irregularly distributed asymmetrical array.

The array configurations were selected to have a wide range of spatial coverage in terms of antenna positions and spatial diversity in the propagation paths of the reflected signals inside the breast. Each array was tested with 16 antennas. The performance of the different arrays was assessed based on the quality of images generated from simulations with numerical breast phantoms. An example of each array type is shown in Fig. 5.16.

Data for each of the three antenna arrays was collected from two hemi-spherical numerical breast phantoms. Phantom A represented a simple test case: the breast interior was entirely homogeneous, made up of adipose tissue, with a 2-mm thick skin layer. Phantom B represented a more challenging and realistic environment: the breast interior was composed of 50%, by volume, of glandular structures, arranged as cones originating from the nipple. Images were created using the DMAS algorithm with a differential data set. For the tumour bearing measurements, a 5-mm radius tumour was inserted into the numerical phantom. The properties of the various tissues were modelled based on the Debye properties defined in [9]. From the HFSS simulations, the mutual S-parameters

(S_{xy}), for each antenna pair, were obtained. This data represents the channel response of all possible channels in the system (for the 240 antenna pairs for the system, 240 mutual S-parameters were extracted). The channel response was then convolved with the band-limited (2 – 4 GHz) experimental pulse, to provide a more accurate representation of the experimental results.

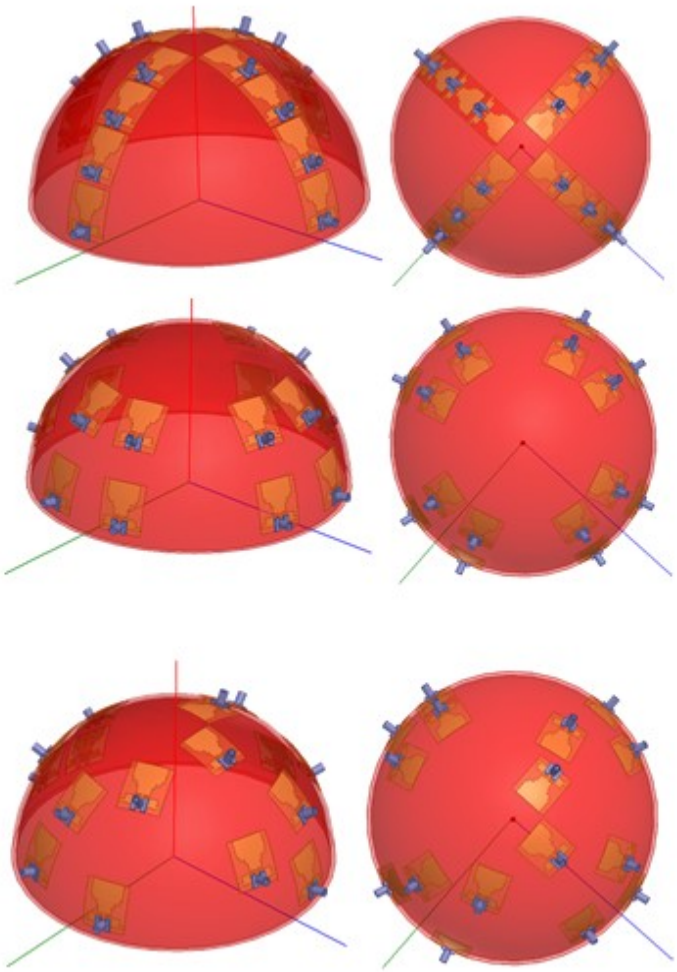

Figure 5.16. Schematic drawings of the three different types of arrays assessed. (Top) Regularly spaced cross array, (Middle) spherical ring array, (Bottom) irregularly spaced asymmetrical array.

The images from all three array configurations successfully localize the inserted tumour in the homogeneous Phantom A model. In Fig. 5.17, the 2-D the coronal and axial slice images for Phantom B are compared in both the *yz* and the *xy* planes for the three different arrays tested. From visual inspection of the images, it is clear that the spherical ring array and the irregular asymmetrical array are able to correctly identify and localize the presence of a tumour, even in the heterogeneous breast phantom.

In Table 5.5, the localization error and the Signal-to-Clutter Ratio (SCR) are used as quantifiable metrics to compare the quality of the image results for the three different arrays tested. From a combination of these metrics, and a visual inspection of the images, it is clear that the spherical ring array results in the best performance, for the tumour locations tested here. This result also agrees with [41].

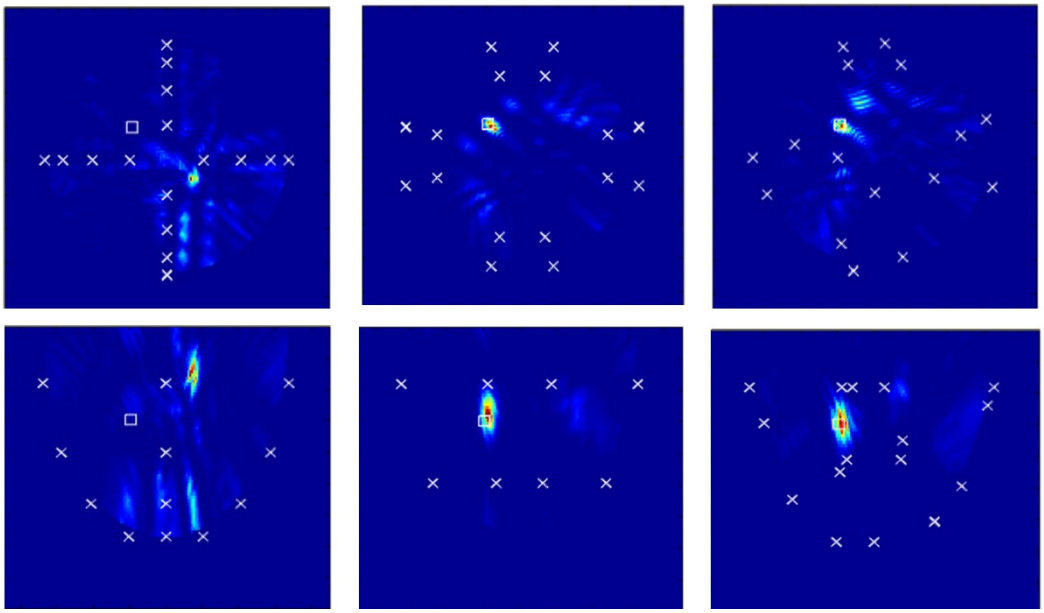

Figure 5.17. The reconstruction images for the data collected from Phantom B for the three different array types: (Left) regularly spaced cross array, (Middle) spherical ring array, (Right) irregular asymmetrical array. The top set of images show the *xy* cross-section at the location of the maximum intensity EM scatterer. z = 30 mm. The bottom set of images show the *xy* cross-section at the location of the maximum intensity EM scatterer, x = 19 mm. The "x" markers represent the positions of the antennas and the white square marks the actual location of the tumor center.

TABLE 5.5. A COMPARISON OF THE IMAGE QUALITY METRICS FOR THE THREE DIFFERENT ARRAY TYPES FOR THE HETEROGENEOUS NUMERICAL BREAST PHANTOM

Array Type	Localization Error (mm)	SCR (dB)
Regular Cross	46.74	N/A
Spherical Ring	2.45	5.69
Irregular Asymmetrical	2.45	3.98

5.2.4 2nd Generation Flexible Prototype Design

The completed layout design of the second-generation flexible circuit board, including antennas, electronics, the common ground layer, and DC and RF traces, is shown in Fig. 5.18. The functionality of the switching matrix is identical to the first-generation prototype as described in Section 5.1.2. With the reduction in size of the antennas, fewer DC control lines, and the redesigned antenna array, the overall size of the PCB has decreased from 20 x 21 cm to 18 x 18 cm; representing a closer fit to a 'C' cup sized bra.

The total system loss for the second-generation prototype was calculated and is shown in Table 5.6. The loss associated with microstrip routing (Path Loss) and the total system loss (including switch insertion losses), for the worst and best-case scenarios, is presented for the three key frequency points in the range of operation for the system. Despite the increased loss per unit length for the new circuit board (due to the higher loss tangent of the substrate), the total system loss is almost identical to the first-generation circuit board; due primarily to the reduction in the overall size of the board and the optimized antenna array layout. Additionally, by rotating the antennas in the bottom ring by 180°, the new design is more symmetric than the first-generation circuit board; thus, the overall path length for each channel is much more alike and the major differences in path loss arise from the number of vias on a particular channel, not path length differences.

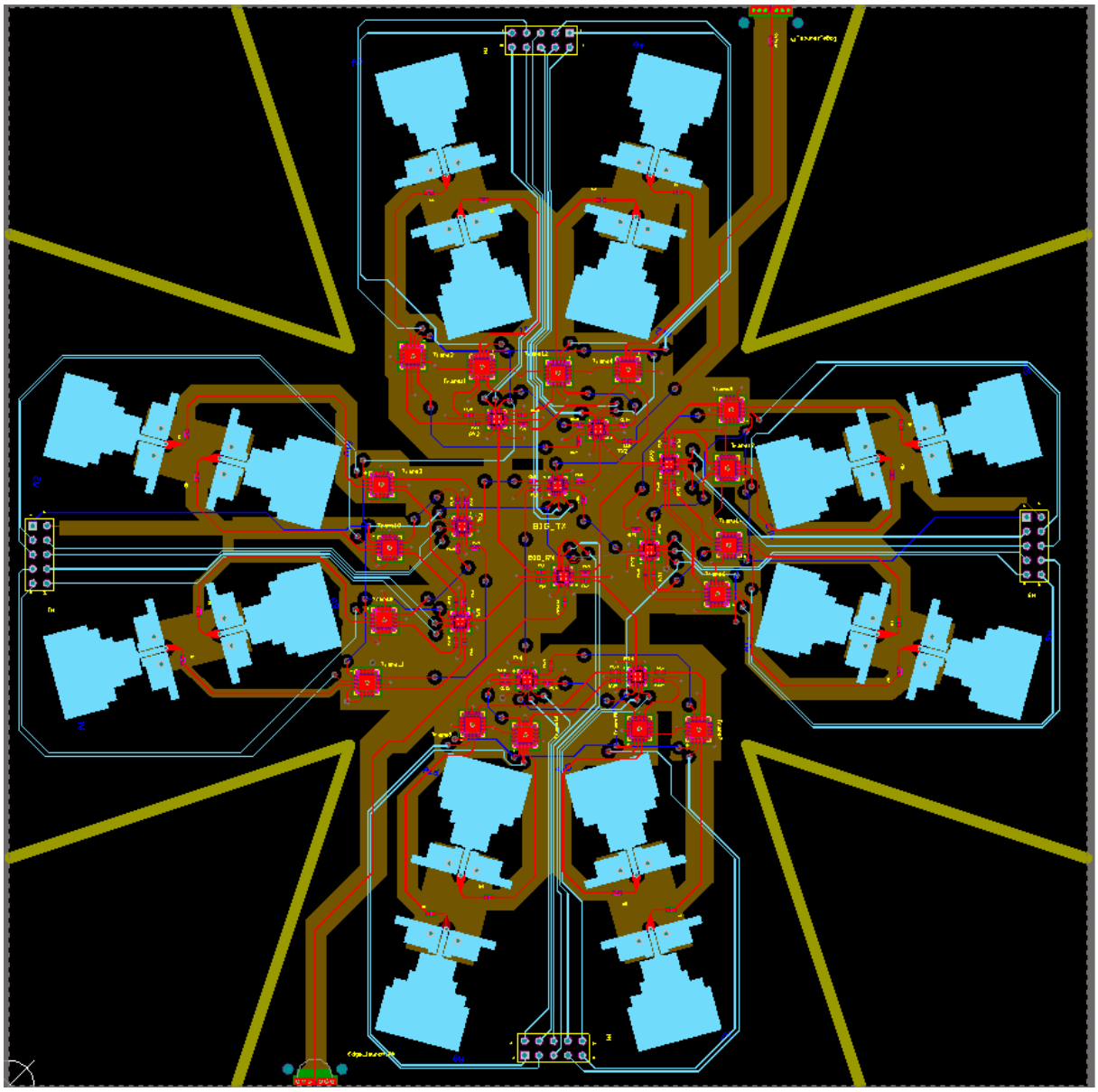

Figure 5.18 Layout illustration of the second-generation flexible circuit board, designed with Altium Designer. The 16 rectangular patch antennas and the DC control lines are shown in cyan. The top layer RF traces, and soldered electronics are shown in red. The power carrying traces, and the duck-under RF traces, are shown in dark blue. The thick yellow lines represent the 'cut-out' regions that are void of electronics or traces. These regions will be cutout from the final design, allowing for improved flexibility. The common ground layer for the microstrip traces is shown in gold.

TABLE 5.6. A COMPARISON OF THE WORST-CASE PATH LOSS AND TOTAL SYSTEM LOSS FOR TRAVEL ACROSS THE 2ND GENERATION FLEXIBLE CIRCUIT BOARD FOR VARIOUS FREQUENCIES. THE BEST-CASE IS SHOWN IN PARENTHESIS.

Frequency	Path Loss (dB)	Total System Loss (dB)
2 GHz	5.13 (3.57)	11.22 (7.77)
3 GHz	7.17 (5.02)	14.20 (9.63)
4 GHz	8.95 (6.17)	18.16 (12.38)

5.3 Hardware Optimization

This section is focused on recent developments aimed at identifying, testing, and integrating discrete hardware components to replace the remaining generic, expensive and bulky system components. As discussed in Chapter 3, the switching, pulse generation, timing, and data recording aspects of the system represents the vast majority of the system cost. The previous sections of this chapter have discussed how a custom-built circuit board can replace the switching matrix and antenna array portions of a system. This section begins with a discussion on the testing and implementation of low-cost off-the-shelf components for the pulse generation and timing (clock generation) aspects of the system. Following this discussion, an equivalent-time sampling circuit to replace the high speed oscilloscope is proposed and tested. Finally, this section concludes with an overview of the hardware changes presented in this Chapter, and compares the cost of the new system prototype that incorporates custom-built components, with the cost of the initial experimental system presented in Chapter 3.

5.3.1 Pulse Generation and Timing

The timing aspects of the system are governed by a clock generator. The clock generator is used to trigger the pulse generator and the high speed oscilloscope in the system. As the system uses an equivalent-time sampling oscilloscope, and averages out

the data over several periods to reduce the noise, a low-jitter source is necessary. Additionally, the pulse generation aspect of the system requires a sharp rising, or falling, edge to create the desired pulse shape.

The Silicon Labs Si5351 was identified as a possible replacement for the Tektronix gigaBERT1400 that is currently used in the system for clock generation. The gigaBERT 1400 is an expensive, bench-top clock generator that has a multitude of functionalities for system testing in a laboratory setting. The Si5351 is an IC (integrated circuit) chip that can generate three independent square wave outputs with repetition rates between 1 kHz and 150 MHz; the current operation of the system is at 25 MHz. The Adafruit Si5351 Development Board [113] allows for the easy testing and integration of the Si5351 component. The development board has dimensions of 3 cm by 2.1 cm and an approximate cost of $10, making it a suitable replacement. In Fig. 5.19, three different output waveforms, at 3 kHz, 25 MHz, and 160 MHz, from the Adafruit clock generator are presented, demonstrating the functionality of the component. At 160 MHz, which is outside the recommended operating range of the device, the output is no longer a high-quality square wave. The data was recorded with the sampling Picoscope.

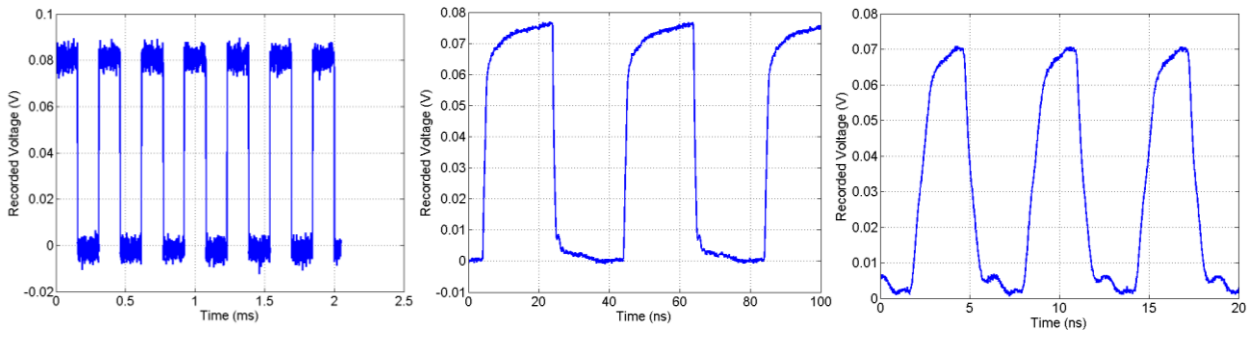

Figure 5.19. Output of the Adafruit clock generator. Square wave outputs at (Left) 3 kHz, (Middle) 25 MHz, and (Right) 160 MHz repetition rates.

The output of the clock generator is used to both trigger the oscilloscope and create the required pulse for the system. The Picosecond impulse generator requires a sharp edge to create the 70 ps FWHM quasi-Lorentzian impulses that are used to drive the system. Operating at 25 MHz, the output of the signal from the gigaBERT1400 has a rise time of approximately 150 ps, whereas the rise time of the Adafruit generated clock signal is approximately 900 ps. The specifications of the Picosecond impulse generator state that a rise time of 1 ns is required. Additionally, the Picoscope requires a trigger with a rise time of 1 ns. To test whether the Adafruit is a viable alternative to the gigaBERT1400, the two clocks, both operating at 25 MHz, were used to trigger both the impulse generator and the Picoscope. The pulses generated from the impulse generator were then passed through the SBR pulse-shaper (refocusing the spectral content of the pulse into the 2 – 4 GHz range) and recorded with the Picoscope. A comparison of the two recorded pulses is shown in Fig. 5.20. From this plot it is clear that the Adafruit clock generator offers a viable low-cost solution to replace the gigaBERT1400, as the resulting pulses after the SBR, which represents the signal sent to the antennas for transmission, are nearly identical. Furthermore, an analysis of the jitter of the two clocks, when operating at 25 MHz was performed. The recorded jitter for the gigaBERT1400 was found to be 21.2 ps, whereas the jitter for the Adafruit clock was found to be 24 ps. This difference of less than 3 ps is a fraction of the time between samples.

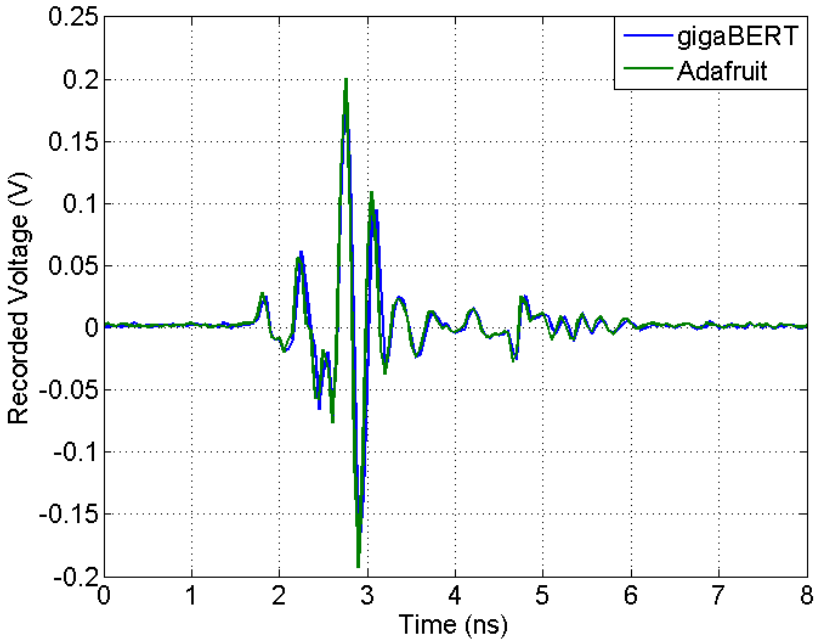

Figure 5.20. Comparison of the pulse recorded, after the reshaping process, when using the two clock generation options for driving both the impulse generator and the Picoscope.

The pulse generation aspect of the system can be quickly summarized as follows; the Picosecond impulse generator is triggered by a clock source and creates 70 ps FWHM quasi-Lorentzian pulses at the same repetition rate of the source. These pulses are reshaped by the SBR to have the majority of the spectral content in the 2 – 4 GHz range. It is necessary for the pulses generated from the pulse generator to have frequency content up to at least 4 GHz, thus setting requirements on the width of the pulses generated.

The Furaxa Sampulse development board [114] was identified as a component to reduce the Picosecond impulse generator at a fraction of the cost, $5 000 CAD, and size, 10 cm by 6 cm, of the device. The Furaxa board is based on a proprietary CMOS IC that generates very narrow pulses based on the falling edge of an input clock signal. An example of the output of pulse from the Furaxa Sampulse board is shown in Fig. 5.21. The pulse generated is a 120 ps FWHM differentiated Gaussian pulse. The pulse was recorded with the Picoscope.

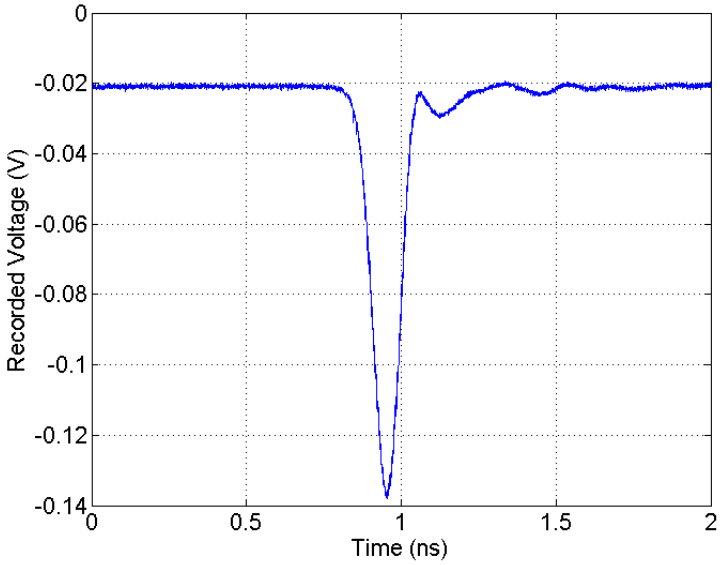

Figure 5.21. Example of the pulse generated from the Furaxa Sampulse board.

The combination of the Adafruit development board and the Furaxa Sampulse board represent a miniaturization of the pulse generation and clock generation aspects of the system. A photograph of the two components, with a ruler for scale, is shown in Fig. 5.22. These two new components can be easily integrated into the system prototype by directly replacing the Tektronix gigaBERT1400 and the Picosecond impulse generator. The functionality of this new miniaturized system is tested with a breast phantom. A comparison of the signals recorded after transmission through the breast phantoms for the new miniaturized system and the original system, as well as the frequency content of the recorded signal, is shown in Fig. 5.23. From these plots, it is clear that these components can be used to replace the bulky components from the original system and to help develop a compact and low-cost system prototype.

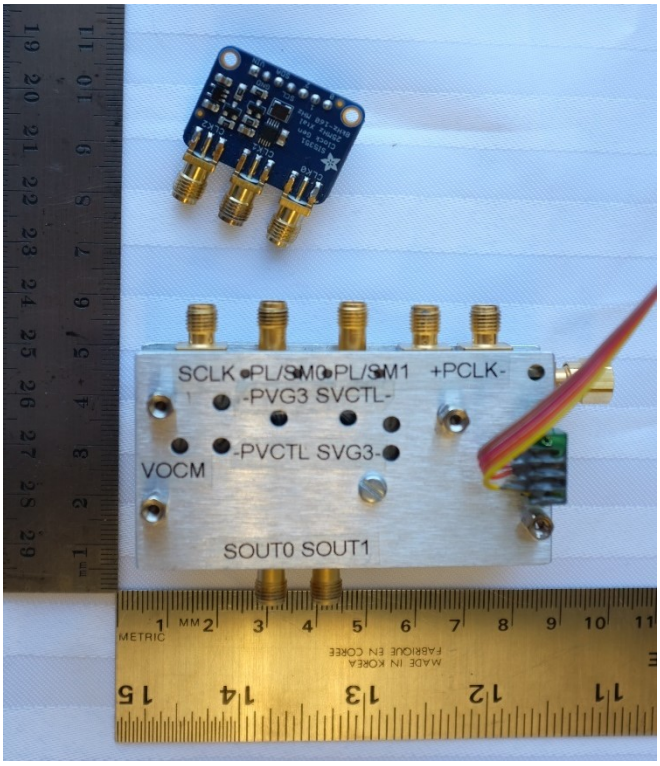

Figure 5.22. Photograph of the (Top, blue board) Adafruit development board and the (Bottom) Furaxa Sampulse development board, placed near a ruler for scale [115].

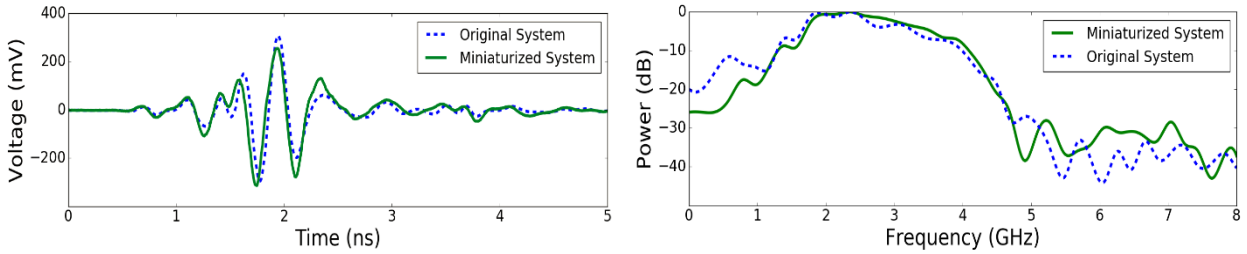

Figure 5.23. Testing the integration of the new components, Adafruit board and the Furaxa Sampulse, into the experimental system. (Left) A comparison of the signal recorded after transmission through a breast phantom for the original system and the miniaturized system. (Right) The spectrum of the recorded signal [115].

5.3.2 Equivalent-Time Sampling Circuit

Recently, the group at Chalmers University of Technology in Sweden has begun to modify their existing TD system to reduce the overall associated cost [52]. The first step they have investigated is to replace the high-speed sampling oscilloscope with inexpensive, discrete off-the-shelf components. Specifically, in [52] an outline is provided on how a track-hold amplifier (T/H), an analog-to-digital converter (ADC), and a field programmable array (FPGA) can be used in conjunction to replace the oscilloscope at a fraction of the cost (less than one-tenth the cost). The T/H amplifier is required to increase the effective sampling rate of the ADC. This minimizes the required sampling rate of the ADC, reducing the cost as high speed ADCs can quickly increase the overall cost of the system. Additionally, by designing the receiving module to make use of time-equivalent sampling, it is possible to operate the circuit at an equivalent sampling rate that can meet the high-speeds demands of a microwave system. The circuit proposed in [52] was integrated into an experimental TD system and was successfully tested, demonstrating that the circuit can be used to replace a high-speed oscilloscope.

The circuit design in [52] was used as the basis for the development of an equivalent-time sampling circuit to replace the Picoscope in the system prototype developed in this thesis. In an effort to further reduce the cost of the system, a STM32F4 Discovery Microcontroller Unit (MCU) is used to replace the FPGA in the proposed equivalent-time sampling circuit. The MCU is used to read the output pins of the ADC, convert the binary 14-bit word to a hex value, and then send the data to the PC. A block schematic of the proposed circuit is shown in Fig. 5.24. The list for the components is given as follows:

- Texas Instrument ADS4149 Analog-to-Digital Converter (ADC)
- STM32F4 Discovery Microcontroller Unit (MCU)
- Analog Devices AD9959 Direct-Digital Synthesizer (DDS)
- Hittite Microwave HMC661LC4B Track-and-Hold (T/H)

In order to control the equivalent-time sampling rate, it is necessary to create a difference in the sampling rate of the ADC and the pulse repetition rate; this creates a sequential delay that can be fine-tuned [52]. This process is illustrated in Fig. 5.24 by the separate clocks controlling pulse generator and the ADC. A photograph of the finalized circuit for testing is shown in Fig. 5.25.

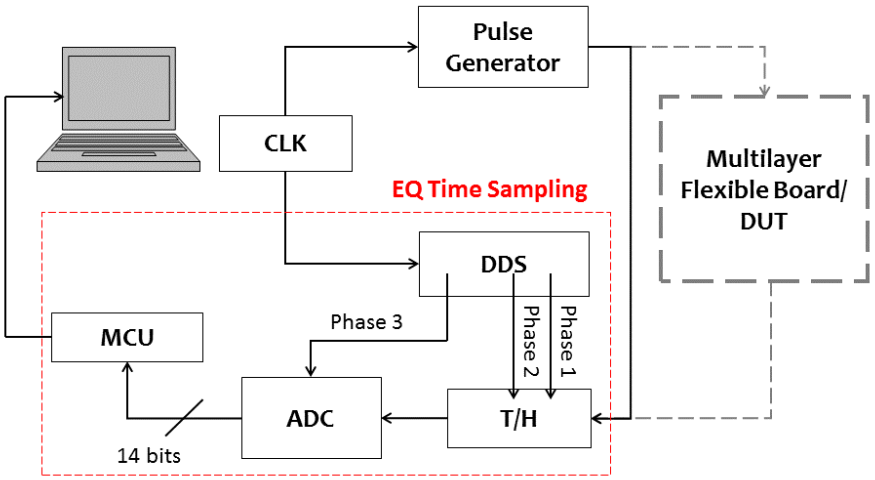

Figure 5.24. A block schematic of the low-cost receiving module implemented in our system. This design is based on the conclusions from [52].

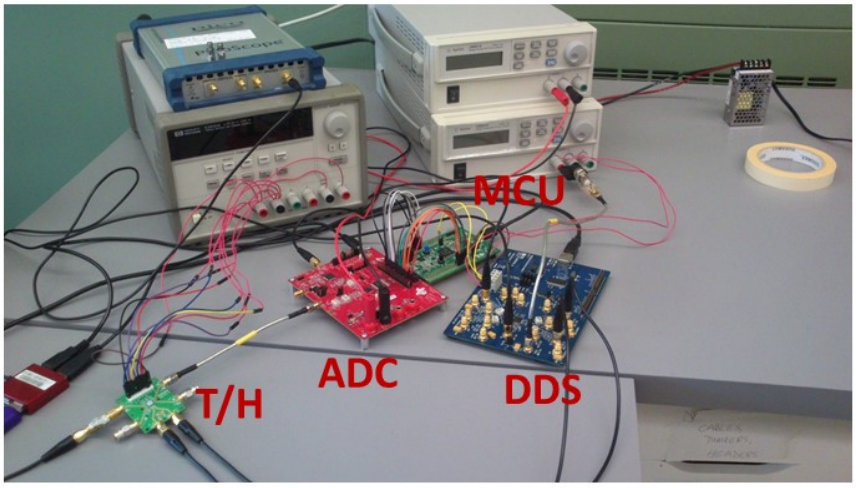

Figure 5.25. A photograph of the implemented equivalent-time sampling circuit; design based on the conclusions from [52].

One of the primary concerns when implementing the equivalent-time sampling circuit with the use of the T/H is to ensure that the ADC is sampling the input signal during the 'hold' phase of the T/H. In order to ensure that the ADC is properly timed, it is necessary to compensate for the different channel delays that can occur between the different phases of the T/H, the triggering of the ADC, and the sampling of data. More specifically, these delays are: the aperture delay of the ADC (t_A), the delay associated with different cable lengths ($t_{RG\text{-}delay}$), the settling time of the T/H output ($t_{SF\text{-}delay}$), and the clock-to-hold (t_{co}) and hold-to-output (t_{ho}) delays of the T/H. These delays are summarised in Fig. 5.26.

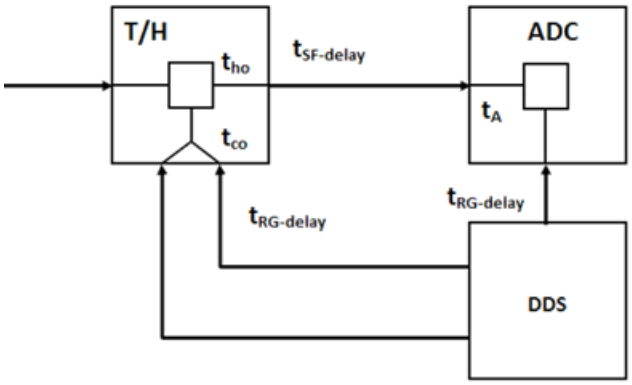

Figure 5.26. An example of the different delays in the equivalent-time sampling circuit, and where in the circuit they occur.

The equivalent-time sampling circuit was first tested with simple sine wave inputs. These simple tests were necessary to first identify the phase offset between the T/H and ADC triggers that ensure the data is being sampled during the hold phase of the T/H and to demonstrate the successful reconstruction of the data sampled by the MCU from the ADC output.

The system was tested with a 25 MHz sine wave input. The choice of a 25 MHz repetition rate is used as this is the repetition rate that the system prototype operates at. The aim of this experiment is to demonstrate that this circuit can be used to obtain an

equivalent sampling rate that far exceeds the 250MSPS of the ADC; by operating the ADC at a 24.947 MSPS an equivalent-time sampling rate of 10 GSa/s can be achieved. A comparison of the ADC output when the phase delays are and are not accounted for is shown in Fig. 5.27. These plots, which show the sample points recorded in blue, and the linearly interpolated signal in green, confirm the necessity for a properly timed ADC for the successful implementation of the equivalent-time sampling circuit. When the phase offset is not accounted for, the ADC is not sampling the T/H at the correct time, thus it is not obtaining the next point on the sine wave, thus the reconstruction is unsuccessful. When the phase offset is successfully accounted for, the reconstruction of the sine wave is exact and the spacing between points is 100 ps. The phase offset between the clock inputs of the ADC and the T/H that leads to the successful reconstruction of the sine wave at 10 GSa/s was found to be 8.5°.

The equivalent-time sampling circuit was then tested with more complex input signals. To minimize the effects of random noise on the reconstructed signal a simple averaging procedure was implemented: a stream of data, representing a snapshot of time that is $N_{averages} \times Period$ in length, is recorded, where $N_{averages}$ is the number of desired averages. The recorded data is then divided into $N_{averages}$ sections, that each represent one period of time. The averaged signal is then obtained by taking the average at each sample across the $N_{averages}$ sections. As with the operation of the Picoscope, there is a direct trade-off between the noise floor of the recording, the time to record the data and the number of averages. For this set of experiments, the number of averages is set to 16.

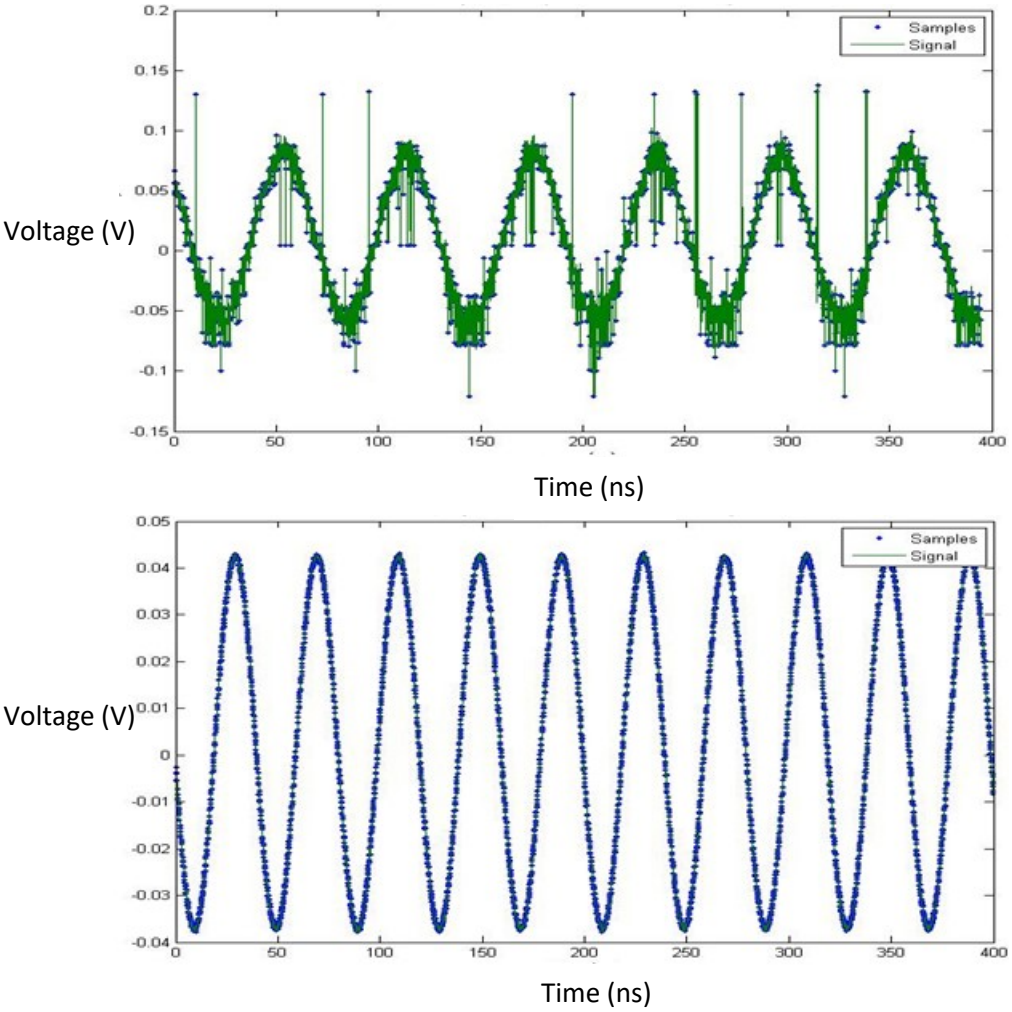

Figure 5.27. A comparison of the ADC output when (Top) the delays are not accounted for, and (Bottom) when it is properly timed with an 8.5° phase offset between the T/H and ADC clock inputs. The recorded samples are shown as the blue dots, the interpolated signal (linear) is shown in green.

The equivalent-time sampling circuit was integrated into the system prototype, replacing the Picoscope, and was tested with the narrow pulses used during the system operation. In order to resolve the fine details of these narrow pulses the sampling rate was now set to 24.984 MHz, resulting in an equivalent-time sampling rate of 40 GSa/s. In Fig. 5.28, the equivalent-time sampling circuit is used to record the pulse from the output of the Furaxa pulse generator. The pulse has been inverted by the T/H amplifier. Additionally, to compensate for the losses incurred from the T/H, a Low-Noise Amplifier

(LNA) was used prior to the T/H input. The FWHM of the recorded signal is measured to be 150 ps, compared to the 120 ps recorded with the Picoscope. In Fig. 5.28, the insertion loss of the equivalent-time sampling circuit, from the T/H, cables, and the ADC, has not been accounted for, and the output voltage is not normalized, thus, there is a discrepancy between the voltage of the recorded pulse in Fig. 5.28 and Fig. 5.21. A proper set of experiments remains to be carried out to normalize the values reconstructed from the output of the ADC and how they relate to the measured voltage. Additionally, it remains to be confirmed if the widening of the pulse with the equivalent-time sampling circuit is due to the BW limitations of the LNA or of some limitations of the equivalent-time sampling circuit. Nevertheless, these tests demonstrate that an equivalent-time sampling circuit can be used to record the high bandwidth signals used in a microwave system for breast health monitoring. Further testing is required to integrate the circuit into the finalized system, and to develop the necessary software to operate both the new switching matrix and the equivalent-time sampling circuit.

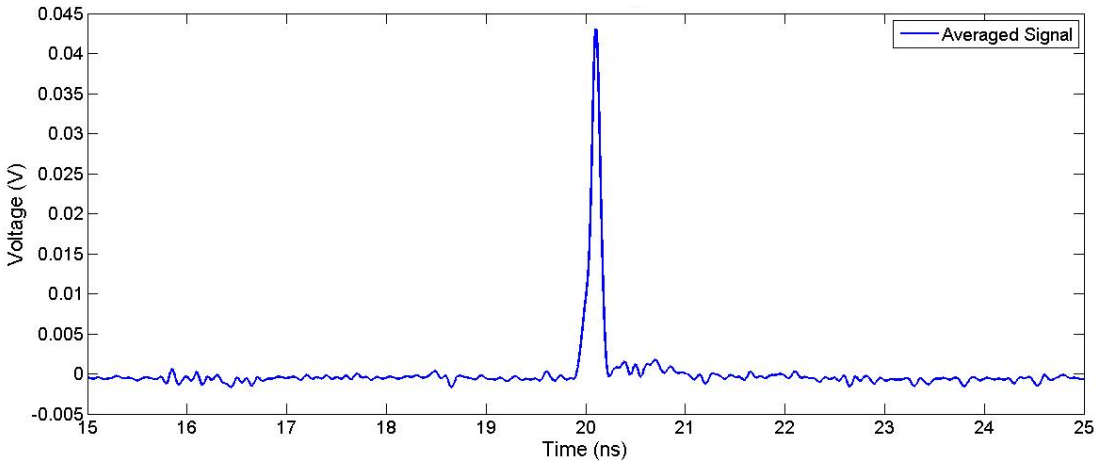

Figure 5.28. Reconstructed signal when using the equivalent-time sampling circuit to record the pulse generated from the Furaxa pulse generator. The signal is recorded with 16 averages and at an equivalent-time sampling rate of 40 GSa/s.

5.3.4 Summary and Future Hardware Considerations

This section presents a summary of the hardware changes made from the initial system prototype presented in Chapter 3 to the compact, low-cost system prototype developed in this thesis. A flexible multi-layer PCB was designed, tested, and integrated into the system to replace the switching matrix, antenna array, and the antenna radome. The design of a second generation of this flexible circuit, which further reduces the overall size of the circuit, the number of control lines, and addresses issues in regards to flexibility of the first-generation PCB was also presented. This flexible PCB significantly reduces the overall size and cost of the system. Additionally, as the switching matrix and antenna array are all now embedded in a singular PCB, mass production of the prototype would greatly reduce the per unit cost. The use of two development boards, the Adafruit Si5351 and the Furaxa Sampulse, were tested and integrated into the system as viable low-cost alternatives to the bulky components used for pulse generation and timing in the original system. An equivalent-time sampling circuit to replace the Picoscope, based on the design

from [52], was tested and integrated into the low-cost system prototype, and was shown to accurately reconstruct the high bandwidth signals used in the operation of the system.

A cost analysis of the proposed system is presented in Table 5.8. The final estimated cost for the new system is just under $13 000 CAD, in comparison to the initial experimental system that had an estimated cost of over $85 000 CAD. This price point can be further reduced as the different development boards are replaced for a singular board that can integrate each component. A photograph comparing the proposed low-cost system (with the Picoscope as the equivalent-time sampling circuit has not been fully integrated and tested with the system to date) and the original experimental system prototype is shown in Fig. 5.29. This photograph highlights the changes to the overall size of the electronics between the two prototypes. The largest components that remain in the newly proposed system are the power supplies, which can be easily replaced with on-board voltage regulators in a finalized design.

TABLE 5.8. COMPARSION OF FINAL SYSTEM COSTS

Equipment	Estimate Cost ($ CAD)
Furaxa Development Board	5 000
Adafruit Development Board	10
Flexible PCB	2 500
SMA cables (10)	1 000
Power Supplies	750
Equivalent-Time Sampling Circuit	3 000
Total System Cost	12 260

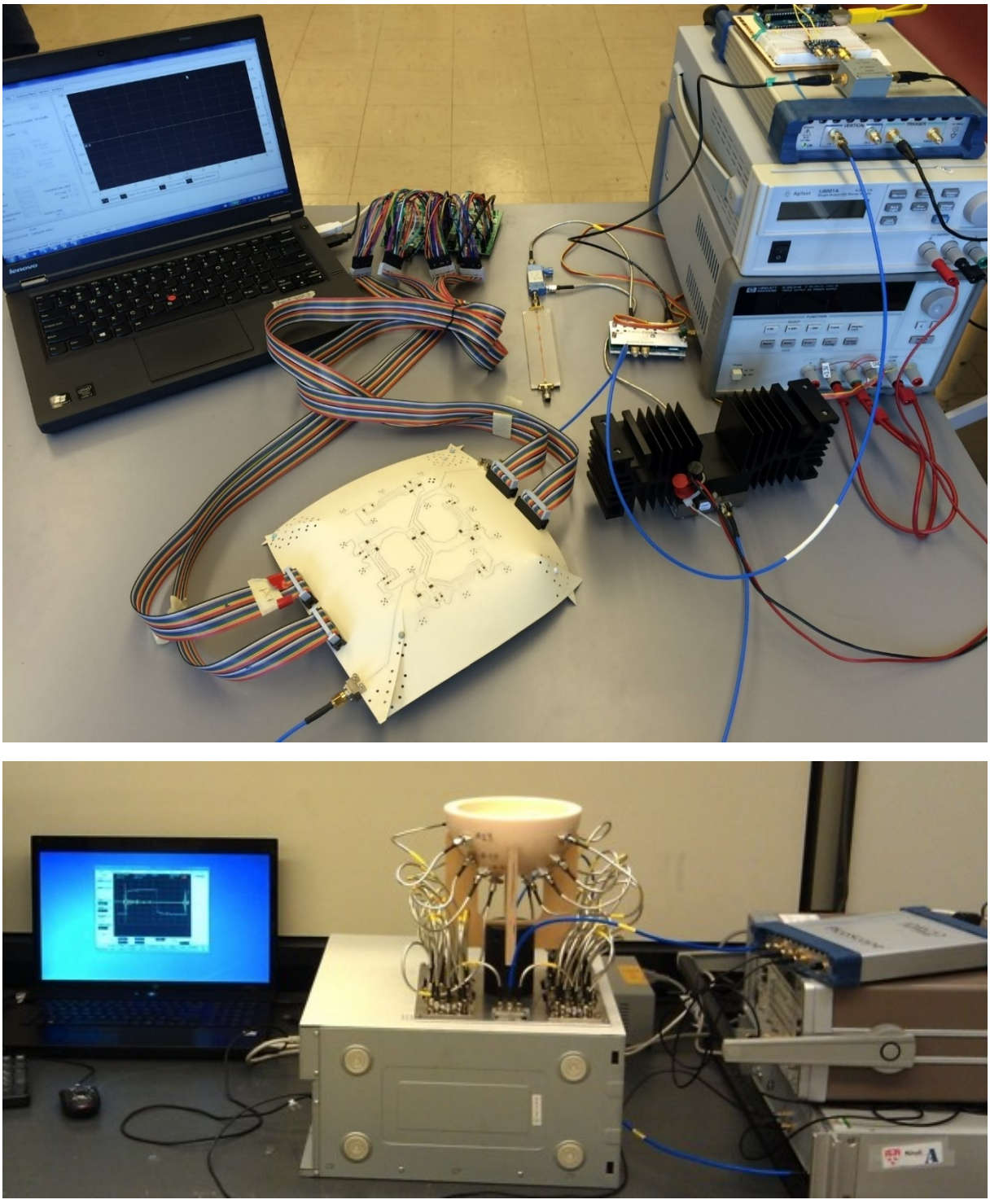

Figure 5.29. A comparison of the (Top) low-cost, and compact system developed and tested within this thesis (here the Picoscope is still in use) with the (Bottom) original experimental system (with the DC source hidden behind the switching matrix).

Future work on the hardware aspects of this prototype will be focused on successfully integrating and testing the proposed equivalent-time sampling circuit, and developing the necessary software to enable easy data collection, with the new system. Once the recording aspects of the new system have been addressed, the focus of the system design will shift towards integrating the various components at the heart of each development board (clock generator, pulse generator, T/H, ADC, DDS) onto a single PCB. The design and implementation of this PCB will further reduce the size and cost of the system, and remove the need for all but two SMA cables for the entire system, which will make it substantially more feasible to develop a commercially available, compact, and low-cost system for breast health monitoring. Notably, such a compact and cost-effective microwave time-domain system could also be applied to a wide range of other medical imaging or monitoring applications, such as brain or bladder imaging.

Chapter 6: Clinical Trials

This chapter discusses the motivation, planning steps, and potential challenges associated with undertaking clinical trials as a development stage of novel medical devices. Clinical trials represent a vital step in the development process of novel technologies. Trials are the link in taking a technology from the experimental bench to the bed side. This process is not without significant hurdles; the implementation of a successful clinical trial places high demand on recruitment efforts, time, and resources. A successful clinical trial is necessary to demonstrate the efficacy of a device and the overall reception of such a technology by both the patients and clinicians. If both of these needs are not met by the medical device, it will never see widespread implementation, voiding all possible benefits.

The experimental systems presented in this thesis were thoroughly tested with a wide variety of breast phantoms, followed by an acceptability study with patient volunteers. The next step was to conduct a clinical trial with a patient population of high risk patients, some of which may have already developed breast cancer. Working with an oncologist specializing in breast cancer detection and treatment, the aim of this clinical trial was to collect data in order to enable a comparison between images from a standard modality (mammography) and the reconstructed microwave images. Such a comparison would allow quantification of the ability of the microwave system to detect and localize tumours, as well as to confirm the breast density estimated using the system.

The clinical trial was a planned collaboration between McGill University and the Breast Clinic of the Cedar Institute at the McGill University Health Centre (MUHC). The MUHC is a research hospital whose researchers were keen to be involved with the development and testing of novel technologies that could improve patient outcomes. The study was to be carried out with the head oncologist of the department, who has access

to a large patient population. This location was chosen to conduct the clinical trial as it offered the best combination of providing high visibility of the research, working with leading experts in the field, and the opportunity to work directly with the key demographic.

Prior to commencing the clinical trial, proper ethical approval from the governing body had to be obtained. As this clinical trial was to be conducted at the MUHC, the governing body was the MUHC Research Ethics Board (REB). The structure of such approval was based on a comprehensive application and review process. All documentation, including the research protocol, recruitment leaflets, background research, and project proposal, must be completed in accordance to specific guidelines. Ultimately, a meeting was scheduled with the REB. This ethics board was comprised of nurses, clinicians, and laypersons from the community. It is essential that all documentation is carefully worded and phrased for this non-specialist target demographic. The review process was an iterative procedure, with feedback from the REB helping to tailor the documentation after each review. As the REB must review all applications for clinical trials which take place at the MUHC, the process of obtaining ethical approval is a significantly consuming procedure both in terms of time and resources, for both the applicants and the reviewers. In this case, the complete process took about 12 months. It is generally recommended to allot between 9 and 18 months for the ethical approval process.

After the REB approved the clinical trial, the next step in preparing the clinical study was a logistical question. The experimental system had to be moved from the laboratory to the Breast Clinic at the Cedar Institute. This meant that a space in the institute had to be agreed upon. Of course, as space in hospitals is always at a premium, it was necessary work with the hospital staff and compromise to ensure that all parties remained happy to participate. As the experimental system is a unique prototype, the

system had to be disassembled, packed, and moved to the MUHC. It was then necessary to set up the system at the new location in the Cedar Institute. A simple phantom experiment was carried out to verify that the system was operating as expected, and any potential outside interference, from other equipment in the hospital, would not impact the recorded data. The system used the bra-based interface as described in Section 3.4.

One of the primary obstacles of any clinical trial is that the research being carried out may represent additional work for individuals who are not a part of the research team. This can be the nurses, clinicians, or other staff at the location where the study is conducted. At the Breast Clinic at the Cedar Institute, there were various clinicians and nurses who were not directly involved with the clinical trial, and who were only learning about the research project upon their arrival at work on that specific day. The nursing staff represents an integral part of the research team, and it is vital to ensure that they understand the research goals of the clinical trial and to ensure that they are readily able to balance the demands of supporting the trial without impacting their regular duties. While the doctor is officially responsible for recruitment, in most cases it is the nursing staff that is the direct link between the researchers and the patients, and it will be them who will help with the recruitment process as they know the patient demographic the best. It is also very important to be mindful on the demands the clinical trial may have on the patient population. The patients will be naturally wary of any research tests that are novel or new. One must be prepared to discuss the research study at length, and in very simple and straightforward terms. Forming bonds with the patient population is a powerful tool in terms of recruitment.

The biggest hurdle the majority of clinical trials face is recruitment issues [116], [117]. In our clinical trial, carried out in December 2015, this was the biggest challenge. The Breast Institute is a secondary referral facility for the patients, who have already had suspicious breast exams on visits with their regular doctors. Thus, the patients who come

to the Breast Institute are subject to a comprehensive series of tests. On a given day, a patient may undergo an X-ray mammogram, meet with their clinician, then undergo an ultrasound or a biopsy. While these patients represent the ideal demographic, as a variety of case studies are possible and there is access to mammography data and radiology reports, it also means that the patients have a long and often arduous day in the clinic. They can be in the clinic for several hours, thus, the idea of doing another scan as part of a clinical trial is not always something that sounds appealing. The timing challenges lead to limited interest in participating in our study. Additionally, there were issues with the general perception of radio frequency/wireless transmission. To be clear, the term "microwave" was removed from patient materials prior to commencing the clinical study, as earlier meetings with relevant stakeholders suggested negative associations related with the word. However, in describing how the device works, comparison was made to common electromagnetic based wireless technologies. On several occasions, patient feedback was received stating concerns with regarding the use of wireless antennas in the microwave prototype, due to reports suggesting that WiFi and cell phones cause cancer. Clearly, further efforts must be made to familiarize patients with these types of technologies and to promote positive education related to the risks and benefits of participation.

In the end, this clinical trial concluded after successfully recruiting only three patients. While these three patients were eager to participate, and all three had a favourable experience with the clinical prototype (pain-free, quick scan time), data to compare the mammogram and the microwave scan images has not yet been analysed. With this data set, the opposite breast, that was proclaimed healthy by the investigating doctor, wsa used as the calibration data set. However, key lessons were learned in regards to the time and resources that must be dedicated to such a clinical trial. The study also highlighted the importance of the demographic choice and the trial location. While the Breast Clinic at the Cedar Institute offers vast potential for clinical studies, the patients were often

under a great deal of stress preparing for a diagnosis on the day, thus they did not represent the ideal patient population to try out a new medical device.

In summary, while clinical trials represent a significant challenge, they are necessary for the progress of a medical device from a laboratory prototype to a clinically used medical tool. This chapter highlighted the need to devote ample resources to forming strong bonds and working relationships with everyone involved in a clinical trial; be it industry partners, funding agencies, all hospital staff involved, and patient support groups. In order for the microwave breast screening system to progress to the next development stage, more clinical trials will be needed. Efforts to develop the next clinical study are currently underway, and will be a subject of future work.

Chapter 7: Conclusions and Future Work

7.1 Thesis Overview

This thesis has focused on the design, testing, and integration of a compact and low-cost microwave system prototype for breast health monitoring. Microwave systems for a breast cancer screening protocol offer several advantages over the current standard of X-ray mammography, including no breast compression, comfortable scans, and the capability to perform numerous and regular breast scans without ionizing radiation. A microwave system, as opposed to other complementary diagnostic tools (for example, magnetic resonance imaging) can be implemented in a cost-effective manner, thus enabling wider access and the potential to be used as part of a screening protocol implemented worldwide to help save lives from breast cancer.

In Chapter 1 of this thesis, the motivation for the use of a microwave system for breast health monitoring was presented. In Chapter 2, a thorough background on the topic, including breast anatomy, the development of breast cancer, a review of the primary breast screening technologies and an overview of microwave systems for medical diagnostics, was discussed. In Chapter 3, a time-domain microwave radar prototype for breast health monitoring was presented. An overview and discussion on the hardware components of the system was included and initial results were presented. Chapter 4 discussed the development of novel stable tissue mimicking materials, which were made of a mixture of polyurethane and carbon-based particles, to represent high water content materials. A wide range of materials were fabricated and dielectric measurements were performed to verify the stability and range in their complex permittivity. From these materials, accurate and modular breast phantoms, consisting of skin, fat, gland, and embedded tumours, were fabricated. These phantoms were then tested with the initial

system prototype. Finally, a specialized phantom with four embedded low-contrast tumours was fabricated and tested with various imaging modalities (MRI, CT).

In Chapter 5, the design of a novel multi-layer flexible circuit board was presented. This circuit board replaces several of the expensive and bulky components found in the initial experimental system, namely, the electromechanical switching matrix, the antenna array, and the antenna radome, with a smaller and more cost-effective solution. This circuit board was then integrated into the experimental system and its performance was compared to the initial system prototype using the rubber phantoms presented in Chapter 4. The design of a 2nd generation prototype that reduces the number of control lines, reduces the size of the PCB so it is more appropriately sized, and increases the flexibility of the PCB was then presented. A low-cost solution for the clock generator and pulse generator was then presented. These components were tested and integrated into the circuit, and demonstrated that they can successfully replace the large and bulky components used previously. An equivalent-time sampling circuit to replace the Picoscope was then demonstrated. Chapter 5 concluded with a comparison of the cost and size of the new system prototype with the initial system prototype tested in Chapter 3. In Chapter 6, some of the experiences, difficulties, and key observations from undertaking a Phase 0 clinical trial with an experimental medical device were presented.

7.2 Summary of thesis contributions

In this thesis, significant progress has been made in development of both the hardware and data analysis aspects of a microwave system for breast health monitoring. An initial system prototype was tested and modified for clinical use. A second generation low-cost and compact prototype was designed and tested. This newly proposed prototype reduced the overall cost of the system from approximately $87 000 to under $13 000 by designing novel hardware solutions to replace the large and bulky commercially available hardware

components used in the original prototype. These hardware advances highlight the potential for the development of a low-cost mass produced system that can be used for breast health monitoring in both developed and developing countries.

The novel contributions and key results of this thesis are as follows:

- The development and testing of the first clinically ready patient interface for a microwave time-domain experimental system;
- First demonstration of using machine learning classification techniques with experimental data obtained from breast phantoms;
- Application of hybrid artifact removal to a time-domain experimental system;
- Development, fabrication, and verification of stable tissue mimicking materials to represent high permittivity biological tissues;
- Development of heterogeneous modular realistic breast phantoms consisting of skin, fat, gland, and tumour regions;
- Development of a large scale phantom with four embedded tumours for verification with X-ray, ultrasound, and MRI;
- Design, testing, and integration of a multi-layer circuit board that has a solid-state switching network and embedded antenna array;
- Antenna array optimization for next generation iteration of flexible circuit board;
- Design of a second generation multilayer flexible circuit board with improved flexibility, fewer control lines, and optimized antenna array;
- Identification, testing, and integration of low-cost components for clock generation and pulse generation;
- Design and testing of a low-cost equivalent-time sampling circuit;
- Carried out a Phase 0 clinical trial with a system prototype in conjunction with a breast cancer specific clinic at the MUHC.

7.3 Future work

Immediate work will need to focus on integrating the equivalent-time sampling circuit into the prototype to replace the oscilloscope. This will also involve software development to ensure the proper operation of the switching network and the data collection, as both these processes require the use of MCUs to control their behaviour. Additionally, some software development will be required to ensure that the data collection process is automated and can be easily done by a nurse or technician for any future clinical work.

The next hardware improvements will need to focus on integrating the flexible PCB into a patient-ready interface. The idea of creating this flexible PCB is so that it can conform to the breast of the patient. Future research will need to determine how this PCB can be integrated into a bra-like structure, how the patient will use the device to ensure that the system use is repeatable, and how to improve the overall appearance of this prototype so it is not intimidating to future patients. Once the prototype is ready, future clinical trials will be necessary. These clinical trials will need to be carried out in several iterations; first, with healthy volunteers to confirm that the new prototype is easy to use and that the data recorded from the system is repeatable and accurate, and secondly, a more involved clinical trial with a large scale number of both healthy and unhealthy patients, who will undergo the standard screening protocol in order for comparison to determine the sensitivity and specificity of the microwave system.

Finally, recent advances in [118] and [119] have demonstrated the possibility of using low-cost frequency-domain based transceivers to replace a VNA. These low-cost components would replace the pulse generation and the equivalent-time sampling circuit aspects of the system prototype. Combining these components, with the advances from the flexible PCB for the antenna array and the switching network, will lead to the design

of a truly affordable system prototype that can be used to help screen for breast cancer in areas of the world where no screening protocol is currently in place, ultimately helping to save lives.

References

[1] World Health Organization. "Breast cancer: prevention and control," [Online]. Available: http://www.who.int/cancer/detection/breastcancer/en/ , last accessed: October 20, 2016.

[2] Canadian Cancer Society's Advisory Committee on Cancer Statistics, "Canadian Cancer Statistics 2016," Toronto, Ontario: Canadian Cancer Society, 2016.

[3] American Cancer Society, "Facts & Figures: 2014," Atlanta: 2014.

[4] B. O. Anderson and R. Jakesz, "Breast cancer issues in developing countries: an overview of the Breast Health Global Initiative," *World journal of surgery*, vol. 32, no. 12, pp. 2578 – 2585, 2008.

[5] J. B. Harford, "Breast-cancer early detection in low-income and middle-income countries: do what you can versus one size fits all," *The lancet oncology,* vol. 12, no. 3, pp. 306-312, 2011.

[6] E. Panieri, "Breast cancer screening in developing countries," *Best practice & research Clinical obstetrics & gynaecology,* vol. 26, no. 2, pp. 283-290, 2012.

[7] P. C. Gøtzsche, and K. J. Jørgensen, "Screening for breast cancer with mammography," *The Cochrane Database of Systematic Review,* vol. 6, 2013.

[8] N. K. Nikolova, "Microwave biomedical imaging," *Wiley Encyclopedia of Electrical and Electronics Engineering,* pp. 1 – 22, Apr. 2014.

[9] M. Lazebnik, et al., "A large-scale study of the ultrawideband microwave dielectric properties of normal, benign and malignant breast tissues obtained from cancer surgeries," *Physics in Medicine and Biology,* vol. 52, no. 20, pp. 6093-6115, 2007.

[10] Mayo Clinic Staff, Mayo Clinic. "Female Breast Anatomy," [Online]. Available: http://www.mayoclinic.com/health/breast-cancer-early-stage/BC00001 , last accessed October 20, 2016.

[11] S. M. Lewis, M. McLean Heitkemper, and S. R. Dirksen, "Medical-Surgical Nursing in Canada: Assessment and Management of Clinical Problems", 1st ed., S. Goldsworthy and Maureen Barry, Eds. Toronto, Canada: Elsevier Canada, 2006.

[12] V. Kumar, A. Abbas, N. Fausto and J. Aster, Robbins & Cotran, "Pathological Basis of Disease" (Chapter 7: Neoplasia), 8th ed., pp.259-330, United States: Elsevier, 2010.

[13] V. Y. Sohn, Z. M. Arthurs, J. A. Sebesta, T. A. Brown, "Primary tumor location impacts breast cancer survival", *American Journal of Surgery,* vol. 195, no. 5, pp. 641–644, 2008.

[14] E. I. Blumgart, R. F. Uren, P. M. F. Nielsen, M. P. Nash, H. M. Reynolds, "Predicting lymphatic drainage patterns and primary tumour location in patients with breast cancer", *Breast Cancer Research and Treatment*, vol. 130, no. 2, pp. 699–705, 2011.

[15] S. Rummel, M. T. Hueman, N. Costantino, C. D. Shriver, R. E. Ellsworth, "Tumour location within the breast: Does tumour site have prognostic ability?", *Ecancermedicalscience*, vol. 9, no. 552, 2015.

[16] J. E. Joy, E. E. Penhoet, and D. B. Petitti, editors, Saving women's lives: strategies for improving breast cancer detection and diagnosis (Chapter 2), National Academies Press, 2005.

[17] E. C. Fear, "Microwave Imaging of the Breast," *Techn. Cancer Res. Treat.*, vol. 4, no. 1, pp. 69-82, 2005.

[18] T. M. Kolb, J. Lichy, and Je. H. Newhouse, "Comparison of the performance of screening mammography, physical examination, and breast us and evaluation of factors that influence them: An analysis of 27,825 patient evaluations 1," *Radiology,* vol. 225, no. 1, pp. 165-175, 2002.

[19] M. Kriege, et al. "Efficacy of MRI and mammography for breast cancer screening in women with a familial or genetic predisposition", *N Engl J Med*, vol. 351, pp. 427-437, 2004

[20] S. G. Orel, "MR Imaging of the Breast," *Radiol. Clin. N. Am.*, vol. 38, no. 4, pp. 899-913, 2000.

[21] S. H. Heywang-Kobrunner, et al., "International Investigation of Breast MRI: Results of a Multicentre Study (11 Sites) Concerning Diagnostic Parameters for Contrast- Enhanced MRI Based on 519 Histopathologically Correlated Lesions," *Euro. Radiol.*, vol. 11, no. 4, pp. 531-546, 2001.

[22] C. Kuhl, et al. "Mammography, Breast Ultrasound and Magnetic Resonance Imaging for Surveillance of Women at High Risk of Familial Breast Cancer" *Journal of Clinical Oncology.* vol. 23, no.33, pp. 8469-8476, Nov. 2005.

[23] M. Lazebnik et al., "A large-scale study of the ultrawideband microwave dielectric properties of normal breast tissue obtained from reduction surgeries," *Phys. Med. Biol.*, vol. 52, pp. 2637-2656, 2007.

[24] T. Sugitani et al., "Complex permittivities of breast tumor tissues obtained from cancer surgeries", *Appl. Phys. Lett.*, vol. 104, 253702, pp. 1-5, 2014.

[25] P. M. Meaney, "Microwave open-ended coaxial dielectric probe: Interpretation of the sensing volume re-visited", BMC Med. Phys., vol. 14, no. 3, pp. 1-11, 2014.

[26] R. J. Halter et al., "The correlation of in vivo and ex vivo tissue dielectric properties to validate electromagnetic breast imaging: initial clinical experience," *Physiol. Meas.*, vol. 30, pp. 121-136, 2009.

[27] S. Gabriel, R.W. Lau, and C. Gabriel, "The dielectric properties of biological tissues: II. Measurements in the frequency range 10 Hz to 20 GHz," *Phys. Med. Biol.,* vol. 41, pp. 2251-2269, 1996.

[28] S. Gabriel, R.W. Lau, and C. Gabriel, "The dielectric properties of biological tissues: III. Parametric models for the dielectric spectrum of tissues," *Phys. Med. Biol.*, vol. 41, pp. 2271-2293, 1996.

[29] E. C. Fear, X. Li, S. C. Hagness, and M. A. Stuchly. "Confocal microwave imaging for breast cancer detection: Localization of tumors in three dimensions." *IEEE Transactions on Biomedical Engineering ,* vol. 49, no. 8, pp 812-822, 2002.

[30] M. Guardiola, S. Capdevila, J. Romeu, and L. Jofre, "3-D Microwave Magnitude Combined Tomography for Breast Cancer Detection Using Realistic Breast Models," *IEEE Antennas Wireless Propag. Lett.*, vol. 11, pp. 1622-1625, 2012.

[31] X. Zeng, A. Fhager, P. Linner, M. Persson, and H. Zirath, "Experimental Investigation of the Accuracy of an Ultrawideband Time-Domain Microwave-Tomographic System," *IEEE Trans. Instrum. Meas.*, vol. 60, no. 12, pp. 3939- 3949, 2011.

[32] R. C. Conceicao, H. Medeiros, M. O'Halloran, D. Rodriguez-Herrera, D. Flores-Tapia, and S. Pistorius, "SVM-based classification of breast tumour phantoms using a UWB radar prototype system," in Proc. *URSI General Assembly and Scientific Symposium (GASS)*, pp. 1–4, Beijing, China, Aug. 2014.

[33] D. Byrne, M. O'Halloran, M. Glavin, and E. Jones, "Breast cancer detection based on differential ultrawideband microwave radar," *Prog. Electromagn. Res.*, vol. 20, pp. 231–242, 2011.

[34] B. McGinley, M. O'Halloran, R. C. Conceicao, F. Morgan, M. Glavin, and E. Jones, "Spiking neural networks for breast cancer classification using radar target signatures," *Progress In Electromagnetics Research C*, vol. 17, pp. 79-94, 2010.

[35] P. M. Meaney, M. W. Fanning, D. Li, S. P. Poplack, and K. D. Paulsen, "A clinical prototype of active microwave imaging of the breast," *IEEE Trans. Microw. Theory Techn.*, vol. 48, pp. 1841–1853, 2000.

[36] T. Grzegorczyk, P. M. Meaney, P. A. Kaufman, R. M. diFlorio-Alexander, and K. D. Paulsen, "Fast 3-D Tomographic Microwave Imaging for Breast Cancer Detection," *IEEE Trans. Med. Imag.*, vol. 31, no. 8, pp. 1584-1592, 2012.

[37] P. M. Meaney, et al., "Microwave imaging for neoadjuvant chemotherapy monitoring: initial clinical experience." *Breast Cancer Research,* vol. 15, no. 2, 2013.

[38] N. R. Epstein, P. M. Meaney, and K. D. Paulsen, "3D parallel-detection microwave tomography for clinical breast imaging," *Rev. Sci. Instrum.*, vol. 85, pp. 124704-1 - 124704-12, 2014.

[39] J. Bourqui, J. Garrett, and E. Fear, "Measurement and Analysis of Microwave Frequency Signals Transmitted through the Breast," *Int. J. Biomed. Imag.*, vol. 2012, Article ID 562563, pp. 1-11, 2012.

[40] E. C. Fear, J. Bourqui, C. Curtis, D. Mew, B. Docktor, and C. Romano, "Microwave Breast Imaging With a Monostatic Radar-Based System: A Study of Application to Patients," *IEEE Trans. Microw. Theory Techn.*, vol. 61, no. 5, pp. 2119 – 2128, 2013.

[41] Kurrant, Douglas, Jeremie Bourqui, Charlotte Curtis, and Elise Fear. "Evaluation of 3-D Acquisition Surfaces for Radar-Based Microwave Breast Imaging." *IEEE Transactions on Antennas and Propagation* 63, no. 11 (2015): 4910-4920.

[42] Bourqui, Jeremie, and Elise C. Fear. "System for Bulk Dielectric Permittivity Estimation of Breast Tissues at Microwave Frequencies." *IEEE Transactions on Microwave Theory and Techniques* 64, no. 9 (2016): 3001-3009.

[43] M. Klemm, I. J. Craddock, J. A. Leendertz, A. Preece, and R. Benjamin, "Radar-Based Breast Cancer Detection Using a Hemispherical Antenna Array—Experimental Results*," IEEE Trans. Antennas Propag.,* vol. 57, no. 6, pp. 1692-1704, 2009.

[44] M. Klemm, J. A. Leendertz, D. Gibbins, I. J. Craddock, A. Preece, and R. Benjamin, "Microwave Radar-Based Differential Breast Cancer Imaging: Imaging in Homogeneous Breast Phantoms and Low Contrast Scenarios," *IEEE Trans. Antennas Propag.*, vol. 58, no. 7, pp. 2337-2344, 2010.

[45] M. Klemm, I. J. Craddock, J. A. Leendertz, A. Preece D. R. Gibbins, M. Shere and R. Benjamin, "Clinical Trials of a UWB Imaging Radar for Breast Cancer," in *Proc. Antennas and Propagation (EUCAP), 4th European Conference on*, pp. 1-4, Barcelona, Spain, Apr. 12-16, 2010.

[46] M. Klemm, D. Gibbins, J. Leendertz, T. Horseman, A. W. Preece, R. Benjamin and I. J. Craddock, "Development and Testing of a 60-Element UWB Conformal Array for Breast Cancer Imaging," in *Proc. Antennas and Propagation (EUCAP), 5th European Conference on,* pp. 3232-3234, Rome, Italy, Apr. 11-15, 2011.

[47] A. W. Preece, I. Craddock, M. Shere, L. Jones, and H. L. Winton, "MARIA M4: clinical evaluation of a prototype ultrawideband radar scanner for breast cancer detection," *Journal of Medical Imaging,* vol. 3, no. 3, 2016.

[48] C. Gilmore, et al., "A wideband microwave tomography system with a novel frequency selection procedure," *IEEE Transactions on Biomedical Engineering,* vol. 57, no. 4, pp. 894-904, 2010.

[49] D. Flores-Tapia and S. Pistorius, "Real Time Breast Microwave Radar Image Reconstruction Using Circular Holography: A Study of Experimental Feasibility," *Med. Phys.,* vol. 38, pp. 5420-5431, 2011.

[50] D. Flores-Tapia, O. Maizlish, C. Alabaster, and S. Pistorius, "Microwave Radar Imaging of Inhomogeneous Breast Phantoms using Circular Holography," *in Proc. Biomedical Imaging (ISBI), 9th IEEE International Symposium on*, pp. 86-89, Barcelona, Spain, April 30 – May 5, 2012.

[51] R. C. Conceição, H. Medeiro, M. O'Halloran, D. Rodriguez-Herrera, D. Flores- Tapia, S. Pistorius, "Initial Classification of Breast Tumour Phantoms Using a UWB Radar Prototype," *Electromagnetics in Advanced Applications (ICEAA), 2013 International Conference on,* pp. 720-723, Torino, Italy, Sept. 9-13, 2013.

[52] X. Zeng, A. Fhager, Z. He, M. Persson, P. Linner, and H. Zirath, "Development of a Time Domain Microwave System for Medical Diagnostics," *IEEE Trans. Instrum. Meas.*, vol. 63, no. 12, pp. 2931-2939, Dec. 2014.

[53] X. Zeng, A. Monteith, A. Fhager, M. Persson, and H. Zirath, "Noise performance comparison between two different types of time-domain systems for microwave detection," *International Journal of Microwave and Wireless Technologies*, 2016.

[54] H. Song, et al., "A Radar-Based Breast Cancer Detection System Using CMOS Integrated Circuits," *IEEE Access,* vol. 3, pp. 2111-2121, 2015.

[55] M. Persson, et al., "Microwave-based stroke diagnosis making global prehospital thrombolytic treatment possible" *IEEE Transactions on Biomedical Engineering*, vol. 61, no. 11, pp.2806-2817, 2014.

[56] A. T. Mobashsher, A. Mahmoud, and A. M. Abbosh, "Portable wideband microwave imaging system for intracranial hemorrhage detection using improved back-projection algorithm with model of effective head permittivity," *Scientific reports,* vol. 6, 2016.

[57] A. T. Mobashsher, K. S. Bialkowski, A. M. Abbosh, and S. Crozier, "Design and experimental evaluation of a non-invasive microwave head imaging system for intracranial haemorrhage detection," *PloS one,* vol. 11, no. 4, 2016.

[58] M. O'Halloran, Martin, F. Morgan, D. Flores-Tapia, D. Byrne, M. Glavin, and E. Jones, "Prototype Ultra Wideband Radar System for Bladder Monitoring Applications, "*Progress in Electromagnetics Research C*, vol. 33, pp. 17-28, 2012.

[59] M. O'Halloran, F. Morgan, M. Glavin, E. Jones, R. C. Conceio, and D. Byrne. "Bladder-state monitoring using ultra wideband radar," *in Proc. Antennas and Propagation (EUCAP), 7th European Conference on,* pp. 624-627, 2013.

[60] P. M. Meaney, et al., "Clinical microwave tomographic imaging of the calcaneus: a first-in-human case study of two subjects." *IEEE Transactions on Biomedical Engineering*, vol. 59, no. 12, pp. 3304-3313, 2012.

[61] N. R. Datta, et al., "Local hyperthermia combined with radiotherapy and-/or chemotherapy: Recent advances and promises for the future," *Cancer treatment reviews*, vol. 41, no. 9 pp. 742-753, 2015.

[62] H. D. Trefná, J. Vrba, and M. Persson. "Evaluation of a patch antenna applicator for time reversal hyperthermia," *International Journal of Hyperthermia*, vol. 26, no. 2, pp. 185-197, 2010.

[63] E. Porter, E. Kirshin, A. Santorelli, M. Coates, and M. Popović, "Time-domain multistatic radar system for microwave breast screening," *IEEE Antennas Wireless Propag. Lett.,* vol. 12, pp. 229-232, 2013.

[64] A. Santorelli, et al., "Experimental Demonstration of Pulse Shaping for Time-Domain Microwave Breast Imaging", *Prog. Electromagn. Res.*, vol. 133, pp. 309-329, 2013.

[65] E. Porter, E. Kirshin, A. Santorelli, and M. Popović, "Microwave Breast Screening in the Time-Domain: Identification and Compensation of Measurement-Induced Uncertainties," *Prog. Electromagn. Res. B*, vol. 55., pp. 115–130, 2013.

[66] E. Porter, A. Santorelli, and M. Popović, "Measurement Uncertainties in Differential Radar Applied to Breast Imaging," in *Proc. 2014 IEEE Sensors Applications Symposium (SAS)*, Queenstown, New Zealand, Feb. 18-20, 2014.

[67] E. Porter, J. Fakhoury, R. Oprisor, M. Coates and M. Popović, "Improved tissue phantoms for experimental validation of microwave breast cancer detection," in *Proc. 4th European Conference on Antennas and Propagation (EUCAP)*, Barcelona, Spain, April 12-16, 2010.

[68] E. Porter, A. Santorelli, A. Bourdon, D. Coulibaly, M. Coates and M. Popović, "Time-domain microwave breast cancer detection: experiments with comprehensive glandular phantoms," in *Proc. 2011 Asia-Pacific Microwave Conference (APMC)*, Melbourne, Australia, Dec. 5-8, 2011.

[69] E. Porter, A. Santorelli, D. Coulibaly, M. Coates and M. Popović, "Time-Domain Microwave Breast Screening System: Testing with Advanced Realistic Breast Phantoms," in *Proc. 6th European Conference on Antennas and Propagation (EUCAP)*, Prague, Czech Republic, March 26-30, 2012.

[70] E. Porter, A. Santorelli, and M. Popovic, "Time-Domain Microwave Radar Applied to Breast Imaging: Measurement Reliability in a Clinical Setting," Prog. Electromagn. Res., vol. 149, pp. 119-132, 2014.

[71] E. Porter, A. Santorelli, and M. Popović, "Time-Domain Microwave Radar for Breast Screening: Initial Testing with Volunteers," in *Proc. 8th European Conference on Antennas and Propagation (EUCAP)*, The Hague, The Netherlands, Apr. 6–11, 2014.

[72] E. Porter, A. Santorelli, and M. Popović "Breast Monitoring via Time-Domain Microwave Radar: Early Clinical Trial Study," in *Proc. 36th Ann. Int. Conf. IEEE Engineering in Medicine and Biology Society* (EMBC), Chicago, U.S.A., Aug. 26-30, 2014.

[73] E. Porter, A. Santorelli, M. Coates, and M. Popović, "Breast Tissue Screening with Microwave Time-Domain Radar: Initial Clinical Trials" in *Proc. IEEE Conf. Antenna Measurements & Applications (CAMA)*, Antibes Juan-les-Pins, France, Nov. 16-19, 2014.

[74] E. Porter, R. Kazemi, A. Santorelli, M. Popović, "Study of Daily Tissue Changes through Breast Monitoring with Time-Domain Microwave Radar," in *Proc. 9th European Conference on Antennas and Propagation (EUCAP)*, Lisbon, Portugal, Apr. 12–17, 2015.

[75] E. Porter, A. Santorelli, R. Kazemi, and M. Popović, "Daily Breast Monitoring with Time-Domain Microwave Radar," *IEEE Antennas Wireless Propag. Lett.*, vol. PP, no. 99, pp. 1-4, 2015.

[76] E. Porter, H. Bahrami, A. Santorelli, B. Gosselin, L. A. Rusch and M. Popović, "A Wearable Microwave Antenna Array for Time-Domain Breast Tumor Screening," *IEEE Transactions on Medical Imaging*, vol. 35, no. 6, pp. 1501-1509, June 2016.

[77] A. Santorelli, E. Kirshin, E. Porter, M. Popović, and J. Schwartz, "Improved Calibration for an Experimental Time-Domain Microwave Imaging System" in *Proc. 7th European Conference on Antennas and Propagation (EUCAP)*, Gothenburg, Sweden, Apr. 8–12, 2013.

[78] A. Santorelli, E. Porter, E. Kirshin, Y. J. Liu, and M. Popović, "Investigation of Classifiers for Tumor Detection with an Experimental Time-Domain Breast Screening System," *Prog. Electromagn. Res.*, vol. 144, pp. 45–57, 2014.

[79] A. Santorelli, Y. Li, E. Porter, M. Popović, and M. Coates, "Investigation of Classification Algorithms for a Prototype Microwave Breast Cancer Monitor," in *Proc. 8th European Conference on Antennas and Propagation (EUCAP)*, The Hague, The Netherlands, Apr. 6–11, 2014.

[80] G. Ursin, et al., "Mammographic Density Changes During the Menstrual Cycle," *Cancer Epidemiol. Biomarkers Prev.*, vol. 10, pp. 141–142, 2001.

[81] E. White, et al, "Variation in mammographic breast density by time in menstrual cycle among women aged 40-49 years," *J. Natl. Cancer Inst.*, vol. 90, no. 12, pp. 906–910, 1998.

[82] H. Kanj, and M. Popović, "A novel ultra-compact broadband antenna for microwave breast tumor detection," *Prog. Electromagn. Res.*, vol. 86, pp. 169-198, 2008.

[83] A. Santorelli, E. Porter, E. Kang, T. Piske, M. Popović, M.; Schwartz, J.D., "A Time-Domain Microwave System for Breast Cancer Detection Using a Flexible Circuit Board," *IEEE Trans. Instrum. Meas.*, vol. 64, no. 11, pp. 2986-2994, Nov. 2015.

[84] E. Kirshin, "Microwave breast cancer detection: Signal processing and device prototype", Ph.D. Thesis, Dept. Elec. and Comp. Eng., McGill Univ., Montréal, Canada, 2015.

[85] E. J. Bond, Xu Li, S. C. Hagness and B. D. Van Veen, "Microwave imaging via space-time beamforming for early detection of breast cancer," *IEEE Transactions on Antennas and Propagation*, vol. 51, no. 8, pp. 1690-1705, Aug. 2003.

[86] H. Been Lim, N. Thi Tuyet Nhung, E.P. Li, and N. Duc Thang, "Confocal Microwave Imaging for Breast Cancer Detection: Delay-Multiply-and-Sum Image Reconstruction Algorithm," *IEEE Transactions on Biomedical Engineering*, vol.55, no.6, pp.1697-1704, June 2008.

[87] E. Porter, "Microwave time-domain radar for monitoring breast health: development and testing of an early prototype", Ph.D. Thesis, Dept. Elec. and Comp. Eng., McGill Univ., Montréal, Canada, 2015.

[88] H. Bahrami, E. Porter, A. Santorelli, B. Gosselin, M. Popović, and L. A. Rusch, "Flexible Sixteen Antenna Array for Microwave Breast Cancer Detection," *IEEE Transactions on Biomedical Engineering*, vol. 62, no. 10, pp. 2516 - 2525, 2015.

[89] Z. Wang, A. C. Bovik, H. R. Sheikhm and E. P. Simoncelli, "Image quality assessment: From error visibility to structural similarity," *IEEE Trans. Image Process.*, vol. 13, no. 4, pp. 600–612, Apr. 2004.

[90] M. A. Elahi, A. Shahzad, M. Glavin, E. Jones and M. O'Halloran, "Hybrid Artifact Removal for Confocal Microwave Breast Imaging," *IEEE Antennas and Wireless Propagation Letters*, vol. 13, pp. 149-152, 2014.

[91] A. Santorelli, P. Hazarika, M. Popović, A. Elahi and M. O'Halloran, "Hybrid artifact removal for breast imaging applied to a time-domain microwave system," *2016 17th International Symposium on Antenna Technology and Applied Electromagnetics (ANTEM)*, Montreal, QC, pp. 1-2, 2016.

[92] Arnau, O., J. Freixenet, R. Martí, and R. Zwiggelaar, "A comparison of breast tissue classification techniques," *Medical Image Computing and Computer-Assisted Intervention*–MICCAI 2006, pp. 872-879. Springer Berlin Heidelberg, 2006.

[93] Prasad, D.P., C. Quek, and M. K.H. Leung. "A hybrid approach for breast tissue data classification." in *TENCON 2009-2009 IEEE Region 10 Conference*, pp. 1-4, 2009.

[94] Davis, Shakti K., et al., "Breast tumor characterization based on ultrawideband microwave backscatter," *IEEE Transactions on Biomedical Engineering,* vol. 55, no. 1, pp. 237-246, 2008.

[95] Kerhet, A., M. Raffetto, A. Boni, and A. Massa "A SVM-based approach to microwave breast cancer detection," Engineering Applications of Artificial Intelligence, vol. 19, pp. 807-818, 2006.

[96] Conceição, R. C., M. O'Halloran, M. Glavin, and E. Jones, "Support Vector Machines for the Classification of Early-stage Breast Cancer Based on Radar Target Signatures," *Prog. Electromagn. Res. B*, vol. 23, pp. 311–327, 2010.

[97] Byrne, D., M. O'Halloran, E. Jones, and M. Glavin, "Support Vector Machine-Based Ultrawide-band Breast Cancer Detection System," *J. of Electromagn. Waves and Appl.*, vol. 25, pp. 1807–1816, 2011.

[98] Conceicao, R. C., et al. "Evaluation of features and classifiers for classification of early-stage breast cancer." *Journal of Electromagnetic Waves and Applications,* vol. 25, no. 1, pp. 1-14, 2011.

[99] Hsu, C.-W., C.-C. Chang, and C.-J. Lin, "A practical guide to support vector classification," Department of Computer Science, National Taiwan University, Tech. Rep., 2003. [Online]. Available: http://www.csie.ntu.edu.tw/ cjlin/papers.html.

[100] M. Lazebnik, E. L. Madsen, G. R. Frank, and S. C. Hagness, "Tissue- mimicking phantom materials for narrowband and ultrawideband microwave applications," *Phys. Med. Biol.*, vol. 50, no. 18, pp. 4245–58, Sep. 2005.

[101] A.Mashal, F. Gao, and S. C. Hagness, "Heterogeneous anthropomorphic phantoms with realistic dielectric properties for microwave breast imaging experiments," *Microw. Opt. Technol. Lett.*, vol. 53, no. 8, pp. 1896–1902, Aug. 2011.

[102] J. Garrett and E. Fear, "Stable and Flexible Materials to Mimic the Di- electric Properties of Human Soft Tissues", *Antennas Wireless Propag. Lett.*, vol. 13, pp. 599-602, 2014.

[103] J. Garrett and E. Fear, "A New Breast Phantom With a Durable Skin Layer for Microwave Breast Imaging," *IEEE Transactions on Antennas and Propagation*, vol. 63, no. 4, pp. 1693-1700, April 2015.

[104] A. Santorelli, O. Laforest, E. Porter and M. Popović, "Image classification for a time-domain microwave radar system: Experiments with stable modular breast phantoms," in Proc. *9th European Conference on Antennas and Propagation (EUCAP)*, Lisbon, 2015, pp. 1-5.

[105] Y. Li, A. Santorelli, O. Laforest, and M. J. Coates, "Cost-sensitive ensemble classifiers for microwave breast cancer detection", *IEEE Int. Conf. Acoustics Speech and Sig. Proc. (ICASSP)*, Brisbane, Australia, 04/2015.

[106] B.J. Mohammed, A.M. Abbosh, S. Mustafa, and D. Ireland, "Microwave System for Head Imaging," *IEEE Trans. Instrum. Meas.,* vol.63, no.1, pp.117-123, Jan. 2014.

[107] A. Azhari, S. Takumi, S. Kenta, T. Kikkawa X. Xiao, "A 17 GHz bandwidth 1.2 mW CMOS switching matrix for UWB breast cancer imaging," in *Proc. Biomed. Circuits and Systems, IEEE Conf.*, pp.109-112, Oct. 22-24, 2014.

[108] M. Haynes, J. Stang, and M. Moghaddam. "Microwave breast imaging system prototype with integrated numerical characterization." *J. Biomed. Imag.*, pp. 1- 18, 2012.

[109] J. Bourqui, J. M. Sill, and E. C. Fear, "A prototype system for measuring microwave frequency reflections from the breast," *Int. J. Biomed. Imag.*, vol. 2012, Article ID 851234, pp. 1–12, 2012.

[110] E. Porter, G. Walls, Y. Zhou, M. Popović, and J. D. Schwartz, "A Flexible Broadband Antenna and Transmission Line Network for a Wearable Microwave Breast Cancer Detection System," *Prog. Electromagn. Res. Lett.*, vol. 49, pp. 111-118, 2014.

[111] A. Santorelli, E. Porter, S. Dantas, M. Popović and J. Schwartz, "Low-cost hardware for a time-domain microwave system for breast health monitoring," in Proc. *10th European Conference on Antennas and Propagation (EUCAP),* Davos, 2016, pp. 1-4.

[112] L. Wang, A. M. Al-Jumaily, and R. Simpkin, "Investigation of antenna array configurations using far-field holographic microwave imaging technique," *Progress In Electromagnetics Research M*, vol. 42, pp. 1–11, 2015.

[113] Adafruit, "Adafruit Si5351 clock generator breakout," Aug. 2014. [Online]. Available: https://learn.adafruit.com/downloads/pdf/adafruitsi5351-clock-generator-breakout.pdf

[114] Furaxa, "Sampulse20x2 dual pulser/sampler demo board," Dec. 2015. [Online]. Available: http://www.furaxa.com/Documents/SamPulse20x2 122715.pdf

[115] K. El-Hallaoui, A. Santorelli, M. Popović, and M. Coates, "Signal Analysis and Phantom Experiments for a Miniaturized Time-Domain Microwave Breast Health Monitoring Device," in Proc. *11th European Conference on Antennas and Propagation (EUCAP)*, 2017 [accepted].

[116] E. Mahon, J. Roberts, P. Furlong, G. Uhlenbrauck, and J. Bull, "Barriers to Clinical Trial Recruitment and Possible Solutions: A Stakeholder Survey", *Applied Clinical Trials*, 2015.

[117] S. Ross, A. Grant, C. Counsell, W. Gillespie, I. Russell, and R. Prescott, "Barriers to participation in randomised controlled trials: a systematic review," *Journal of clinical epidemiology*, vol. 52, no. 12 pp. 1143-1156, 1999.

[118] J. Marimuthu, K. S. Bialkowski and A. M. Abbosh, "Software-Defined Radar for Medical Imaging," *IEEE Transactions on Microwave Theory and Techniques,* vol. 64, no. 2, pp. 643-652, Feb. 2016.

[119] J. A. T. Vasquez, F. Vipiana, M. R. Casu, M. Vacca and A. Pulimeno, "Experimental testing of a low-cost microwave imaging system for early breast cancer detection," *10th European Conference on Antennas and Propagation (EUCAP)*, Davos, 2016, pp. 1-3.